Study on the Neuronal Activities Regulating a Caenorhabditis elegans Salt-chemotaxis Circuit

year	2017
	(University of Tsukuba)
	2016
	12102　　8149
URL	http://hdl.handle.net/2241/00148005

Study on the Neuronal Activities Regulating a *Caenorhabditis elegans* Salt-chemotaxis Circuit

January 2017

Masahiro KURAMOCHI

Study on the Neuronal Activities Regulating a *Caenorhabditis elegans* Salt-chemotaxis Circuit

A Dissertation Submitted to

the Graduate School of Life and Environmental Sciences,

the University of Tsukuba

in Partial Fulfillment of the Requirements

for the Degree of Doctor of Philosophy

(Doctoral Program in Life Sciences and Bioengineering)

Masahiro KURAMOCHI

Abstract

One of the ultimate challenges in neuroscience is to elucidate animal behaviors which is navigated by the end product of interaction between elementary processing in the nervous system. In the past decades, increasing amount of studies has characterized the mechanisms underlying neural encoding for behavioral outputs. However, it is yet difficult to clearly describe neural encoding for one behavior, because we have not entirely understood how the spatio-temporal activity in individual neurons contributes circuit dynamics for that behavior.

An integrated analysis which performs both the *in-vivo* measurement of neuronal activity and the computational modeling using observation data is useful for understanding the circuit dynamics of one behavior. This strategy could easily predict the patterns of each neuronal activity involved in the circuit and gives us important information to estimate the spatio-temporal dynamics of each single neuronal activity during behavior. Furthermore, by combining the strategy with synaptic information in the circuit, we can understand characteristics of a neural encoding for behavioral outputs. In this study, I focused on the salt-chemotaxis behavior in the nematode *Caenorhabditis elegans*.

The *C. elegans* has only 302 neurons and is a useful model organism both for neuronal and for behavioral study. In particular, the neural mechanism of the salt-chemotaxis behavior has been well analyzed for decades. *C. elegans* detects NaCl by a pair of salt-sensing neurons named ASEL/R and shows both attractive or repulsive behaviors dependent on former experience. For this chemotaxis behavior, the

salt-sensing neurons ASEL and ASER have an opposite sensory function: ASEL is activated by the upstep of NaCl concentration, whereas ASER is activated by the downstep of NaCl concentration. In addition, these neurons seem to have distinct roles for the behavior, such as a forward run probability by ASEL and a turn probability by ASER. To understand how these two sensory neurons navigate these opposite behaviors through synapses, a novel integrated analysis should be introduced for the detailed description of neural encoding. Thus, I developed the novel computational model based on multi-regional calcium imaging which precisely represents the spatio-temporal dynamics in the ASER neuron. In addition, I analyzed how ASEL/R neurons regulate the activity of postsynaptic neurons AIB through synaptic connections to expand the integrated analysis to a circuit level.

To generate a novel mathematical model which predicts *C. elegans* neuronal activity *in silico*, I observed the spatio-temporal calcium responses in the ASER neuron, in response to various patterns of NaCl stimulation. The ASER neuron showed simple temporal responses to the downstep of concentration, relatively fast activation and slow decay followed by peak response during the downstep of NaCl concentration. On the other hand, the upstep of NaCl concentration rapidly inactivated ASER. The responses in the dendrite, soma, and axon showed similar temporal dynamics to various types of NaCl stimuli. Based on collected ASER calcium responses, I constructed a novel mathematical model named the three-unit ODE model, which predicts neuronal activities in various parts of the cells. This model successfully reproduced the spatio-temporal activity of this neuron in response to not only a simple downstep-concentration change but also to the various types of stimuli such as ran-

4

domized concentration changes. Most surprisingly, this model can reliably reproduce the neuronal responses to several types of stimulation patterns, though the model was constructed based on the single calcium responses to one sensory stimulation. On the other hand, the model did not reproduce well quantitative neuronal activities to tiny changes of NaCl concentration. The actual imaging data showed that the response of ASER neuron was not linear to the step changes of NaCl concentration but seemed to be sigmoidal. I thus found that a sigmoidal transfer function to simulated responses was required to fit simulated peak responses with actual neuronal responses. This sigmoidal transfer allows to predict the response of ASER neuron when it received small input stimuli. Furthermore, it is also possible to estimate worm's NaCl-concentration environment by using the proposed neuronal model with sigmoidal transfer.

To expand this integrated analysis to the neuronal circuit for the salt-chemotaxis behavior, the synaptic information should be included to the three-unit ODE model. I thus examined activities of the first-layer interneurons AIB which are connected by the ASE presynaptic neurons, and tried to evaluate the role and meaning of each synaptic connection for their neuronal activities. To analyze the synaptic signaling between these two neurons, I monitored the calcium responses in postsynaptic AIB neurons of the wild-type or the sensory-input defective mutant animals. These analyses indicated that the ASE neurons really regulate AIB activity. Furthermore, by using synaptic transmission defective mutants and their cell-specific rescuing animals, I found that the glutaminergic signal from ASEL inhibits AIB through an unidentified receptor, whereas that from ASER stimulates AIB through an AMPA-type ionotropic glutamate receptor. The sites of each synapse between ASEL-to-AIB or

ASER-to-AIB were accurately coordinated on their neurites, according to the type of glutamate receptors. This finding provides a novel aspect of the synaptic regulation from a single type of sensory neuron to lead appropriate postsynaptic responses for the salt-chemotaxis behavior.

Calcium imaging methods are widely used to analyze whole-brain activities from worms to mammals. This novel computational model based on calcium response will greatly contribute to estimate neuronal circuit dynamics for several behaviors and complex brain functions.

Contents

List of Figures

13

List of Tables

Acknowledgement

I thank my co-adviser Motomichi Doi for countless hours and patience in mentoring me, teaching me both how to do science and how to perform cutting-edge molecular biology for *in vivo* observation of brain activity in the worm. I thank the other members of my thesis committee, Akiyoshi Fukamizu, Sosaku Ichikawa, and Nobutada Kimura for being so accommodating and for providing valuable research advice and critical thinking about this work. I thank Saya Tsukakoshi and Megumi Sato for technical assistance and Yoichi Shinkai and other members in AIST for critical discussion for this study. I also thank Miho Iijima at Fukamizu Lab for taking care of office work for me.

I thank Yuichi Iino, Hirofumi Kunitomo and Hirofumi Sato for providing calcium imaging techniques and for sharing a plasmid DNA, and Takeshi Ishihara and Takayuki Teramoto for sharing G-GECO plasmids. I thank Takaaki Hirotsu for sharing a *Pttx-3::glr-1::gfp* plasmid DNA, and also thank Sreekanth Chalasani for sharing a *Pttx-3::TeTx::mCherry* plasmid DNA. I thank Masahiro Tomioka for providing about information of plasmid DNA. I also thank Yuishi Iwasaki, Yu Toyoshima, and Mamoru Usuyama for critical discussion about a computational model.

I thank my old brother Takahiro for being a role model, and showing me many of the cool things in life. Finally, I thank my parents Kazuhiko and Mitsuko for generous support in all of my challenges, and showing me the pleasure and importance of looking at things critically and the satisfaction of completion.

Some strains were provided by the CGC which is funded by NIH Office of Research

Chapter 1

General Introduction

1.1 Role of information processing and its analytical difficulty in animal brain

How does animal's brain (neural circuit) produce the complex phenomena that are perception, memory formation, learning, and decision making? The brain can represent these interesting phenomena by the interaction between elementary processing in the nervous system. To understand the neural mechanisms for navigating these phenomena, the information flow at cellular-resolution level in the brain should be observed. In the each brain region, the enormous number of neurons interacts with each other spatially and temporally to generate these functions. So it is difficult to analyze the information processing of the brain network in cellular-resolution level. Moreover, the following neuronal features also cause analytical difficulties in the nervous system. (1) Neuronal state is switched stochastically by a feedforward- and a feedback-signal

through synapses [1, 2]. (2) The temporal features in neurons include a 'chaotic' behavior. In fact, a chaotic oscillation is experimentally observed in the squid giant axon when the axon was stimulated by an oscillated sinusoidal force [3]. These neuronal features generate the complex information processing in neural circuit which functions as a gigantic complex system, in which individual neurons interact with stochastically and chaotically through synapses. The mammalian brains consisted of multibillion neurons contain a difficulty for describing the relationship between neural circuit dynamics in cellular resolution and their roles in behavioral outputs. In contrast, lower organisms such as *Caenorhabditis elegans*, *Drosophila*, and zebrafish have a much compact nervous system which may be an advantage for the description of circuit dynamics in a cellular level.

1.2   *C. elegans* for neuroscience

The nematode *Caenorhabditis elegans* has only 302 neurons and is a useful model organism both for neuronal and for behavioral study. Synaptic connectivity in the *C. elegans* nervous system has been identified [4]. Varshney and his colleagues reported that a total of 7,283 synaptic connections are involved in 279 somatic neurons, in which 6,393 are chemical synapses, and 890 are gap junctions [5]. In spite of such a smaller nervous system compared to mammal brains, worms execute a broad spectrum of behaviors, ranging from simple motor and sensory behaviors to more complex mating, social, sleep, and drug-dependent behaviors, as well as associative learning and memory [6, 7, 8, 9, 10]. However, the knowledge on synaptic connectivity alone

is insufficient for understanding the patterns of neural activity and their regulations for behaviors.

The electrophysiological studies provide characteristics of individual neuronal activity [11, 12, 13, 14]. Goodman and her colleagues developed a whole-cell patch clumping technique for *C. elegans* neurons, and clarified that many *C. elegans* neurons exhibit a graded potential without classical Na^+-based action potential [11]. The voltage-sensitive sodium channels have not been identified in the *C. elegans* genome [11, 12]. Instead of the sodium-based classical action potential, *C. elegans* neurons are likely to use calcium-based signal amplification for generating intracellular currents. These electrophysiological studies have a restriction in which a simultaneous observation of the multiple neuronal activity is hard. So, such single-cell level analyses have not provided meaningful descriptions for animal behaviors which is navigated by the end product of interaction between elementary processing of neurons. To understand the relation between nervous system and behavioral output, temporal activity of multiple neurons should be observed simultaneously.

Real-time calcium imaging from single-cell level to whole-brain level can be applied in living worms to overcome above difficulty [15, 16, 17]. Calcium signals in *C. elegans* neurons are generally correlated with their depolarization and hyperpolarization, meaning that we can basically treat calcium response as a neuronal activity. The small and simple nervous system in *C. elegans* transparent body is suitable for real-time imaging, and this can illuminate not only dynamic responses of individual neurons but also temporal relationship among many cells. Interestingly, the preceding studies showed that calcium dynamics in *C. elegans* neurons can vary among cellu-

lar compartments [18, 19, 20]. Kato and his colleagues found out that locomotion behavior could be represented by cyclical trajectory of distributed neural activity using wide-brain-imaging at single-cell resolution in immobilized animals [21]. Real-time calcium imaging provides these insights for sensory- and circuit-driven behavior. Furthermore, recording systems for large-scale circuits with cellular resolution during free locomotion has been developed using a spinning disk confocal microscope [16, 17]. The pan-neuronal imaging in free moving animals will facilitate systematic analyses for circuit dynamics control behavioral output in systems neuroscience.

Here, using calcium imaging, I characterized a neuronal- and circuit-activity in the *C. elegans* salt-chemotaxis behavior to generate the computational model for understanding the relation between circuit dynamics and behavioral output. The neuronal and molecular mechanism regulating this behavior has been analyzed for decades [22, 23, 24, 25, 26]. *C. elegans* detects NaCl by a pair of salt-sensing ASEL/R neurons and basically shows attraction to NaCl. It has been shown that the attraction to NaCl is caused by several behavioral strategies to achieve a better living condition [23, 27]. These previous studies also provide valuable information to describe the relation between neuronal encoding and behavior. The salt-sensing neurons ASEL and ASER have an opposite sensory function: ASEL is activated by the increase of NaCl concentration, whereas ASER is activated by the decrease of NaCl concentration. ASEL promotes forward run probability, whereas ASER promotes turn probability [24]. Although the relation between sensory inputs and behavioral outputs has been described, the mechanism of the neuronal information processing as transfer function for salt-chemotaxis behavior is not well understood yet. How does

a sensory activity affect the postsynaptic neuronal responses? What kind of synaptic signal does regulate a fine behavior change to NaCl? Can I speculate a neuronal signaling pathway dependent on NaCl conditions by using simulation model? To answer these questions, I focused on this neuronal circuit and behavior.

1.3 Computational models for neural circuit analysis in *C. elegans*

To understand systematically the information flow in neural circuit, the computational modeling and simulation analysis are quite useful. Computational modeling has an essential integrative role to understand dynamic neural interaction. Simulation analysis provides a new perspective or hypothesis for biological experiments which we cannot perform easily in hand. Computational model or simulation often invites a new perspective which is not retrieved from usual experiments, but we should keep in mind that a model is not perfect. If model teaches us nothing new, it may be useless. To develop an useful model, model should be refined by experimental data. The theory/experiment integration analysis leads us a deeper understanding for neuroscience. I believe that computational models should have much benefits for neural circuit analysis in *C. elegans*. Here I introduce the current state of a useful computational models for the *C. elegans* nervous system.

A sensorimotor integration for *C. elegans* computational modeling is often divided into two phases; neuronal model and body-movement model. As an example of

neuronal model, the conductance-based model has been applied for the analysis of synaptic polarities (excitatory/inhibitory) [28, 29, 30, 31]. In addition, an integrated leaky-and-fire neuronal model is also applied for circuit-behavior analyses [32, 33]. On the other hand, the body-movement model in *C. elegans* can be divided into several segments. A muscle tension of individual segments is modeled as difference of motor neuronal activities in ventral- and dorsal-side. Boyle, Berri, and Cohen developed a neuro-mechanical model for locomotion by using realistic environmental forces [34]. As for other models, Kato and his colleagues characterized the dynamics of *C. elegans* sensory neurons by calcium imaging under the influence of various stimuli. Based on this *in vivo* imaging data, they modeled the phenomenological filters for sensory neurons as a three-first-order linear ordinary differential equations [35]. In these models, neurons are represented as a deterministic unit (compartment). On the other hand, Roberts and his colleagues modeled neuronal activity state as a stochastic switch model, and applied for analysis of locomotion state transition in random search [2].

C. elegans is one of the best animals for the whole-brain modeling (emulation) as a sensorimotor integration system. Recently, there are several projects for whole-brain emulation in which purpose is to reconstruct the whole-brain activity in a cellular-level. The OpenWorm project is an attempt to build a complete cellular-level simulation of *C. elegans* neurons [36]. The simulation analyses have been performed using the hodgkin-huxley model [37] which handles electrical activities in all the muscles and neurons. On the other hand, *Si elegans* project is an attempt to develop a whole-brain in *C. elegans* as a hardware which has 302 parallel interconnected pro-

24

cessing unit named advanced field-programmable gate array (FPGA) [38]. Although there are efforts toward whole-brain emulation, a computational model with cellular-resolution level for whole-brain activity has not been established yet. Can I build a computational model which has a biophysical justification for whole-brain with cellular resolution? I believe it is a possibility. In chapter II and III, I evaluated the feasibility for whole-brain modeling.

1.4 Goals

This thesis represents the beginning of an endeavor to generate a computational modeling of the whole-brain dynamics in *C. elegans* based on calcium imaging data. The goal of this work is to:

1. Characterize the spatio-temporal dynamics in a *C. elegans* salt-sensing neuron to the step-like NaCl stimuli by calcium imaging.

2. Develop a computational model for the spatio-temporal activity in a *C. elegans* salt-sensing neuron under the influence of various time-varying stimuli.

3. Characterize the synaptic transmission in a salt-chemotaxis circuit toward developing computational model for circuit analysis.

In chapter II, I attempted to develop the computational model for the spatio-temporal dynamics in a single-cell activity (above 1 and 2). In chapter III, I quested the mechanism of neural encoding through synapses in salt-chemotaxis circuit to develop the computational model of synaptic transmission for circuit modeling (above 3).

Bibliography

[1] Gordus, A., Pokala, N., Levy, S., Flavell, S. W., and Bargmann, C. I. (2015) Feedback from network states generates variability in a probabilistic olfactory circuit. *Cell,* **161**(2), 215–227.

[2] Roberts, W. M., Augustine, S. B., Lawton, K. J., Lindsay, T. H., Thiele, T. R., Izquierdo, E. J., Faumont, S., Lindsay, R. A., Britton, M. C., Pokala, N., Bargmann, C. I., and Lockery, S. R. (2016) A stochastic neuronal model predicts random search behaviors at multiple spatial scales in *C. elegans. eLife,* **5**, e12572.

[3] Aihara, K. and Matsumoto, G. (1982) Temporally coherent organization and instabilities in squid giant axons. *Journal of Theoretical Biology,* **95**(4), 697–720.

[4] White, J. G., Southgate, E., Thomson, J. N., and Brenner, S. (1986) The structure of the nervous system of the nematode *Caenorhabditis elegans. Philosophical Transactions of the Royal Society of London B: Biological Sciences,* **314**(1165), 1–340.

[5] Varshney, L. R., Chen, B. L., Paniagua, E., Hall, D. H., and Chklovskii, D. B. (2011) Structural properties of the *Caenorhabditis elegans* neuronal network. *PLoS Computational Biology,* **7**(2), e1001066.

[6] Bono, M. d. and Villu Maricq, A. (2005) Neuronal substrates of complex behaviors in *C. ELEGANS. Annual Review of Neuroscience,* **28**(1), 451–501.

[7] de Bono, M., Tobin, D. M., Davis, M. W., Avery, L., and Bargmann, C. I. (2002) Social feeding in *Caenorhabditis elegans* is induced by neurons that detect aversive stimuli. *Nature,* **419**(6910), 899–903.

[8] Liu, K. S. and Sternberg, P. W. (1995) Sensory regulation of male mating behavior in *Caenorhabditis elegans. Neuron,* **14**(1), 79–89.

[9] Raizen, D. M., Zimmerman, J. E., Maycock, M. H., Ta, U. D., You, Y.-j., Sundaram, M. V., and Pack, A. I. (2008) Lethargus is a *Caenorhabditis elegans* sleep-like state. *Nature,* **451**(7178), 569–572.

[10] Feng, Z., Li, W., Ward, A., Piggott, B. J., Larkspur, E. R., Sternberg, P. W., and Xu, X. Z. S. (2006) A *C. elegans* model of nicotine-dependent behavior: Regulation by TRP-family channels. *Cell,* **127**(3), 621–633.

[11] Goodman, M. B., Hall, D. H., Avery, L., and Lockery, S. R. (1998) Active currents regulate sensitivity and dynamic range in *C. elegans* neurons. *Neuron,* **20**(4), 763–772.

[12] Nickell, W. T., Pun, R. Y. K., Bargmann, C. I., and Kleene, S. J. (2002) Single ionic channels of two *Caenorhabditis elegans* chemosensory neurons in native membrane. *The Journal of Membrane Biology,* **189**(1), 55–66.

[13] Mellem, J. E., Brockie, P. J., Madsen, D. M., and Maricq, A. V. (2008) Action potentials contribute to neuronal signaling in *C. elegans. Nature Neuroscience,* **11**(8), 865–867.

[14] Ramot, D., MacInnis, B. L., and Goodman, M. B. (2008) Bidirectional temperature-sensing by a single thermosensory neuron in *C. elegans. Nature Neuroscience,* **11**(8), 908–915.

[15] Prevedel, R., Yoon, Y.-G., Hoffmann, M., Pak, N., Wetzstein, G., Kato, S., Schrodel, T., Raskar, R., Zimmer, M., Boyden, E. S., and Vaziri, A. (2014) Simultaneous whole-animal 3D imaging of neuronal activity using light-field microscopy. *Nature Methods,* **11**(7), 727–730.

[16] Nguyen, J. P., Shipley, F. B., Linder, A. N., Plummer, G. S., Liu, M., Setru, S. U., Shaevitz, J. W., and Leifer, A. M. (2016) Whole-brain calcium imaging with cellular resolution in freely behaving *Caenorhabditis elegans. Proceedings of the National Academy of Sciences of the United States of America,* **113**(8), E1074–E1081.

[17] Venkatachalam, V., Ji, N., Wang, X., Clark, C., Mitchell, J. K., Klein, M., Tabone, C. J., Florman, J., Ji, H., Greenwood, J., Chisholm, A. D., Srinivasan, J., Alkema, M., Zhen, M., and Samuel, A. D. T. (2016) Pan-neuronal imaging in

roaming *Caenorhabditis elegans. Proceedings of the National Academy of Sciences of the United States of America,* **113**(8), E1082–E1088.

[18] Hendricks, M., Ha, H., Maffey, N., and Zhang, Y. (2012) Compartmentalized calcium dynamics in a *C. elegans* interneuron encode head movement. *Nature,* **487**(7405), 99–103.

[19] Chalasani, S. H., Chronis, N., Tsunozaki, M., Gray, J. M., Ramot, D., Goodman, M. B., and Bargmann, C. I. (2007) Dissecting a circuit for olfactory behaviour in *Caenorhabditis elegans. Nature,* **450**(7166), 63–70.

[20] Clark, D. A., Biron, D., Sengupta, P., and Samuel, A. D. T. (2006) The AFD sensory neurons encode multiple functions underlying thermotactic behavior in *Caenorhabditis elegans. Journal of Neuroscience,* **26**(28), 7444–7451.

[21] Kato, S., Kaplan, H. S., Schrödel, T., Skora, S., Lindsay, T. H., Yemini, E., Lockery, S., and Zimmer, M. (2015) Global brain dynamics embed the motor command sequence of *Caenorhabditis elegans. Cell,* **163**(3), 656–669.

[22] Bargmann, C. I. and Horvitz, H. R. (1991) Chemosensory neurons with overlapping functions direct chemotaxis to multiple chemicals in *C. elegans. Neuron,* **7**(5), 729–742.

[23] Pierce-Shimomura, J. T., Morse, T. M., and Lockery, S. R. (1999) The fundamental role of pirouettes in *Caenorhabditis elegans* chemotaxis. *Journal of Neuroscience,* **19**(21), 9557–9569.

[24] Suzuki, H., Thiele, T. R., Faumont, S., Ezcurra, M., Lockery, S. R., and Schafer, W. R. (2008) Functional asymmetry in *Caenorhabditis elegans* taste neurons and its computational role in chemotaxis. *Nature,* **454**(7200), 114–117.

[25] Thiele, T. R., Faumont, S., and Lockery, S. R. (2009) The neural network for chemotaxis to tastants in *C. elegans* is specialized for temporal differentiation. *The Journal of Neuroscience,* **29**(38), 11904–11911.

[26] Satoh, Y., Sato, H., Kunitomo, H., Fei, X., Hashimoto, K., and Iino, Y. (2014) Regulation of experience-dependent bidirectional chemotaxis by a neural circuit switch in *Caenorhabditis elegans. Journal of Neuroscience,* **34**(47), 15631–15637.

[27] Iino, Y. and Yoshida, K. (2009) Parallel use of two behavioral mechanisms for chemotaxis in *Caenorhabditis elegans. Journal of Neuroscience,* **29**(17), 5370–5380.

[28] Wicks, S. R., Roehrig, C. J., and Rankin, C. H. (1996) A dynamic network simulation of the nematode tap withdrawal circuit: predictions concerning synaptic function using behavioral criteria. *Journal of Neuroscience,* **16**(12), 4017–4031.

[29] Rakowski, F., Srinivasan, J., Sternberg, P., and Karbowski, J. (2013) Synaptic polarity of the interneuron circuit controlling *C. elegans* locomotion. *Frontiers in Computational Neuroscience,* **7**, 128.

[30] Sakata, K. and Shingai, R. (2004) Neural network model to generate head swing in locomotion of *Caenorhabditis elegans. Network: Computation in Neural Systems,* **15**(3), 199–216.

[31] Kuramochi, M. and Iwasaki, Y. (2010) Quantitative modeling of neuronal dynamics in *C. elegans*. *Neural Information Processing. Theory and Algorithms: 17th International Conference, ICONIP 2010, Sydney, Australia, November 22-25, 2010, Proceedings, Part I,* pp. 17–24.

[32] Izquierdo, E. J. and Lockery, S. R. (2010) Evolution and analysis of minimal neural circuits for klinotaxis in *Caenorhabditis elegans*. *Journal of Neuroscience,* **30**(39), 12908–12917.

[33] Izquierdo, E. J. and Beer, R. D. (2013) Connecting a connectome to behavior: An ensemble of neuroanatomical models of *C. elegans* klinotaxis. *PLoS Computational Biology,* **9**(2), 1–20.

[34] Boyle, J., Berri, S., and Cohen, N. (2012) Gait modulation in *C. elegans*: An integrated neuromechanical model. *Frontiers in Computational Neuroscience,* **6**, 10.

[35] Kato, S., Xu, Y., Cho, C. E., Abbott, L. F., and Bargmann, C. I. (2014) Temporal responses of *C. elegans* chemosensory neurons are preserved in behavioral dynamics. *Neuron,* **81**(3), 616–628.

[36] Szigeti, B., Gleeson, P., Vella, M., Khayrulin, S., Palyanov, A., Hokanson, J., Currie, M., Cantarelli, M., Idili, G., and Larson, S. (2014) OpenWorm: An open-science approach to modeling *Caenorhabditis elegans*. *Frontiers in Computational Neuroscience,* **8**, 137.

[37] Hodgkin, A. L. and Huxley, A. F. (1952) A quantitative description of membrane current and its application to conduction and excitation in nerve. *The Journal of Physiology,* **117**(4), 500–544.

[38] Machado, P., Wade, J., and McGinnity, T. M. (2016) *Si elegans*: Modeling the *C. elegans* nematode nervous system using high performance FPGAS. *in Biosystems & Biorobotics - Advances in Neurotechnology, Electronics and Informatics, R.A. Londral and P. Encarnação (Eds.),* **12**, 31–45.

Chapter 2

Computational modeling of the spatio-temporal activity in a *C. elegans* sensory neuron

2.1 Abstract

Due to the huge number of neuronal cells in the brain and their complex circuit formation, computer simulation of neuronal activity is indispensable to understanding whole brain dynamics. Recently, various computational models have been developed based on whole-brain calcium imaging data. However, these analyses monitor only the activity of neuronal cell bodies and treat the cells as point unit. This point-neuron model is inexpensive in computational costs, but the model is unrealistically simplistic at representing intact neural activities in the brain. Here, I describe a novel three-unit Ordinary Differential Equation (ODE) model based on the neuronal responses derived

from a *Caenorhabditis elegans* salt-sensing neuron. I recorded calcium responses in three regions of the ASER neuron using a simple downstep of NaCl concentration. This simple ODE model generated from a single recording can adequately reproduce and predict the temporal responses of each part of the neuron to various types of NaCl concentration changes. My strategy which combines a simple recording data and an ODE mathematical model may be extended to realistically understand whole brain dynamics by computational simulation.

2.2   Introduction

Mathematical simulation of neuronal activity in the brain helps to describe neuronal encoding for certain animal behaviors and to estimate the circuit dynamics regulating those behaviors. Generating a general theory of neural encoding is a fundamental approach to model the whole brain circuit *in silico*. Simulation of whole brain dynamics can also systematically increase the understanding of the mechanism of neural coding of the sensorimotor integration system in animals [1]. Using calcium imaging methods, observations of neural activities in living animal brains has been performed. This approach enables us to analyze circuit dynamics for perception, memory formation, and decision making dependent on sensory inputs [2, 3, 4].

The nematode *Caenorhabditis elegans* has a simple nervous system consisting of only 302 neurons. The patterns of synaptic connectivity in these neuronal cells have been identified by anatomical studies [5, 6]. Real-time calcium imaging from a single-cell level to the whole-brain level can be applied in living worms [7, 8, 9], and

this can illuminate dynamic responses of individual neurons [10]. This simple, well-characterized nervous system, which is also suitable for imaging analyses, should be quite useful for analyses of neural coding by integrating actual neuronal activity from *in vivo* imaging and computational modeling based on that data. Kato *et al.* successfully applied the integration method and demonstrated a close relationship between sensory-neuronal dynamics and sensory-driven behaviors [11]. However, because this research only treats the activity of cells as a point-unit, it is not clear whether the morphology of the neuronal cells affects to these integration analyses of whole brain activity or not. To handle intrinsic neuronal activities in the brain for computational simulation, a simple model with a smaller number of parameters that can reproduce the various characteristics of neuronal activity is preferable. One of the simple models is Izhikevich's spiking neuron model which uses only four parameters and can reproduce the spiking and bursting patterns of cortical neurons [12]. Hence, Izhikevich's model is suitable for exhaustive simulation of neural information processing with a low computational burden [13]. *C. elegans* neurons also show various patterns of responses to several external stimuli [14], however, Izhikevich's spiking neuron model cannot be applied directly to *C. elegans* neurons since voltage-sensitive sodium channels have not been identified in the *C. elegans* genome [15, 16]. On the other hand, to simplify the analytical method of neural information processing in the worm, a point-neuron model for neuronal activity has been described [11, 17, 18, 19, 20, 21, 22]. The point-neuron model neglects the spatial structure of the cell(s) to decrease numerical costs for simulations. To address phenomenological analysis in neural circuit dynamics in the animal, however, each neuronal activity should be analyzed based on

37

its temporal and spatial resolution. Recent studies also indicate that compartmentalized activities at distinct regions of the neurites exist [23, 24, 25], suggesting that *C. elegans* neurons should be handled as a multi-unit to build a reliable simulation model. As for a detailed multi-unit model, partial differential equations (PDE) are known to well represent the spatio-temporal activity of single neuron [26]. However, PDE models are numerically or computationally prohibitive for a large neural circuit like a whole brain [27]. Thus, generating a multi-unit model which involves the native morphology and the activity of a *C. elegans* neuron should be quite helpful for simulating whole-brain circuit activity underlying certain behaviors in this animal.

In this chapter, I first characterized the spatio-temporal calcium activity of a salt-sensing neuron ASER in *C. elegans* with a simple step-down stimulus of NaCl concentration. To build a better mathematical model for intact nervous systems, temporal calcium responses from the dendrite, soma, and axon were observed, and the responses from all parts of the ASER neuron showed similar dynamics. These temporal responses were simple: they peaked within several seconds and decayed slowly until the concentration was increased to a higher one. Based on these actual neuronal-calcium-responses, I constructed a three-unit Ordinary Differential Equation (ODE) model which can predict the spatio-temporal responses of the ASER neuron to various types of NaCl concentration stimuli [28].

2.3 Materials and methods

2.3.1 Strains

The strain used for calcium imaging was *taEx138* [*Pgcy-5:: G-GECO1.2*]. Worms were cultivated on standard NGM agar plates seeded with *E. coli* strain OP50 at room temperature ($\sim$ 22 °C).

2.3.2 Molecular biology and transgenic animals

The *Pgcy-5:: G-GECO1.2* DNA construct for the ASER calcium imaging was generated by first inserting the G-GECO1.2 [29] sequence between the AgeI and *Eco*RI site of the pPD95.79 vector (kind gift from Andy Fire). Then, a 3.0 kb *gcy-5* promoter region was inserted between the SphI and SmaI site of the pPD95.79/G-GECO1.2 plasmid. The resulting plasmid was injected into Bristol (N2) animals at a concentration of 50 ng/μl with the *Plin-44:: mCherry* injection marker using a standard microinjection method [30].

2.3.3 Calcium imaging

One or two day old adult transgenic worms were used for imaging. Worms were immobilized in a microfluidic device fabricated from polydimethylsiloxane (PDMS) (Fig 1) [31]. The microfluidic device was set on an inverted fluorescent microscope (Olympus IX71), and time-lapse images were performed using an ORCA-Flash 4.0 CCD camera (Hamamatsu Photonics) controlled by HCImage software (Hamamatsu

Photonics). Recordings were started within 3 minutes after removal from food, and images were captured at the rate of 10 frames/sec. The following compositions of buffers for calcium imaging were used: (in mM) 5 KPO_4 (pH 6.0), 1 $CaCl_2$, 1 $MgSO_4$, and 0-50 mM NaCl for the stimulation. All the buffers were adjusted to be 350 mOsmol/L H_2O with glycerol [32]. The patterns of salt stimulation were automated by using the Perfusion Valve Controller System VC-6M (Warner Instruments) and Arduino microcontroller to control solenoid valves (Arduino SRL) with a pre-generated sequence. A pseudorandom pattern of 50 mM/0 mM NaCl concentration change was generated by Mersenne Twister [33]. I used both $\Delta F/F_{max}$ and $\Delta F/F_0$ for values of fluorescence intensity change. For analysis of temporal dynamics of each region in the cell, the $\Delta F/F_{max}$ value was linearly scaled from 0 to 1 with formula $(F - F_{min})/(F_{max} - F_{min})$. F_{max} is the maximum value of the fluorescence intensity, whereas F_{min} is the minimum value of the fluorescence intensity. The $\Delta F/F_0$ value was used to compare the neuronal activity to the NaCl concentration changes. F_0 was defined as the average fluorescence in a 5 s window before stimulation. After background subtraction, the total fluorescence intensity was measured from individual regions of interest (ROIs) in the ASER neuron. Photo-bleaching was corrected by fitting a single exponential before and after stimulation and removing the latter by fitted curve.

A computational model for the spatio-temporal activity in a single neuron

The three-unit ODE model to quantitatively describe spatio-temporal dynamics of a *C. elegans* neuron was formulated as follows:

$$\text{Dendrite} \qquad \tau_d \frac{dx_d}{dt} = -x_d + y_d + D(W_d x_s - x_d) + I(t), \qquad (2.1)$$

$$\text{Soma} \qquad \tau_s \frac{dx_s}{dt} = -x_s + Y_s y_s + D(x_d + x_a - x_s), \qquad (2.2)$$

$$\text{Axon} \qquad \tau_a \frac{dx_a}{dt} = -x_a + Y_a y_a + D(W_a x_s - x_a), \qquad (2.3)$$

where x_d, x_s, and x_a are intracellular calcium dynamics in each region and represent neuronal activities. Time constants are given as $\tau_d = 1.4$ s, $\tau_s = 3.7$ s, $\tau_a = 1.2$ s from the calculation of imaging data (Fig 2). The variable y_i is:

$$\frac{dy_i}{dt} = -Ax_i \quad (i = d, s, a). \qquad (2.4)$$

y_i represents a inactivation variable and provides negative feedback to x_i. y_i describes the slow delayed-decay during the decrease of NaCl concentration in Fig 2. A classic leaky integrate-and-fire model, which does not have an inactivation variable y, cannot reproduce well this delayed-decay response, because neuronal response converges to

41

a peak response during pulse input [11]. I thus hypothesized that temporal dynamics of this delayed-decay is represented by the inactivation variable which is formulated by the first order differential equation dependent on the self-activity. In addition, I also hypothesized that y_i is zero before and after the stimulus presentation. Without this assumption, the simulated trace shows a hyperpolarized response by negative feedback to x_i. However, the imaging results showed that the ASER response was not hyperpolarized after stimulation (Fig 2). For simplicity, in the ODE model, the y_i works only during the presentation of the input stimulus. The parameter A describes the timescale of the inactivation variable y_i. Smaller value results in slower inactivation. The parameters Y_s and Y_a describe the magnitude of the inactivation variable y_i to express decay process during the downstep of NaCl stimulation in soma and axon respectively. The magnitudes of decay response during the 0 mM NaCl presentation were different in each unit (Fig 2). I thus decided to use different parameters for the magnitudes of the inactivation variable in each unit.

The parameter D describes a coupling constant in each unit through calcium diffusion. The variables W_d and W_a describe weights in each unit through calcium diffusion from soma. In the ODE model, I hypothesized that calcium can diffuse from soma to both dendrite and axon, and that the diffusion effect from soma depends on the state of dendritic- and axonal-activity. If the dendrite has a high-activity, W_d is smaller than W_a. On the other hand, if the axon has a high-activity, W_d is bigger than W_a. Details for W_d and W_a setting are shown in Table 1.

In the ODE model, x_i and y_i are dimensionless variables, and D, Y_s, Y_a, and A are dimensionless free parameters, where t is the time. The initial condition of

x_i and y_i is zero. The free parameters were optimized from calcium responses to a simple pulse-like stimulation (Fig 2) by using optimization methods (Table 2). $I(t)$ is the input stimulus to the downstep in NaCl concentration. For a simple step-like simulation, $I(t)$ is defined as 1.0 or 0.0, respectively, when the worm is exposed to 0 mM or 50 mM NaCl. For the flickering- or randomized-stimulation, the ASER neuron was stimulated with $I(t) = 1.5$ or 1.0 as the downstep in NaCl concentration, and with $I(t) = 1.0$ or 0.5 as an upstep in NaCl concentration to reproduce better performance of simulation.

Environment of computer simulation

The computational model was implemented using C on a UNIX workstation in which the fourth-order Runge-Kutta method with adaptive time steps was included [34].

Optimization of free parameters

For modeling, the combination of free parameters D, Y_s, Y_a, and A was defined using two methods. I first determined the range of each free parameter that reproduces the corresponding *in vivo* calcium response data (Fig 2) based on the results of pilot simulations (Table 3). In this pilot simulation, I simulated all the combinations of free parameters (8,000,000) for adequate search ranges of free parameters (see Fig 3). Next, I applied the Genetic Algorithm (GA) to determine the optimal combination of free parameters in the neuronal models. GA is an evolutionary method used in a heuristic parameter search [35]. An initial population of 100 individuals eight

43

binary character lengths was generated by random selection in each parameter range. Crossover was set to generate the next individuals (offspring) using two randomly-selected current individuals (parents). I defined that a crossover will occur at any randomly-selected points with probability 0.6. The first offspring was generated by combining with the former part of male parent and the latter part of female parent, and vice versa for the second offspring. Bit lengths from male or female parent were dependent on the point of crossover. Randomly-selected bits of individuals were inverted by mutation of the bit strings with mutation probability 0.01. The fitness of all individuals was evaluated by comparing their simulation results (neuronal responses) with the *in vivo* imaging data of the downstep of NaCl concentration for 60 seconds. The fitness function (Euclidean distance between two neuronal activities related to the downstep of NaCl concentration for 60 seconds) was defined as follows:

$$dL = \sum_{t=0}^{120} \left(|f_d(t) - \hat{x}_d(t)| + |f_s(t) - \hat{x}_s(t)| + |f_a(t) - \hat{x}_a(t)| \right), \tag{2.5}$$

where $f_i(t)$ is the calcium responses from actual imaging in each region (Fig 2). $\hat{x}_i(t)$ is the simulated responses in each region. The actual- and simulated-responses are linear scaled from 0 to 1. dL is the summation of differences between $|f_i(t)|$ and $|\hat{x}_i(t)|$ for 120 s with interval 0.1 s in all the regions. Smaller values of dL indicate better fitness. The populations of parameter sets evolved up to 500 generations. Optimization of parameter set was repeated 18 times using the initial population with different random seeds in GA. Pseudorandom numbers were generated for GA by Mersenne Twister. In addition to GA, I also used the Brute Force (BF) approach

44

to identify a parameter set expected to fit well to the imaging data in Fig 2. All combinations of free parameters (approximately 1,200,000) were simulated by the BF approach, and their fitness were compared to the GA approach. This dL was calculated only for the optimization of free parameters from calcium responses to a simple pulse-like stimulation.

2.3.4 Evaluation of the model performance

The output responses from the model were evaluated by analyzing the variance accounted for (VAF) values as follows:

$$\text{VAF} = 100 * \left(1 - \frac{\text{var}(x - \bar{x})}{\text{var}(x)}\right).\tag{2.6}$$

This VAF index was proposed for the evaluation of model performance as scales relative to the variance of the simulated trace [11, 36]. A model is evaluated as showing good performance when a high VAF is derived from the model. A lower value, however, indicates that the resulting response does not fit the actual imaging data.

2.4 Results

2.4.1 Characteristics of the ASER calcium response to the NaCl concentration step change

Calcium imaging techniques are suited for evaluating neuronal activities in *C. elegans* as endogenous voltage-sensitive sodium channels have not been identified in the *C. elegans* genome [15, 16]. Instead of the sodium-based classical action potential, *C. elegans* neurons likely to use calcium-based signal amplification for generating currents as in the large nematode *Ascaris* [37, 38, 39].

To build a temporal- and spatial-reconstitution model for neuronal activity in *C. elegans*, I analyzed calcium responses in each part of the ASER neuron and tried to understand how salt information is propagated in the dendrite, soma, and axon of this neuron (Fig 1). The ASER neuron is activated by the decrease in NaCl concentration [40] and mediates chemotaxis behaviors by controlling reorientation movements in response to salt gradients [41, 42, 43, 44, 45]. I applied downstep changes in NaCl concentration from 50 mM to 0 mM to transgenic animals expressing G-GECO1.2 protein [29] specifically in the ASER neuron. The duration of 0 mM portion was ranged from 3 s to 60 s, and responses in each part of the neuron were compared (Fig 2 and data not shown). Calcium responses in all the regions of the ASER neuron showed similar patterns of activity; they rose slowly after the downstep of NaCl concentration, and $\Delta F/F_{max}$ value reached its peak position several seconds after changing to 0 mM NaCl (Fig 2 and data not shown). After reaching peak response, the calcium

46

response gradually decayed during the downstep to 0 mM NaCl concentration. This decay process during the downstep to 0 mM NaCl concentration lasted until the NaCl concentration was restored to 50 mM (Fig 2). After the NaCl concentration reached 50 mM (upstep), the ASER activity rapidly returned to the basal, steady state activity. These features of calcium responses which take a few seconds to a peak response and decay slowly during the 0 mM NaCl presentation, were consistent with previous studies [32, 40, 44]. Using the responses to the 60-second downstep stimulation, I quantitatively analyzed their temporal activity (Fig 4). Response to the peak was fastest in the axon compared to other regions (Fig 4A). The decay responses during the downstep to 0 mM and at the upstep to 50 mM in the axon were also faster than that of soma or dendrite (Fig 4B, C). These results indicate that all regions of the ASER neuron are rapidly activated upon the decrease in NaCl concentration, suggesting that signals detected by the cilia rapidly propagate into the dendrite and spread to both soma and axon.

2.4.2 Modeling of spatio-temporal dynamics in the ASER neuron

Based on the calcium imaging as indices of neuronal activity, I constructed a mathematical model that describes the temporal dynamics of the dendrite, soma, and axon in the ASER neuron (Fig 5). In the simulation process, the free parameters (D, Y_s, Y_a, and A) were optimized by two methods, Brute Force (BF) search and genetic algorithm (GA) (Table 2), and the resulting responses were compared with actual

47

imaging data (Fig 6–8). Both parameter-search methods gave quite similar response curves in all regions of the neuron (Fig 6), and showed low error if best 100 parameter combinations were used in BF (Fig 7A). However, the BF parameter-search using worst 100 data showed quite high error (Fig 7A). Considering the number of trial in parameter search (about 50,000 patterns in GA vs. 1.2 million patterns in BF), GA was more effective than BF when the number of generations increased (Fig 7B). Although several discrepancies were observed between actual imaging data and simulation data such as the $t_{1/2}$ decay to the 50 mM upstep in the dendrite (Fig 8C), most temporal parameters from simulation seem to be quite similar to those of actual imaging data (Fig 8A, B). This is also confirmed by calculating VAF values in each region: all the percent VAFs were more than 90% (Fig 8D). These results suggest that three-compartment ODE model in combination with the GA parameter optimization can effectively reproduce the spatio-temporal activity of the actual ASER neuron in response to the step change in NaCl concentration.

2.4.3 Neuronal and computational responses to rapidly-flickering stimuli

The three-unit ODE model was developed by using a single stimulation: 50 mM to 0 mM downstep in NaCl concentration change for 60 seconds. I asked whether this ODE model could predict neuronal responses triggered by other types of stimulations such as weak concentration changes, short-period continuous concentration change, and so on. First, I applied a rapidly-flickering concentration change of NaCl which

may be a more realistic model stimulation for naturally-living worms. I changed the concentration at 1/2 frequency, the rate of worm's head swing during forward movement. At the onset of the flickering stimulus, gross neuronal activity was observed and this gross activity gradually decreased during the input stimulus (Fig 9, 11, 12). Similar to the simple one-downstep stimulation, it took several seconds to reach the peak response, and the response decayed slowly until the concentration returned to the basal 50 mM level. At high magnification, I found that calcium concentration in ASER rapidly increased and decreased following the NaCl concentration change (Fig 10). This indicates that water-soluble chemosensory neurons can respond to such quickly-repeated stimuli. These quick responses were observed in all regions of the neuron (Fig 9–12). The same frequency of input-output stimulation was applied to the three-unit ODE model, and I found that the response was quite similar to that of calcium imaging data. The VAF value in the dendrite was relatively low, but in the soma and axon matched to the living cell responses (Fig 13). Thus, model can predict the neuronal response corresponding to a fast-flickering stimulation.

2.4.4 Prediction of neuronal responses to unfixed, randomized changes of stimulus

Animals may remain in one field with a fixed environment but walk randomly around to find better conditions. This random movement presents a random change of stimulation to sensory neurons. So I simulated the temporal activity of ASER with a pseudorandom pattern of input stimuli applied (Materials and Methods). The response

from the ODE simulation showed quite similar pattern of activity to the imaging response (Fig 14–16). Similar to the quick flickering stimulation, the VAF value in the dendrite was relatively low compared to other regions of the neuron, but the soma and axon responded with almost the same time resolution (Fig 17). I also found that during a long stimulation, the amplitude of neuronal response in the simulation was maintained, but that of actual response gradually decreased (Fig 14–16). These data suggest that the three-unit ODE model can effectively predict *in silico* the patterns of neuronal activity mimicking natural behaviors despite the fact that the modeling was constructed using the ASER response to a simple downstep concentration change.

2.4.5   Neuronal responses to various NaCl concentration changes

The concentration change of NaCl between 50 mM and 0 mM is much larger than the NaCl gradients encountered by moving worms under living (physiological) environments. I applied various patterns of NaCl concentration change, and validated whether the three-unit ODE model could predict neuronal responses to any NaCl concentration changes (Fig 18–26). As shown in Fig 18, somatic responses to NaCl concentration changes were observed from a 1 mM change to the 30 mM change. The response curves for over 10 mM concentration changes were similar to that of 30 mM change; it takes a few seconds to reach peak response, and the response decays slowly until the next upstep of NaCl concentration is presented to the worms. However, the peak responses were significantly reduced when the NaCl concentration changes smaller than 10 mM change were applied to worms. Although decay process after the

peak response in the simulation was slower compared to the actual calcium imaging data, the three-unit ODE model also showed the same response curves as the experimental responses. In fact, the VAF values were decreased when the concentration change was less than 10 mM change, suggesting that this model may not be suitable to predict the response to slight concentration changes (Fig 19). As with somatic responses, I also observed that the dendritic and axonal responses were dependent on the difference in NaCl concentration (Fig 21, 24). According to imaging analyses, the simulation model can predict neuronal responses well when the salt concentrations gradients are higher than 10 mM change.

In these analyses, the peak calcium responses were not proportional to the concentration differences in NaCl but were sigmoidal (soma in Fig 20A, dendrite in Fig 23A, axon in Fig 26A). In simulation, I set the input stimulus to be proportional to the difference of NaCl concentration. The peak responses were proportional to the input stimuli, and those responses did not correspond to the actual responses (Fig 20B, 23B, 26B). However, the peak transition pattern to the input stimulus seemed to be similar to that of actual neuronal response if a sigmoidal transfer function was applied to the peak neuronal activity $x(t)$ (Fig 20C, 23C, 26C). Thus, actual imaging analysis suggests that the relationship between the ASER neuronal activity and NaCl concentration changes is not proportional but sigmoidal.

2.5 Discussion

This study used a calcium imaging method to characterize the spatio-temporal activity in the salt-sensing ASER chemosensory neuron in response to various patterns of NaCl stimulation. By adopting the actual neuronal responses by this calcium imaging, I constructed a novel mathematical model named the three-unit ODE model. Surprisingly, this model successfully reproduced the spatio-temporal activity of this neuron to not only a simple downstep-concentration change but also to the various types of stimuli such as randomized concentration changes (Fig 6, Fig 9–12, Fig 14–16), despite the three-unit ODE model was constructed based on calcium responses to a simple sensory stimulation. This finding implies that a computational model in *C. elegans* can be developed relatively easy from the neuronal response to a simple pulse-like stimulation.

The temporal responses of the ASER neuron to the NaCl concentration changes have been well characterized. This calcium imaging data also showed the simple temporal responses to the 50-0 mM downstep of concentration: a relatively fast activation and slow decay followed by peak response during the downstep of NaCl concentration. Although differences of time constants were observed among three regions, all the responses showed similar temporal dynamics to various types of NaCl stimuli. In addition, compartmentalized activity was not observed in both neurites of this neuron as reported in other *C. elegans* neurons [23, 24, 25]. These results suggest that the signal can be rapidly transmitted from the cilia to the axon terminal of this cell. I have also shown that in the imaging analysis, calcium goes up and down faster in the

axon (also up faster in the dendrite) than in the soma (Fig 2, 4). What factor does influence the time constant of calcium dynamics in each region? The simple answer may be the volume of regions. In the large space of soma, calcium influx or diffusion into the soma may be slow down, and calcium binding to the G-GECO protein can be slow even if the similar concentration of the reporter molecule exists. Alternatively, the number of voltage-sensitive Ca^{2+} channels on the plasma membrane may not be uniform among these regions. For example, UNC-2, a calcium channel alpha subunit similar to the human P/Q-type calcium channel, has been shown to localize as puncta on the axon of the AWC chemosensory neurons [46]. This kind of heterogenous localization of Ca^{2+} channels has been shown to localize predominantly at neurites, not at soma. On the other hand, upstepping to 50 mM NaCl concentration rapidly inactivated the ASER, meaning calcium exclusion or sequestration from the cytosol by as yet unidentified mechanisms. This fast activation and inactivation mechanism are probably required for proper response of the ASER neuron to a continuous rapidly-flickering concentration change, as I have first shown in this study. Not only ASER, but other chemosensory neurons AWC and ASH are known to respond temporally to a rapidly-flickering stimulus faster than 1.0 Hz, the timescale of one head swing [11]. Those data suggest that most *C. elegans* sensory neurons may potentially respond to fast input stimuli according to worm movement. In addition to fast response, tha axonal quick-response (Fig 2, 4) may work for effectively information processing in neural circuit. Increase of intracellular calcium ion causes neurotransmitter release from synaptic vesicles by exocytosis [47]. The axonal calcium response in sensory neurons thus might be suitable for transmission of fast information flow.

My novel neuronal model is based on data from a simple step-down stimulus applied for 60 seconds, and this model can represent the spatio-temporal activity of the single neuron when the same stimulus was applied (Fig 6). In addition, the simulation also fit well with the actual neuronal response to a short flickering stimulus pattern (Fig 9–12). However, the simulated response did not correspond to real neuronal activity in the peak response magnitude; magnitude of the peak height in the simulation was remained relatively constant during stimulation, but in live animals, it gradually decreased over the one-min stimulation (Fig 10B). This feature was also observed when a pseudorandomized concentration change was used for a stimulation pattern (Fig 14–16). Similar adaptive responses to fluctuating stimuli in the AWC and ASH neurons are seen in the *C. elegans* chemosensory system [11]. Thus, it is probably true that *C. elegans* sensory neurons have sensory adaptation mechanisms. To improve the three-unit ODE model, these adaptive responses should be included by adding several parameters. In addition, this ODE model cannot reproduce quantitative neuronal activity to the temporal responses of each unit for large or tiny changes of NaCl concentrations. The actual imaging data suggests that the response of ASER neuron is not linear to the step changes of NaCl concentration but seems to be sigmoidal (Fig 20A, 23A, 26A). However, these simulations showed that the relationship between the peak of the neuronal response and $I(t)$ are a linear to from 0.0 to 30.0 (Fig 20B, 23B, 26B). In addition, the responses to smaller concentration changes showed weak discrepancies with live imaging responses. Thus, a sigmoidal transfer function to the simulated responses was required to fit simulated peak responses to actual neuronal responses observed in various step changes in NaCl concentra-

54

tion (Fig 20C, 23C, 26C). This sigmoidal shape of stimulus/response relationship indicates a threshold range in ASER sensitivity, as seen in other *C. elegans* sensory neurons [48, 49]. By examining the threshold range to NaCl concentration change in the ASER neuron or that of other sensory neurons, I will improve the three-unit ODE model to quantitatively estimate neuronal responses to various ranges of external stimuli. In addition, this sigmoidal transfer allows to predict the peak responses of ASER neuron caused by various input stimuli. It is also possible to estimate a NaCl-concentration environments from actual neuronal activity, by using this ODE model with sigmoidal transfer.

Several functions in the proposed the neuronal response model should be issued to support the interpretation biophysically. The first issue is the inactivation variable y_i in the equation (2.4). This variable represents slow delayed-decay during a stimulation (decrease in NaCl concentration). A classic leaky integrate-and-fire model cannot reproduce well this delayed-decay response, because neuronal activity converges to a peak response level during pulse input [11]. Therefore, I supposed that temporal dynamics of this delayed-decay in the ASER neuron might be represented adding an inactivation variable which is formulated by first order differential equation dependent on the self-activity. As expected, the simulated responses were well fit to actual imaging data (Fig 6). A short-period of stimulation such as the 3-second stepdown to 0 mM from 50 mM NaCl concentration does not require this variable, but several *C. elegans* neurons show similar kinds of decay response [11, 24]. Considering the fact that the inactivation variable y_i does not affect to represent the response patterns to short-period stimulations (data not shown), this variable can support to simulate

neuronal responses to any types of stimulation. The second issue is on the coupling constant D, which is the third term in the equation (2.1)–(2.3). This parameter was set to represent calcium diffusion in each unit of the ASER neuron and works for uniform activities in each unit. Although the three-unit ODE model is not represented as a term of calcium influx through voltage-sensitive channels on the soma and axon, calcium responses in each unit are reproduced well. Therefore, the calcium dynamics in the ASER neuron may be largely dependent on calcium diffusion more than calcium influx through voltage-sensitive channel, which may influence on the several parameters of the response curve such as the time constant to the peak response.

As shown simulation results, VAF index in the dendrite was relatively low for flickering- and randomized-stimuli (Fig 13, Fig 17). The low values in VAF do not indicate the bad performance in this ODE model. Because this ODE model has approximately same performance in the previously proposed models [11, 36] for VAF index (Table 4). Moreover, this ODE model also has the following advantage over the previously proposed models: This ODE model can predict the neuronal responses to unknown stimulus-patterns (Fig 9–12, Fig 14–16), despite model parameters and functions were determined based on calcium responses to a simple sensory stimulation (Fig 2). On the other hand, in previous studies, model parameters and response functions were determined respectively based on imaging data with each trials which were recorded neuronal response to input stimuli. Their model thus can reproduce to the neuronal response for known stimulus-pattern, however has an insufficient for predicting the neuronal response for unknown stimulus-pattern.

My final goal is to develop a whole brain, neural computation model which is

based on *in vivo* imaging of the *C. elegans* nervous system. Although I did not found large differences in neuronal responses of three regions, *C. elegans* neurons should be handled as a multi-unit to establish a reliable simulation for network modeling. The point-unit model is well suited for simulation of circuit analysis, but this model bypasses the morphology of each neuron in the circuit. On the other hand, a detailed multi-unit model, which involves complicated morphology of each neuronal cell, is computationally expensive for large-scale network simulations. In consideration of these restrictions, I constructed a three-unit ODE model for addressing both disadvantages. The single neuron is divided into three units based on its basic morphology, and each unit in the proposed ODE model depends only on time. The three-unit ODE model is more physiologically reliable than a point-unit model and is easier to handle analytically and numerically than other multi-unit models. Not only three major regions of the ASER neuron, furthermore, I can also apply the three-unit ODE model to reproduce compartmentalized calcium dynamics on neurites, which are reported in several *C. elegans* neurons [23, 24, 25]. Although several modifications will be required in the term of diffusion of this equations, I believe extensibility of the modeling to several types of neuronal activity *in vivo*. I also propose GA for the parameter estimation of a large-scale network modeling. In the present study, selected parameters from GA showed compatible responses to those from the best BF samples.

In this study, by integrating *in vivo* imaging and *in silico* simulations, I have successfully constructed a simple phenomenological model for a *C. elegans* neuronal activity. I am also trying to fuse the proposed ODE model with a synaptic integration model to understand the neural information processing for salt-chemotaxis behavior.

57

A graded synaptic transmission has modeled as a sigmoidal function dependent on its presynaptic activity [21, 50, 51]. By simply assuming a small coupling constant D in each synaptic region, the proposed neuronal model with synaptic integration can estimate the responses in each compartmentalized subcellular region. This may be, unlike other point-neuron models, a strong advantage for whole-brain modeling in *C. elegans*, and also will be helpful to figure out mechanisms of sensorimotor integration in animals.

Table 1: **Variables W_d and W_a.**

	$x_a > 0$	$x_a < 0$	$x_a = 0$
$x_d > 0$	$W_d = |x_a|/(|x_d| + |x_a|)$	$W_d = 0$	$W_d = |x_a|/(|x_d| + |x_a|)$
	$W_a = |x_d|/(|x_d| + |x_a|)$	$W_a = 1$	$W_a = |x_d|/(|x_d| + |x_a|)$
$x_d < 0$	$W_d = 1$	$W_d = |x_d|/(|x_d| + |x_a|)$	$W_d = 1$
	$W_a = 0$	$W_a = |x_a|/(|x_d| + |x_a|)$	$W_a = 0$
$x_d = 0$	$W_d = 0$	$W_d = 0$	$W_d = 0$
	$W_a = 1$	$W_a = 1$	$W_a = 0$

Table 2: **Averaged parameters used in the three-unit ODE model.**

Parameters	BF (best)	BF (worst)	GA
D	7.300000 ± 0.180348	0.500000 ± 0.000000	7.1 ± 0.2
Y_s	-0.224000 ± 0.00668	-0.14200 ± 0.08181	0.3 ± 0.0
Y_a	-0.047000 ± 0.012099	-0.246000 ± 0.086753	-0.2 ± 0.0
A	0.105200 ± 0.00244	0.280700 ± 0.000987	0.03 ± 0.0

Table 3: **Ranges of free parameters for BF and GA.**

Parameters	Range	Step size
D	$[0.1, 10]$	0.1
Y_s	$[-1, +1]$	0.1
Y_a	$[-1, +1]$	0.1
A	$[0, 0.3]$	0.01

Table 4: **Comparison of neuronal models.**

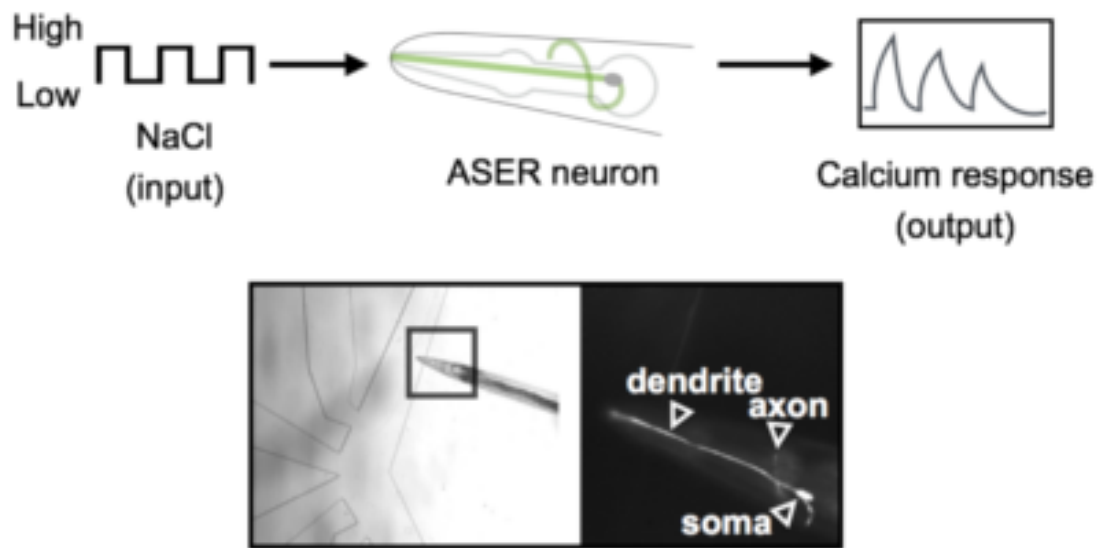| Model	Unit	Free Parameters	Performance (VAF)	Formula
Three-unit ODE model [28]	multi	5	40-90%	Differential equation (nonlinear)
Kato's model [11]	single	5	69-96%	Differential equation (linear)
Tsukada's model [36]	single	3	40-90%	Linear-convolution model (impulse response function)

Figure 1: **Schematic of the experimental set-up to measure calcium response in the ASER neuron.** An identification method of the neuronal-response property in ASER to NaCl stimulation. The worm is fixed with PDMS chip (bottom). Calcium responses of dendrite, soma, and axon were recorded from transgenic worms expressing calcium-sensitive probe G-GECO1.2.
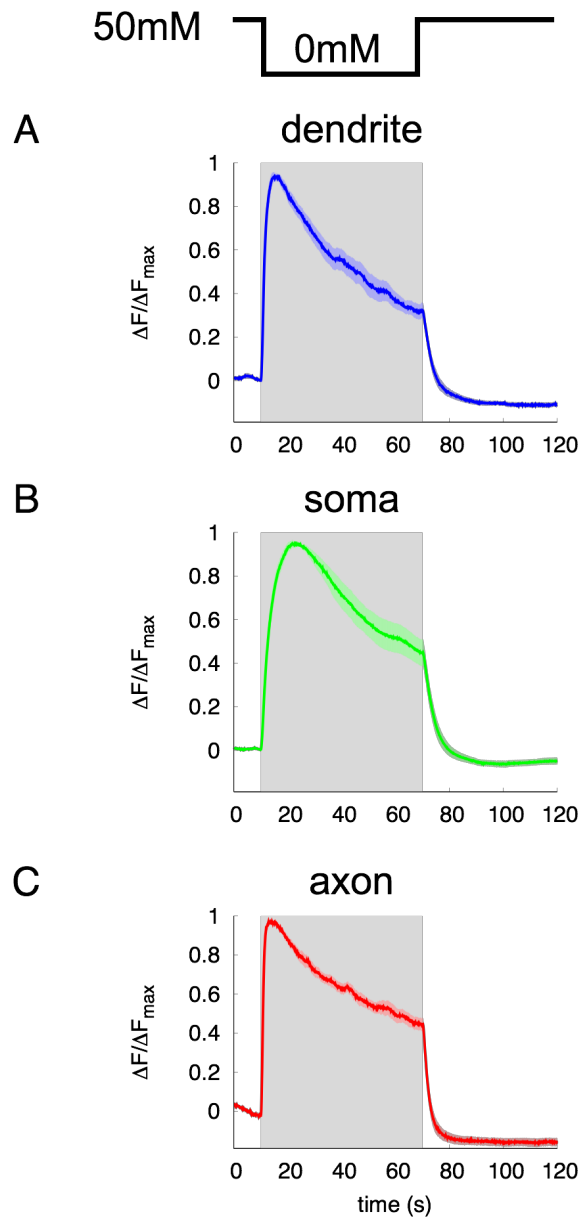
Figure 2: **Normalized calcium dynamics in the dendrite, soma, and axon of the ASER neuron to step changes in NaCl concentration stimuli.** Gray shading denotes the 60-sec downstep to 0 mM NaCl concentration from 50 mM NaCl ($t = 10 - 70$ s). Solid lines represent average data, and the lightly colored region around each line shows SEM.
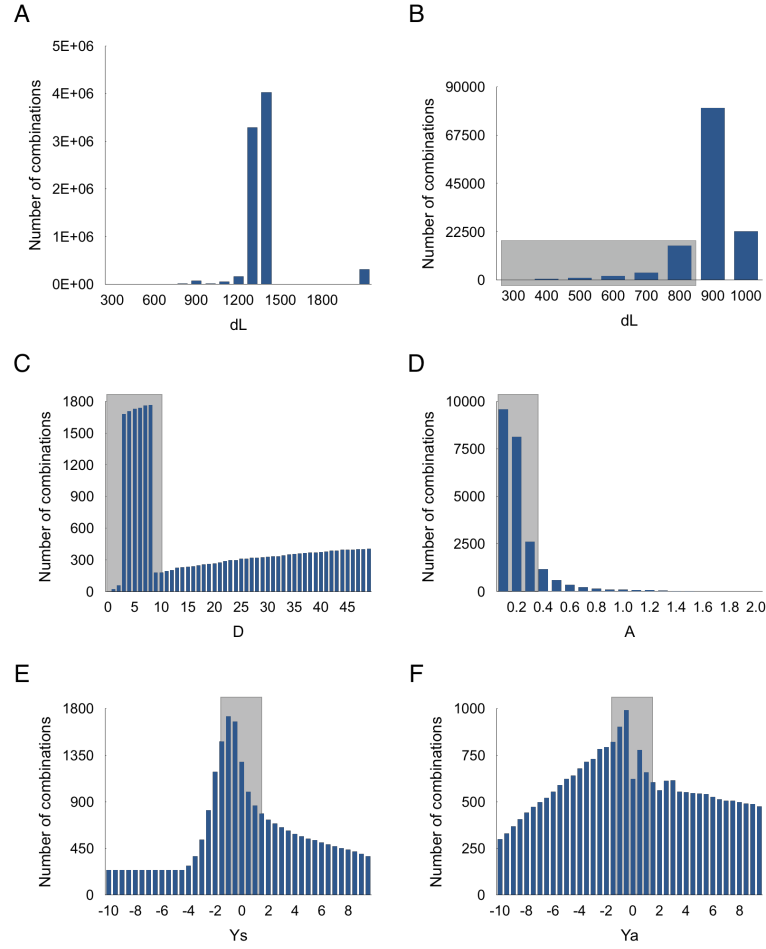
Figure 3: **Adequacy evaluation of free parameters.** All the combinations of free parameters (8,000,000) were simulated by the equation (1)–(4) using following ranges: $D[0, 50]$; $A[0,10]$; Y_s[-10, 10]; Y_a[-10, 10]. dL in the equation (5) was calculated from both simulation results and imaging data (Fig. 2). (A) All combinations were classified based on the dL value. Smaller dL indicates a higher reproducibility. Over half combinations are included into the range over $dL \geq 1300$. (B) Histogram of dL value less than 1,000. The number of combinations is decreased according to smaller dL values. The combinations, whose dL was less than 800, were analyzed for the adequacy evaluation of free parameters (gray-shading area). (C) Histogram of the D values. Selected combinations in (B) were classified based on their D values. Gray shading denotes the range of D used in simulation. (D) Histogram of the A value. Same combinations in (C) were classified based on their A values. Gray shading denotes the range of A used in simulation. (E) Histogram of the Y_s value. Same combinations in (C) were classified based on their Y_s values. Gray shading denotes the range of Y_s used in simulation. (F) Histogram of the Y_a value. Same combinations in (C) were classified based on their Y_a values. Gray shading denotes the range of Y_a used in simulation.
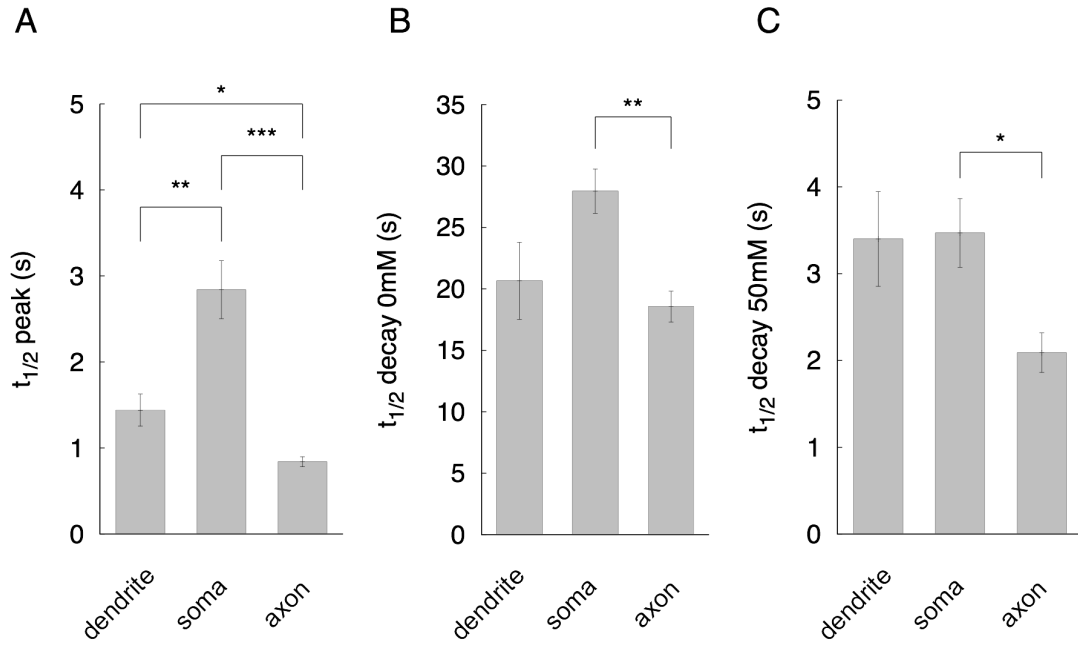
65

Figure 4: **Characteristics of the spatio-temporal response in the ASER chemosensory neuron to step changes in NaCl concentration stimuli.** (A) Time constant to achieve peak response during downstepping of the NaCl concentration. (B) Decay time from peak response to just before the upstep of the NaCl concentration. (C) Decay time back to baseline after the upstep of NaCl concentration. Error bars represent SEM. n = 10, $*p < 0.05$, $**p < 0.01$, and $***p < 0.001$ by Games Howell test.
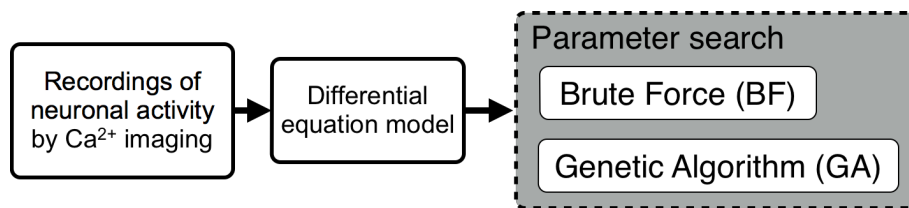
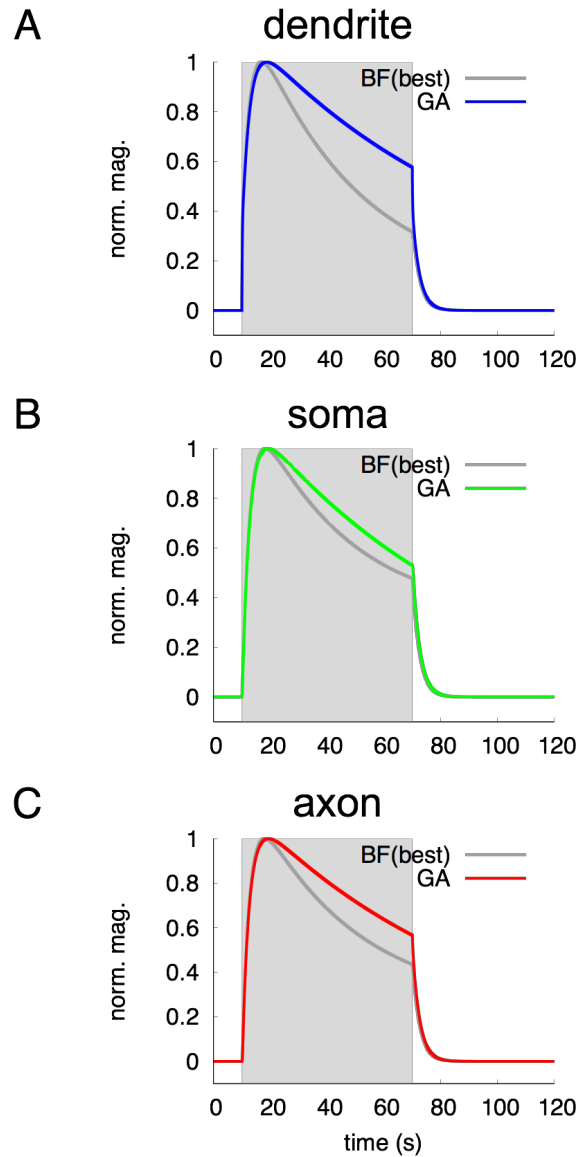Figure 5: **Experimental flow for modeling of ASER activity.**

Figure 6: **Simulated neuronal activities by two parameter search methods.** A 60-second input stimulus was applied to the dendrite. Gray shading denotes the period of input stimulus. Colored lines represent responses estimated by the Genetic Algorithm (GA) method; dark-gray lines represent Brute-Force (BF) method. Magnification is normalized from 0 (baseline) to 1 (peak value).
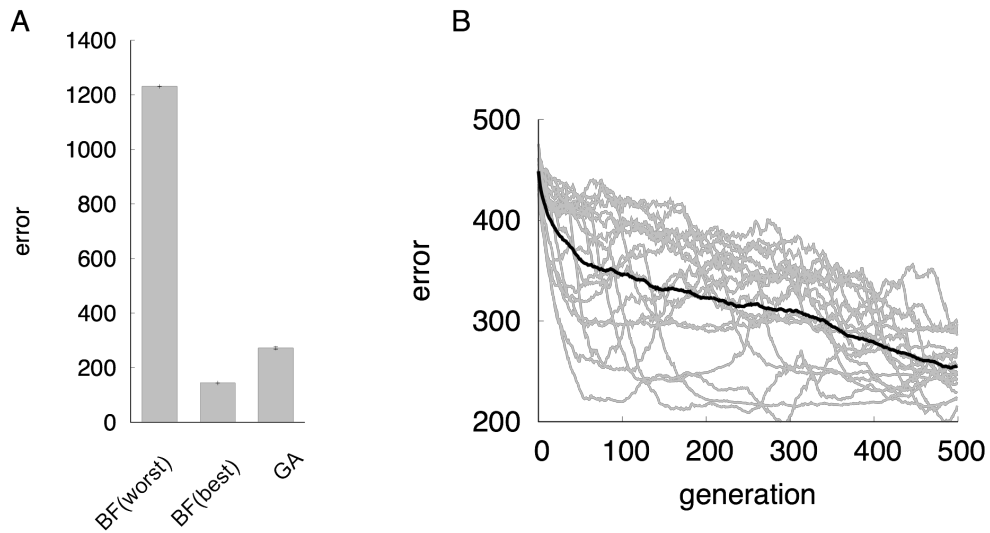
Figure 7: **Optimization of free parameters by GA and BF.** (A) Average fitness from each parameter search, BF or GA. Fitness (error) is a summation of the differences between actual neuronal responses and simulation responses. Small values of fitness indicate that a model reproduces neuronal activity close to the actual response. The best 100 and worst 100 fitness values were calculated in the BF search. In GA search, combinations of free parameters evolved over 500 generations. (B) Evolution process of fitness in GA search. The black line indicates average fitness, and gray lines indicate the individual fitness of eighteen runs.
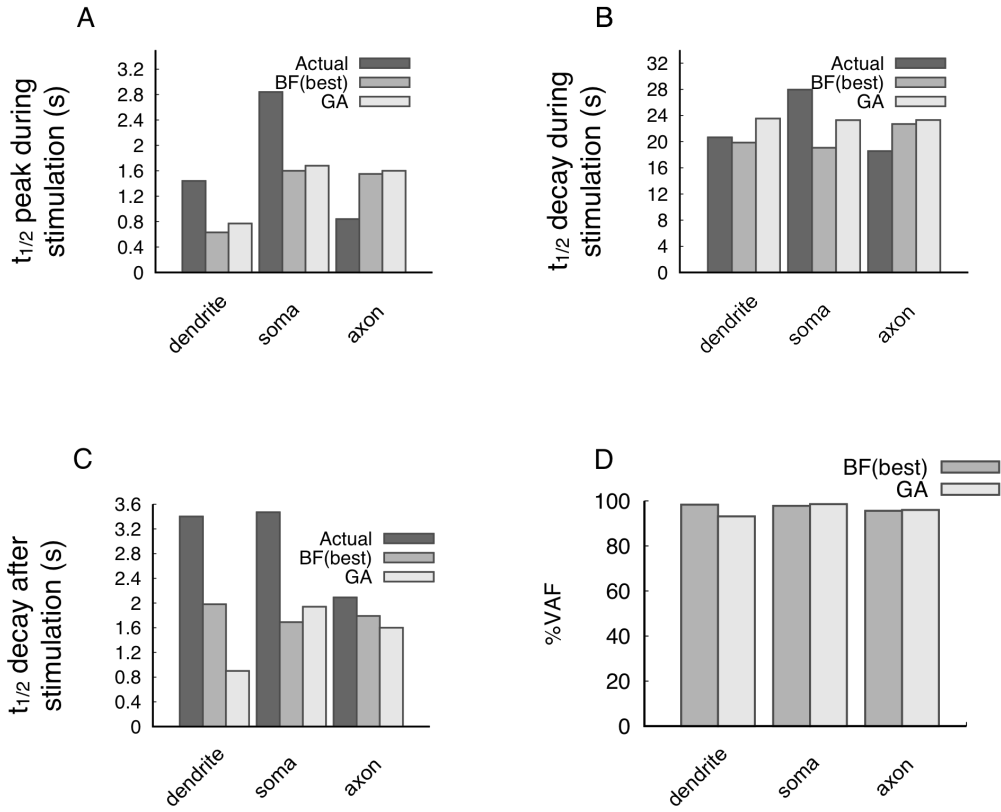
Figure 8: **Characteristics of the spatio-temporal response in the ASER chemosensory neuron to input stimulation.** (A) Comparison of the $t_{1/2}$ to the peak responses in the dendrite, soma and axon to the input stimulus. Actual means the imaging data. (B) Decay times from peak response to the end of input stimulus. (C) Decay times to baseline after removal of input stimulus. (D) Evaluation of simulated responses by variance accounted for (VAF).
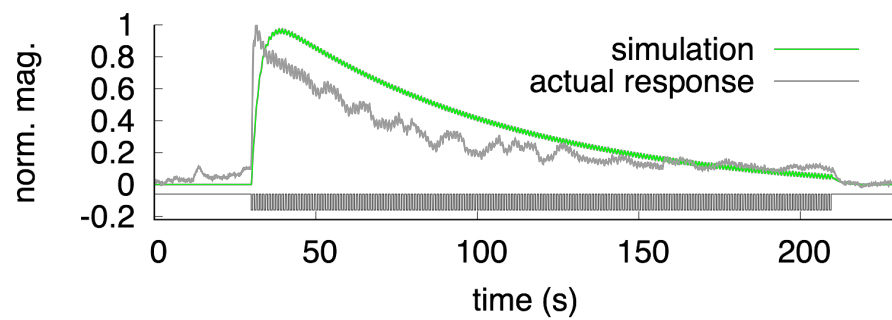
Figure 9: **Actual and simulated responses in the ASER neuron to a fast-flickering stimulus.** Gray line indicates the actual neuronal response in the soma to a flickering change of 50 mM/0 mM NaCl concentration. The green line shows the simulation of neuronal responses in the soma to a flickering input stimuli. The sequence stimulus input is shown in black.
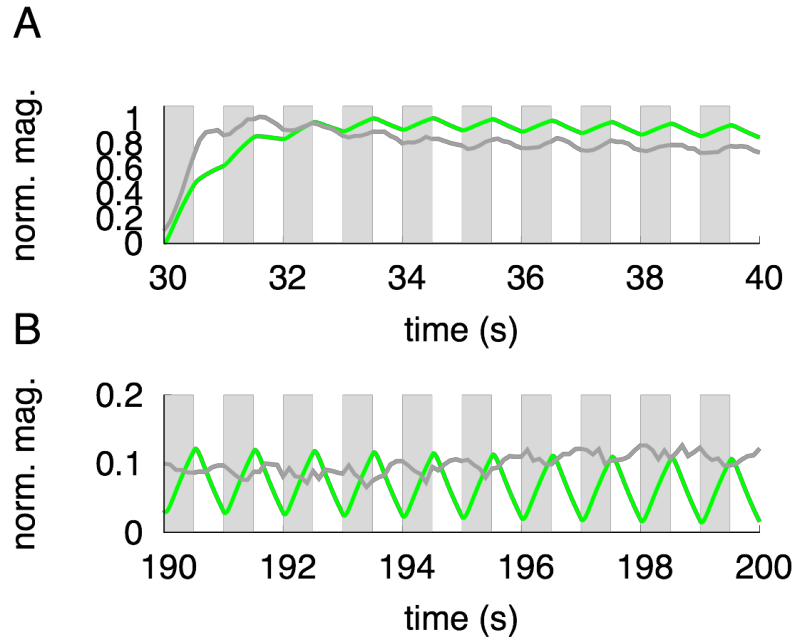
Figure 10: **Actual and simulated responses in the ASER neuron to a fast-flickering stimulus (magnified view).** (A) The graph shows the magnified view around the 30-40 sec interval. Gray shading represents downsteps of NaCl concentration for actual imaging (green) or simulation (dark-gray). (B) The graph shows the magnified view around the 190-200 sec interval. Gray shading represents downsteps of NaCl concentration for actual imaging (green) or simulation (dark-gray).

Figure 11: **Temporal responses of the dendrite to flickering stimuli with 0.5 s pulse.** The actual response (gray) and simulated responses (blue) of the dendrite are shown. The sequence stimulus input is shown in black.

Figure 12: **Temporal responses of the axon to flickering stimuli with 0.5 s pulse.** The actual response (gray) and simulated response (red) of the axon are shown. The sequence stimulus input is shown in black.

Figure 13: **Evaluation of simulation by the percentage of VAF.** VAF index were calculated from simulated responses to flickering stimuli with 0.5 s pulse.
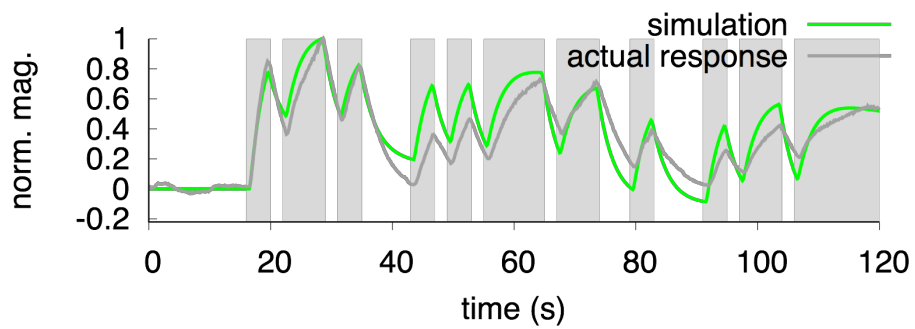
Figure 14: **Somatic responses to a pseudorandom stimulus.** Dark-gray line indicates the actual responses in the soma to pseudorandom changes of 50 mM/0 mM NaCl concentration. The green line indicates the result of simulation in the soma to a pseudorandom input stimulus. Gray shading represents downsteps of NaCl concentration for actual imaging (dark-gray) or simulation (green).
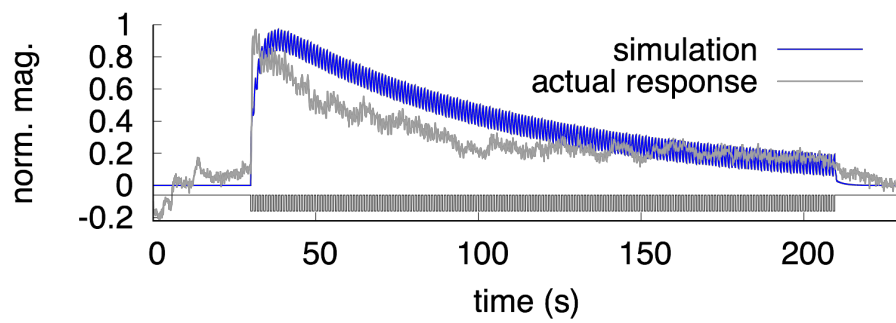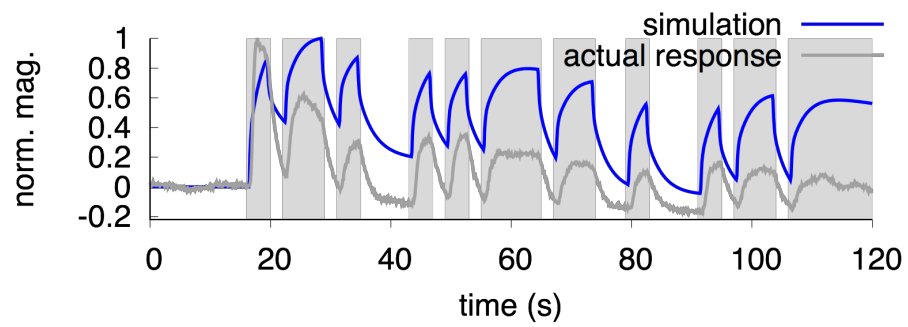
Figure 15: **Temporal responses of the dendrite to pseudorandom stimuli.** The actual response (dark-gray) and simulated responses (blue) of the dendrite are shown. Gray shading represents downsteps of NaCl concentration for actual imaging (dark-gray) or simulation (blue).
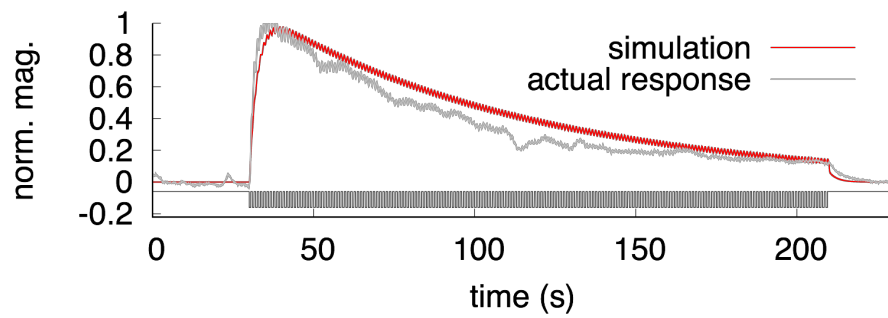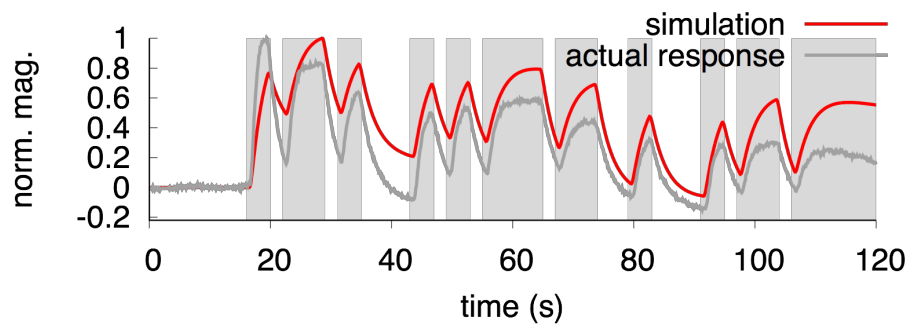
Figure 16: **Temporal responses of the axon to pseudorandom stimuli.** The actual response (dark-gray) and simulated response (red) of the axon are shown. Gray shading represents downsteps of NaCl concentration for actual imaging (dark-gray) or simulation (red).
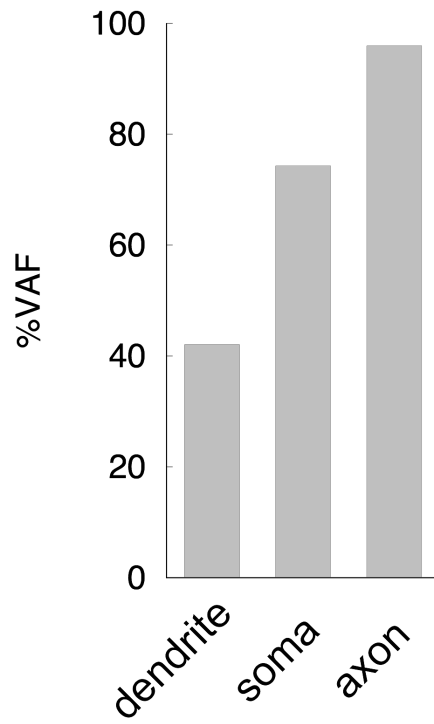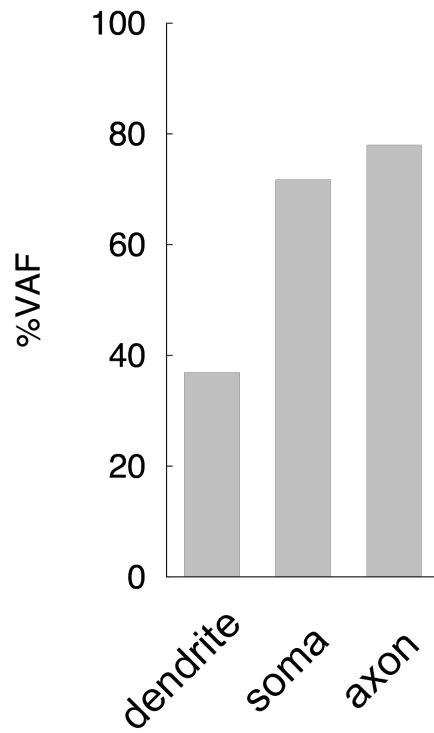
Figure 17: **Evaluation of simulation by the percentage of VAF.** VAF index were calculated from simulated responses to pseudorandom input stimulus.

Figure 18: **Average calcium dynamics in neuronal response (soma) to concentration steps of various sizes from baseline (50 mM NaCl)** The $\Delta F/F_0$ value is indicated to compare the neuronal activity to the NaCl concentration changes. $n = 20$ ($n = 10$ in 50 mM change) (top). The simulated responses in the soma activity with the proposed model to input stimuli of various magnitudes (bottom).

Figure 19: **Evaluation of simulation performance for somatic response.** VAF index were calculated from simulated responses to input stimuli of various magnitudes. 'img. (mM change)' means the size of NaCl downstep in mM, and 'sim' indicates the input stimulus in simulation.

Figure 20: **The relationship between NaCl stimulation and peak responses in soma.** (A) The relationship between the size of NaCl downstep and triggered actual peak response in the soma. Error bars represent SEM. n = 20 (n = 10 in 50 mM change). (B) The relationship between the input stimulus ($I(t)$) and simulated peak response in the soma. (C) The simulated peak response in the soma are plotted after application of sigmoidal transfer function.
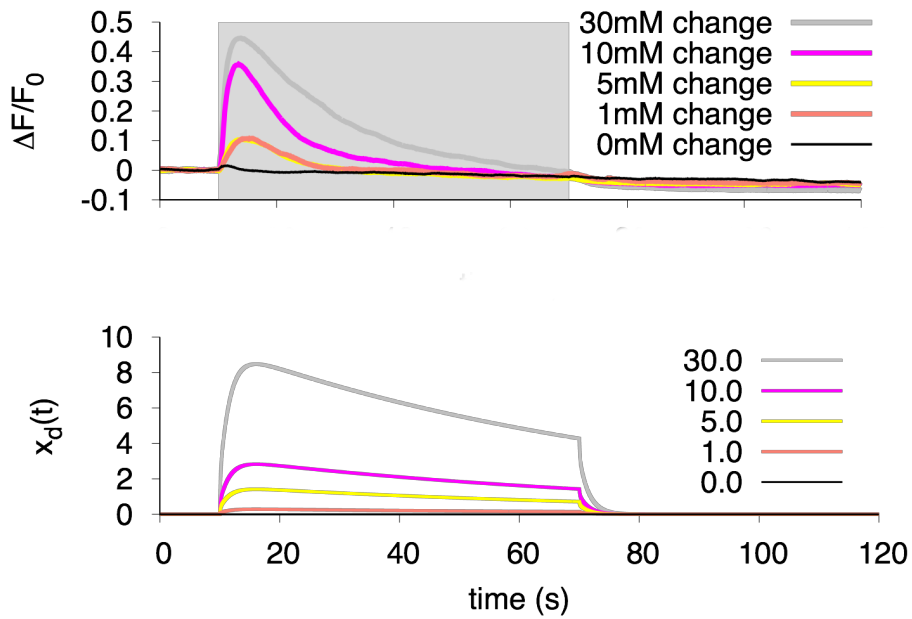
Figure 21: **Average calcium dynamics in neuronal response (dendrite) to concentration steps of various sizes from baseline (50 mM NaCl).** The $\Delta F/F_0$ value is indicated to compare the neuronal activity to the NaCl concentration changes (top). n = 20 (n = 10 in 50 mM change). The simulated responses in the dendrite activity with the proposed model to input stimuli of various magnitudes (bottom).
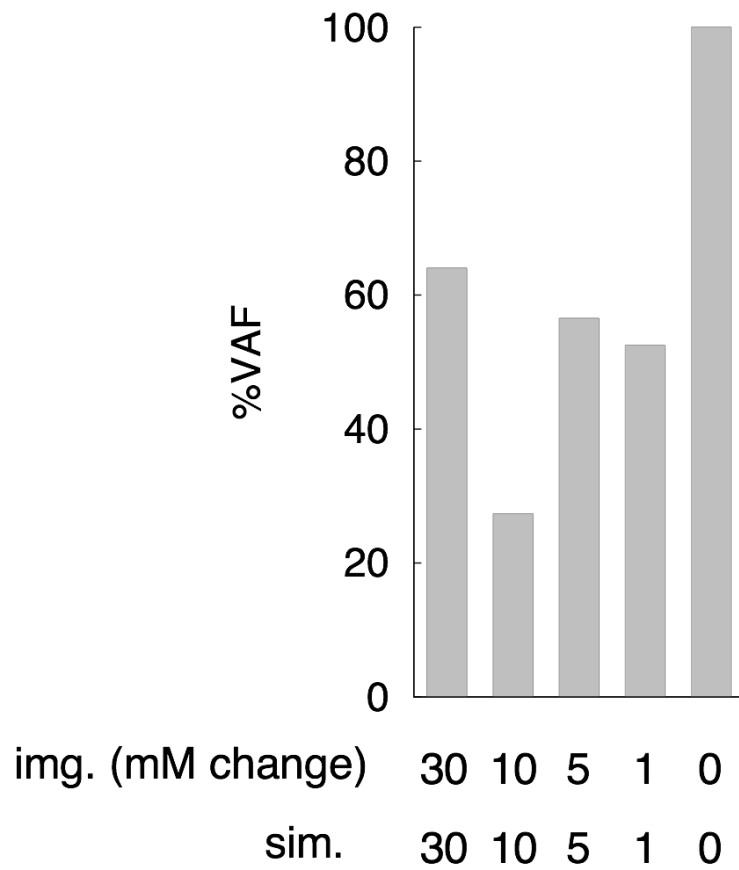
Figure 22: **Evaluation of simulation performance for dendritic response.** VAF index were calculated from simulated responses to input stimuli of various magnitudes. 'img. (mM change)' means the size of NaCl downstep in mM, and 'sim' indicates the input stimulus in simulation.
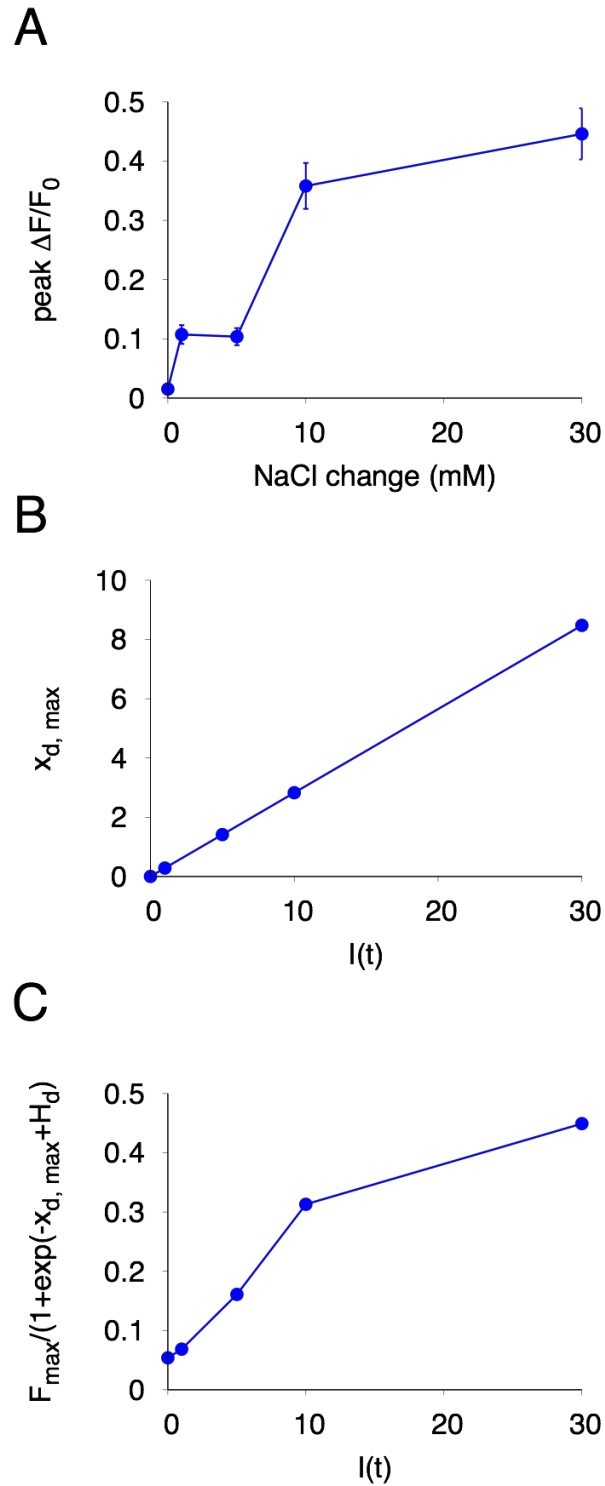
Figure 23: **The relationship between NaCl stimulation and peak responses in dendrite.** (A) The relationship between the size of NaCl downstep and triggered actual peak response in the dendrite. Error bars represent SEM. n = 20 (n = 10 in 50 mM change). (B) The relationship between the input stimulus ($I(t)$) and simulated peak response in the dendrite. (C) The simulated peak response in the dendrite are blotted after application of sigmoidal transfer function.
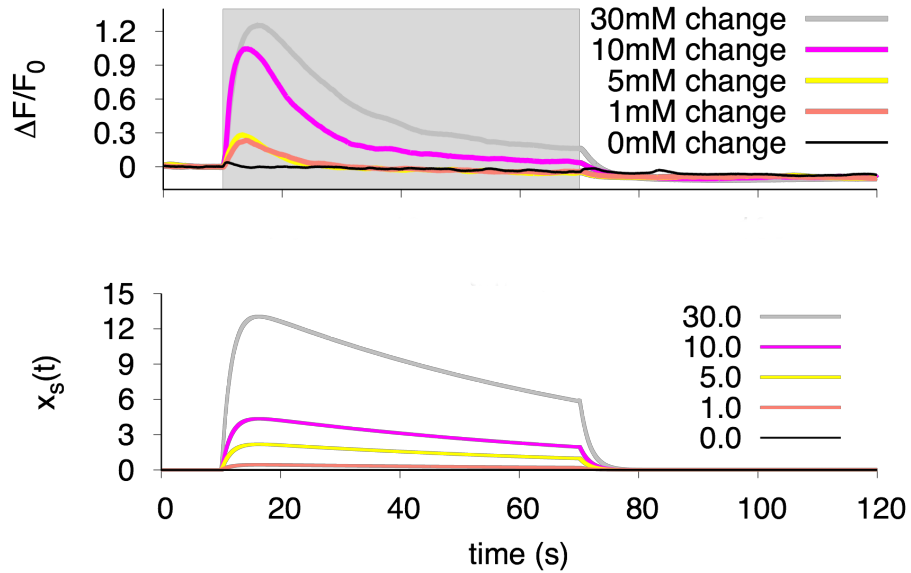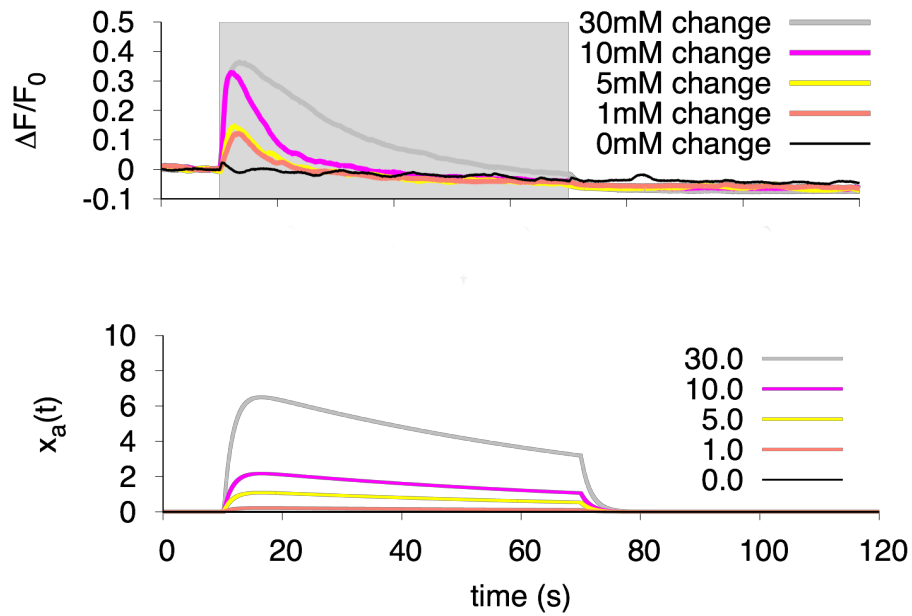
Figure 24: **Average calcium dynamics in neuronal response (axon) to concentration steps of various sizes from baseline (50 mM NaCl).** The $\Delta F/F_0$ value is indicated to compare the neuronal activity to the NaCl concentration changes (top). n = 20 (n = 10 in 50 mM). The simulated responses in the axon activity with the proposed model to input stimuli of various magnitudes (bottom).
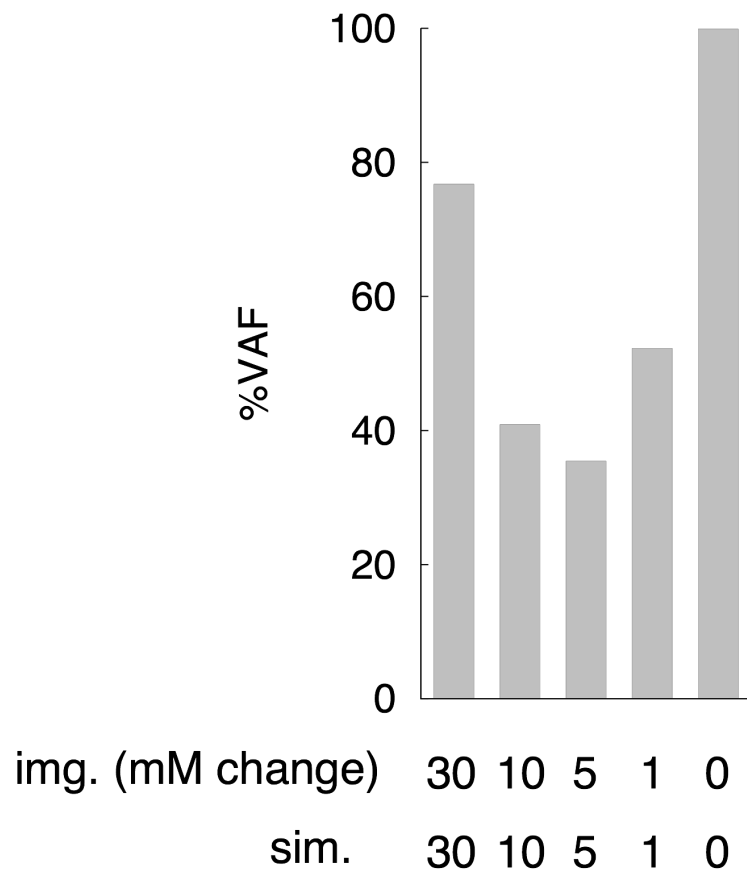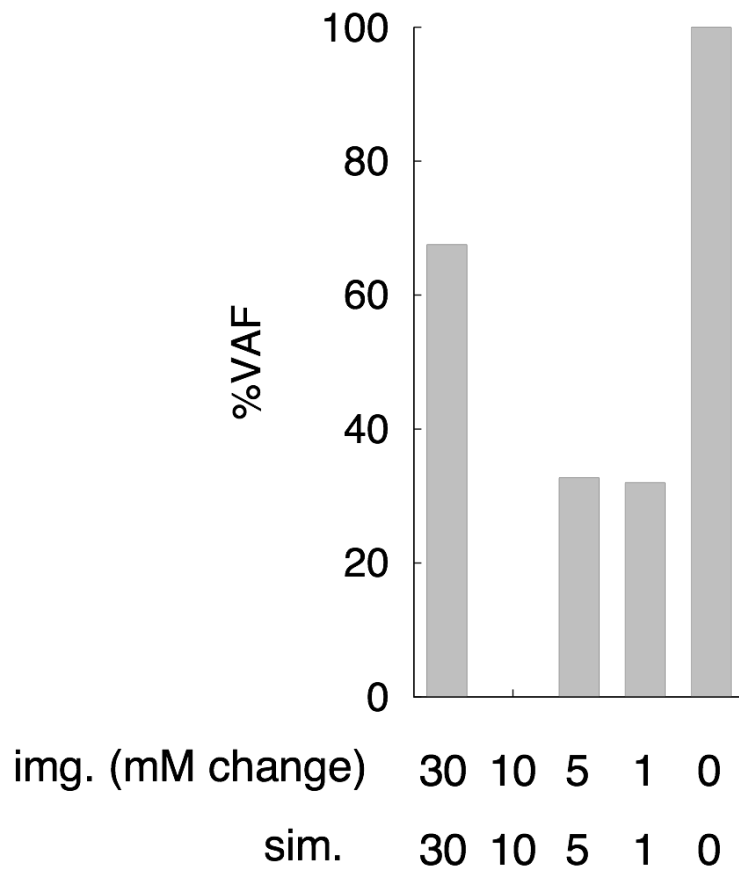
Figure 25: **Evaluation of simulation performance for axonal response.** VAF index were calculated from simulated responses to input stimuli of various magnitudes. 'img. (mM change)' means the size of NaCl downstep in mM, and 'sim' indicates the input stimulus in simulation.
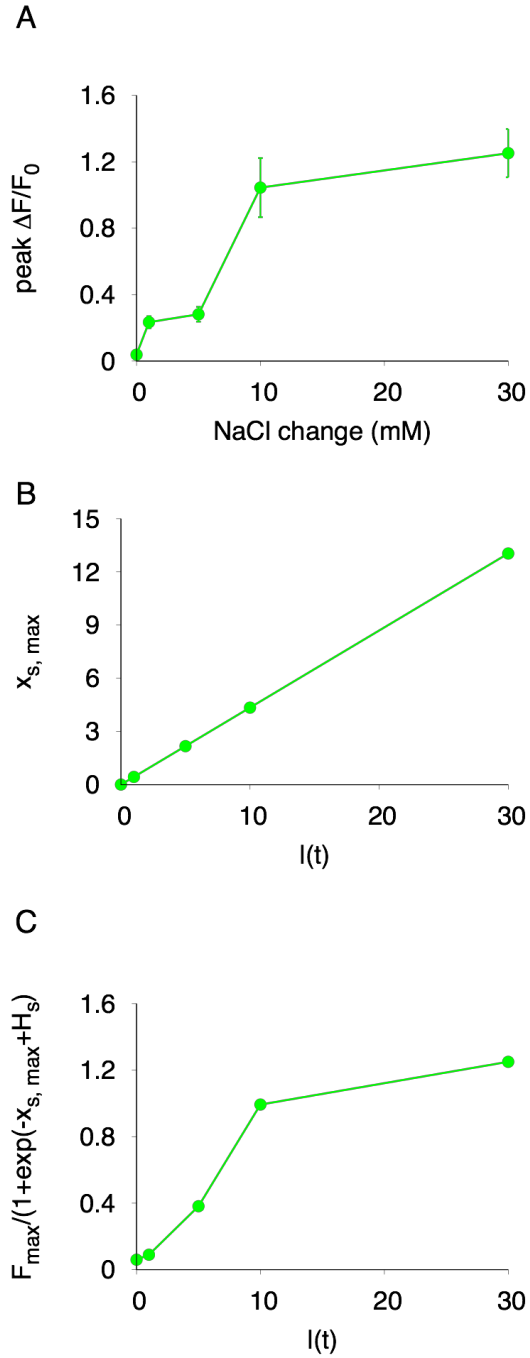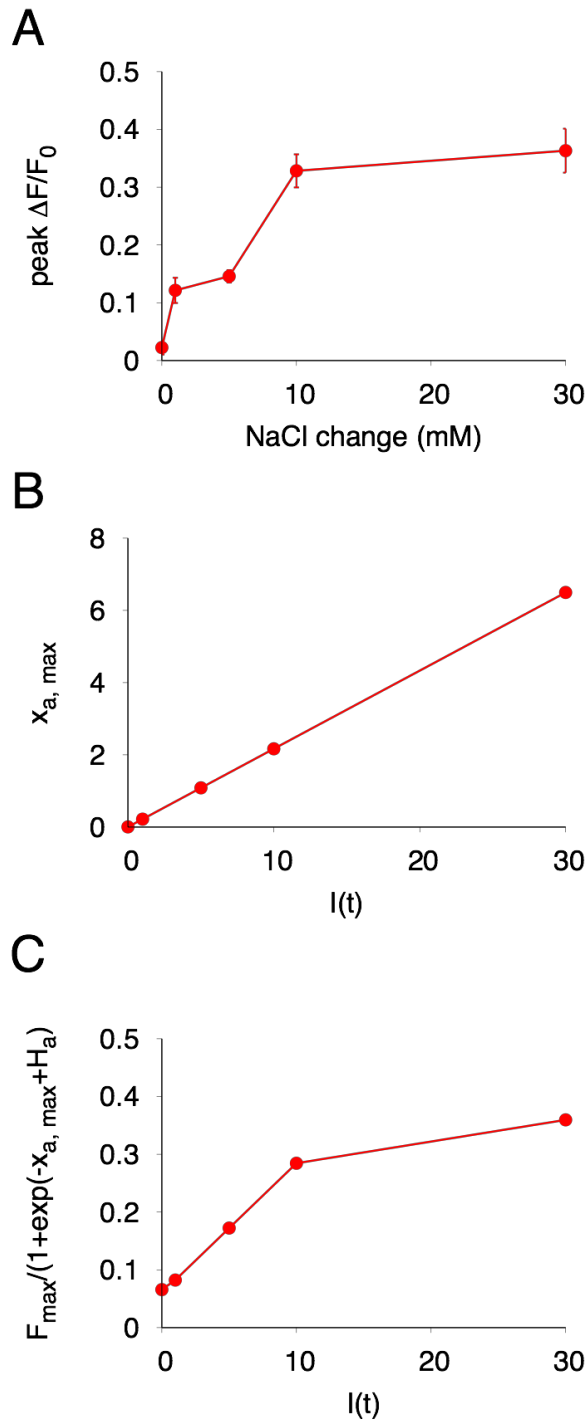
Figure 26: **The relationship between NaCl stimulation and peak responses in axon.** (A) The relationship between the size of NaCl downstep and triggered actual peak response in the axon. Error bars represent SEM. $n = 20$ ($n = 10$ in 50 mM change). (B) The relationship between the input stimulus ($I(t)$) and simulated peak response in the axon. (C) The simulated peak response in the soma are plotted after application of sigmoidal transfer function.

Bibliography

[1] Markram, H., Muller, E., Ramaswamy, S., Reimann, M. W., Abdellah, M., Sanchez, C. A., Ailamaki, A., Alonso-Nanclares, L., Antille, N., Arsever, S., Kahou, G. A. A., Berger, T. K., Bilgili, A., Buncic, N., Chalimourda, A., Chindemi, G., Courcol, J.-D., Delalondre, F., Delattre, V., Druckmann, S., Dumusc, R., Dynes, J., Eilemann, S., Gal, E., Gevaert, M. E., Ghobril, J.-P., Gidon, A., Graham, J. W., Gupta, A., Haenel, V., Hay, E., Heinis, T., Hernando, J. B., Hines, M., Kanari, L., Keller, D., Kenyon, J., Khazen, G., Kim, Y., King, J. G., Kisvarday, Z., Kumbhar, P., Lasserre, S., Le Bé, J.-V., Magalhães, B. R. C., Merchán-Pérez, A., Meystre, J., Morrice, B. R., Muller, J., Muñoz-Céspedes, A., Muralidhar, S., Muthurasa, K., Nachbaur, D., Newton, T. H., Nolte, M., Ovcharenko, A., Palacios, J., Pastor, L., Perin, R., Ranjan, R., Riachi, I., Rodríguez, J.-R., Riquelme, J. L., Rössert, C., Sfyrakis, K., Shi, Y., Shillcock, J. C., Silberberg, G., Silva, R., Tauheed, F., Telefont, M., Toledo-Rodriguez, M., Tränkler, T., Van Geit, W., Díaz, J. V., Walker, R., Wang, Y., Zaninetta, S. M., DeFelipe, J., Hill, S. L., Segev, I., and Schürmann, F. (2015) Reconstruction and simulation of neocortical microcircuitry. *Cell,* **163**(2), 456–492.

[2] Muto, A., Ohkura, M., Abe, G., Nakai, J., and Kawakami, K. (2013) Real-time visualization of neuronal activity during perception. *Current Biology,* **23**(4), 307–311.

[3] Keene, A. C. and Waddell, S. (2007) *Drosophila* olfactory memory: Single genes to complex neural circuits. *Nature Reviews Neuroscience,* **8**(5), 341–354.

[4] Barker, A. J. and Baier, H. (2015) Sensorimotor decision making in the zebrafish tectum. *Current Biology,* **25**(21), 2804–2814.

[5] White, J. G., Southgate, E., Thomson, J. N., and Brenner, S. (1986) The structure of the nervous system of the nematode *Caenorhabditis elegans. Philosophical Transactions of the Royal Society of London B: Biological Sciences,* **314**(1165), 1–340.

[6] Chen, B. L., Hall, D. H., and Chklovskii, D. B. (2006) Wiring optimization can relate neuronal structure and function. *Proceedings of the National Academy of Sciences of the United States of America,* **103**(12), 4723–4728.

[7] Prevedel, R., Yoon, Y.-G., Hoffmann, M., Pak, N., Wetzstein, G., Kato, S., Schrodel, T., Raskar, R., Zimmer, M., Boyden, E. S., and Vaziri, A. (2014) Simultaneous whole-animal 3D imaging of neuronal activity using light-field microscopy. *Nature Methods,* **11**(7), 727–730.

[8] Nguyen, J. P., Shipley, F. B., Linder, A. N., Plummer, G. S., Liu, M., Setru, S. U., Shaevitz, J. W., and Leifer, A. M. (2016) Whole-brain calcium imaging with cellular resolution in freely behaving *Caenorhabditis elegans. Proceedings*

of the National Academy of Sciences of the United States of America, **113**(8), E1074–E1081.

[9] Venkatachalam, V., Ji, N., Wang, X., Clark, C., Mitchell, J. K., Klein, M., Tabone, C. J., Florman, J., Ji, H., Greenwood, J., Chisholm, A. D., Srinivasan, J., Alkema, M., Zhen, M., and Samuel, A. D. T. (2016) Pan-neuronal imaging in roaming *Caenorhabditis elegans. Proceedings of the National Academy of Sciences of the United States of America,* **113**(8), E1082–E1088.

[10] Kato, S., Kaplan, H. S., Schrödel, T., Skora, S., Lindsay, T. H., Yemini, E., Lockery, S., and Zimmer, M. (2015) Global brain dynamics embed the motor command sequence of *Caenorhabditis elegans. Cell,* **163**(3), 656–669.

[11] Kato, S., Xu, Y., Cho, C. E., Abbott, L. F., and Bargmann, C. I. (2014) Temporal responses of *C. elegans* chemosensory neurons are preserved in behavioral dynamics. *Neuron,* **81**(3), 616–628.

[12] Izhikevich, E. M. (2003) Simple model of spiking neurons. *IEEE Transactions on Neural Networks,* **14**(6), 1569–1572.

[13] Izhikevich, E. M. and Edelman, G. M. (2008) Large-scale model of mammalian thalamocortical systems. *Proceedings of the National Academy of Sciences of the United States of America,* **105**(9), 3593–3598.

[14] Mellem, J. E., Brockie, P. J., Madsen, D. M., and Maricq, A. V. (2008) Action potentials contribute to neuronal signaling in *C. elegans. Nature Neuroscience,* **11**(8), 865–867.

[15] Goodman, M. B., Hall, D. H., Avery, L., and Lockery, S. R. (1998) Active currents regulate sensitivity and dynamic range in *C. elegans* neurons. *Neuron,* **20**(4), 763–772.

[16] Nickell, W. T., Pun, R. Y. K., Bargmann, C. I., and Kleene, S. J. (2002) Single ionic channels of two *Caenorhabditis elegans* chemosensory neurons in native membrane. *The Journal of Membrane Biology,* **189**(1), 55–66.

[17] Ferrée, T. C. and Lockery, S. R. (1999) Computational rules for chemotaxis in the nematode *C. elegans. Journal of Computational Neuroscience,* **6**(3), 263–277.

[18] Wicks, S. R., Roehrig, C. J., and Rankin, C. H. (1996) A dynamic network simulation of the nematode tap withdrawal circuit: predictions concerning synaptic function using behavioral criteria. *Journal of Neuroscience,* **16**(12), 4017–4031.

[19] Sakata, K. and Shingai, R. (2004) Neural network model to generate head swing in locomotion of *Caenorhabditis elegans. Network: Computation in Neural Systems,* **15**(3), 199–216.

[20] Rakowski, F., Srinivasan, J., Sternberg, P., and Karbowski, J. (2013) Synaptic polarity of the interneuron circuit controlling *C. elegans* locomotion. *Frontiers in Computational Neuroscience,* **7**, 128.

[21] Izquierdo, E. J. and Lockery, S. R. (2010) Evolution and analysis of minimal neural circuits for klinotaxis in *Caenorhabditis elegans. Journal of Neuroscience,* **30**(39), 12908–12917.

[22] Boyle, J. H. and Cohen, N. (2008) *Caenorhabditis elegans* body wall muscles are simple actuators. *Biosystems,* **94**(1–2), 170–181.

[23] Hendricks, M., Ha, H., Maffey, N., and Zhang, Y. (2012) Compartmentalized calcium dynamics in a *C. elegans* interneuron encode head movement. *Nature,* **487**(7405), 99–103.

[24] Chalasani, S. H., Chronis, N., Tsunozaki, M., Gray, J. M., Ramot, D., Goodman, M. B., and Bargmann, C. I. (2007) Dissecting a circuit for olfactory behaviour in *Caenorhabditis elegans. Nature,* **450**(7166), 63–70.

[25] Clark, D. A., Biron, D., Sengupta, P., and Samuel, A. D. T. (2006) The AFD sensory neurons encode multiple functions underlying thermotactic behavior in *Caenorhabditis elegans. Journal of Neuroscience,* **26**(28), 7444–7451.

[26] Rall, W. (1959) Branching dendritic trees and motoneuron membrane resistivity. *Experimental Neurology,* **1**(5), 491–527.

[27] Herz, A. V. M., Gollisch, T., Machens, C. K., and Jaeger, D. (2006) Modeling single-neuron dynamics and computations: A balance of detail and abstraction. *Science,* **314**(5796), 80–85.

[28] Kuramochi, M. and Doi, M. (2017) A computational model based on multi-regional calcium imaging represents the spatio-temporal dynamics in a *Caenorhabditis elegans* sensory neuron. *PLOS ONE,* **12**(1), e0168415.

[29] Zhao, Y., Araki, S., Wu, J., Teramoto, T., Chang, Y. F., Nakano, M., Abdelfat-tah, A. S., Fujiwara, M., Ishihara, T., Nagai, T., and Campbell, R. E. (2011)

An expanded palette of genetically encoded Ca^{2+} indicators. *Science,* **333**(6051), 1888–1891.

[30] Mello, C. C., Kramer, J. M., Stinchcomb, D., and Ambros, V. (1991) Efficient gene transfer in *C. elegans*: extrachromosomal maintenance and integration of transforming sequences.. *The EMBO Journal,* **10**(12), 3959–3970.

[31] Chronis, N., Zimmer, M., and Bargmann, C. I. (2007) Microfluidics for *in vivo* imaging of neuronal and behavioral activity in *Caenorhabditis elegans. Nature Methods,* **4**(9), 727–731.

[32] Oda, S., Tomioka, M., and Iino, Y. (2011) Neuronal plasticity regulated by the insulin-like signaling pathway underlies salt chemotaxis learning in *Caenorhabditis elegans. Journal of Neurophysiology,* **106**(1), 301–308.

[33] Matsumoto, M. and Nishimura, T. (1998) Mersenne twister: A 623-dimensionally equidistributed uniform pseudo-random number generator. *ACM Trans. Model. Comput. Simul.,* **8**(1), 3–30.

[34] Press, W. H., Teukolsky, S. A., Vetterling, W. T., and Flannery, B. P. (2007) Numerical recipes 3rd edition: The art of scientific computing, Cambridge University Press, New York, NY, USA 3 edition.

[35] Holland, J. (1973) Genetic algorithms and the optimal allocation of trials. *SIAM Journal on Computing,* **2**(2), 88–105.

[36] Tsukada, Y., Yamao, M., Naoki, H., Shimowada, T., Ohnishi, N., Kuhara, A., Ishii, S., and Mori, I. (2016) Reconstruction of spatial thermal gradient en-

94

coded in thermosensory neuron AFD in *Caenorhabditis elegans*. *Journal of Neuroscience,* **36**(9), 2571–2581.

[37] Bargmann, C. I. Chemosensation in *C. elegans.* (2006).

[38] Davis, R. and Stretton, A. (1989) Passive membrane properties of motorneurons and their role in long-distance signaling in the nematode *Ascaris. Journal of Neuroscience,* **9**(2), 403–414.

[39] Davis, R. and Stretton, A. (1989) Signaling properties of *Ascaris* motorneurons: graded active responses, graded synaptic transmission, and tonic transmitter release. *Journal of Neuroscience,* **9**(2), 415–425.

[40] Suzuki, H., Thiele, T. R., Faumont, S., Ezcurra, M., Lockery, S. R., and Schafer, W. R. (2008) Functional asymmetry in *Caenorhabditis elegans* taste neurons and its computational role in chemotaxis. *Nature,* **454**(7200), 114–117.

[41] Pierce-Shimomura, J. T., Morse, T. M., and Lockery, S. R. (1999) The fundamental role of pirouettes in *Caenorhabditis elegans* chemotaxis. *Journal of Neuroscience,* **19**(21), 9557–9569.

[42] Iino, Y. and Yoshida, K. (2009) Parallel use of two behavioral mechanisms for chemotaxis in *Caenorhabditis elegans. Journal of Neuroscience,* **29**(17), 5370–5380.

[43] Kunitomo, H., Sato, H., Iwata, R., Satoh, Y., Ohno, H., Yamada, K., and Iino, Y. (2013) Concentration memory-dependent synaptic plasticity of a taste

circuit regulates salt concentration chemotaxis in *Caenorhabditis elegans*. *Nature Communications,* **4**, 2210 EP –.

[44] Luo, L., Wen, Q., Ren, J., Hendricks, M., Gershow, M., Qin, Y., Greenwood, J., Soucy, E. R., Klein, M., Smith-Parker, H. K., Calvo, A. C., Colón-Ramos, D. A., Samuel, A. D. T., and Zhang, Y. (2014) Dynamic encoding of perception, memory, and movement in a *C. elegans* chemotaxis circuit. *Neuron,* **82**(5), 1115–1128.

[45] Satoh, Y., Sato, H., Kunitomo, H., Fei, X., Hashimoto, K., and Iino, Y. (2014) Regulation of experience-dependent bidirectional chemotaxis by a neural circuit switch in *Caenorhabditis elegans*. *Journal of Neuroscience,* **34**(47), 15631–15637.

[46] Saheki, Y. and Bargmann, C. I. (2009) Presynaptic CaV2 calcium channel traffic requires CALF-1 and the $\alpha_2\delta$ subunit UNC-36. *Nature Neuroscience,* **12**(10), 1257–1265.

[47] Eric, K., James, S., Thomas, J., Steven, S., and A.J., H. (2012) Principles of neural science, McGraw-Hill Professional, 5th ed. edition.

[48] Larsch, J., Ventimiglia, D., Bargmann, C. I., and Albrecht, D. R. (2013) High-throughput imaging of neuronal activity in *Caenorhabditis elegans*. *Proceedings of the National Academy of Sciences of the United States of America,* **110**(45), E4266–E4273.

[49] Cho, C. E., Brueggemann, C., L'Etoile, N. D., Bargmann, C. I., and Ramaswami, M. (2016) Parallel encoding of sensory history and behavioral preference during *Caenorhabditis elegans* olfactory learning. *eLife,* **5**, e14000.

[50] Lindsay, T. H., Thiele, T. R., and Lockery, S. R. (2011) Optogenetic analysis of synaptic transmission in the central nervous system of the nematode *Caenorhabditis elegans. Nature Communications,* **2**, 306 EP –.

[51] Li, Z., Liu, J., Zheng, M., and Xu, X. Z. S. (2014) Encoding of both analog- and digital-like behavioral outputs by one *C. elegans* interneuron. *Cell,* **159**(4), 751–765.

Chapter 3

Synaptic dissection of a neuronal circuit for salt-chemotaxis behavior in *C. elegans*

3.1 Abstract

Neuronal circuits are an assembly of synaptic connectivity among neurons. Analysis of both the patterns of synaptic connections in a circuit and the roles of each synapse for the circuit activity helps to understand characteristics of a neural encoding for behavioral outputs. Here I show that a pair of *C. elegans* chemosensory neurons ASEL/R have an opposite role for their postsynaptic activity even though they use the same signaling molecule. I found that the ASEL glutaminergic signal inhibits the postsynaptic AIB activity through an unidentified receptor. On the other hand, the ASER glutaminergic signal stimulates AIB activity through the AMPA-

type ionotropic glutamate receptor. Both presynaptic neurons employ the same neurotransmitter glutamate but utilize distinct postsynaptic glutamate receptors, and these distinct localization patterns on the AIB neurite contribute to the opposite regulation of activity. This unfamiliar mechanism enables one class of sensory neuron to encode both excitatory and inhibitory signals for precise behavior transition.

3.2 Introduction

Toward understanding the neural information processing based on neuronal interactions, I try to develop a computational model for the whole-brain simulation with cellular-resolution level. In the chapter II, I succeeded to develop a single-cell model with the spatio-temporal activity. However the proposed neuronal model has a restriction for circuit analysis, because cannot handle the synaptic transmission. As a next step, to expand this single-cell computation into a circuit level, I characterize synaptic transmission among neurons as an element for neural encoding using calcium imaging.

Neuronal circuits are an assembly of synaptic connectivity among neurons. Compared to mammalian brains consisted of billions of neurons, lower organisms such as worm, fly, and zebrafish have a much compact nervous system [1, 2, 3]. They thus are widely used as models to study for characterization of neural encoding by *in vivo* neuronal recording [2, 4, 5]. In addition to the *in vivo* imaging analysis, analysis of both the patterns of synaptic connections in a circuit and the roles of each synapse in network activity also helps to understand characteristics of a neural encoding for

behavioral outputs. Despite of compact nervous systems in those model animals, they are capable of performing diverse behavioral outputs, and many of those are analogous to those observed in mammals [6, 7, 8]. This means that there should be the general rule in neural network for simple synaptic information flow, which may navigate circuit computations for multiple behavioral outputs in these organisms, similar to higher organisms. However, how dynamical encoding through synapses between neurons navigate multiple behavioral outputs has not been well understood yet.

C. elegans has a possibility to characterize a circuit dynamics not only in network structure level but also in synaptic functional level. The patterns of synaptic connectivity in the *C. elegans* nervous system has been identified [1]. In addition, a real-time calcium imaging from single cellular resolution to the whole-brain level can be applicable to living animals [4, 9]. *C. elegans* has a small nervous system with only 302 neurons. Due to this simplicity, worm is widely used to understand the mechanisms of neural encoding for behavioral outputs. In particular, the mechanism of salt-chemotaxis behavior has been observed for decades, and its molecular and cellular knowledge are accumulated [10, 11, 12, 13, 14, 15, 16, 17, 18, 19, 20]. For the salt sensing, a pair of sensory neurons named ASEL and ASER are mainly functioning neurons. These two neurons are located at left/right side of *C. elegans* head region and their morphology and synapse localization pattern seems to be bi-symmetrically similar. However, these neurons have an opposite response to salt (NaCl). ASEL is activated by the increase of NaCl concentration (NaCl upstep), whereas ASER is activated by the decrease of NaCl concentration (NaCl downstep). In addition to the different response to NaCl, those neurons seem to have distinct functions for behavior:

ASEL promotes forward run probability, whereas ASER promotes turn probability in chemotaxis behavior [13, 14]. The synaptic connectivity patterns are also similar. Both neurons connect to same interneurons such as AIA, AIB and AIY [1], although both neurons are glutaminergic neurons releasing glutamate as a transmitter [21]. ASEL/R neurons are likely to regulate opposite behavioral outputs by using unknown neuronal signaling mechanism. These facts provoke an intriguing question. What is the synaptic mechanism leading to opposite behavioral outputs by ASE neurons?

To answer this question, I applied both calcium imaging and molecular genetics to the *C. elegans* salt-sensing neural circuit. By characterizing the response of AIB interneurons that are connected and regulated by ASE neurons, I examined cellular and molecular features of synaptic regulation between ASE and AIB. I also examined how synapses between these two neurons are organized based on their functions. From these analyses, I found a novel aspect of relationship between spatial distribution of synapse connectivity and postsynaptic responses in a neuronal circuit. I believe that this information flow provides one topological network at a circuit level.

3.3 Materials and methods

3.3.1 Strains

Worms were cultivated on standard NGM agar plates seeded with *E. coli* strain OP50 at room temperature ($\sim$ 22 °C). Wild-type strain (Bristle N2) and other mutant

strains used in this study are shown in Table 5.

3.3.2   Molecular biology and transgenic animals

Standard methods for molecular biology were used for plasmid DNA construction. For the calcium indicator protein G-GECO1.2 [22] expression, the G-GECO1.2 coding sequence was inserted between the AgeI and EcoRI site of the pPD95.79 vector (kind gift from Andy Fire). Then, each promoter region was inserted between the SphI and XmaI site of resulting pPD95.79/G-GECO1.2 plasmid. I used following promoter regions for cell-specific expression; *gcy-5* for ASER, *gcy-7* for ASEL, and *npr-9* for AIB. To generate plasmid DNAs for UNC-13 expression, the full-length *unc-13* cDNA fragment was amplified by overlapping PCR fusion using the following primers:

5 ' CCGGGATGCCACGCCGACGGAAACGAAA3'

5 ' GTGTCCTTCGTTTGGTCTTTCCAACTTGAG3 '

5 ' CTCAAGTTGGAAAGACCAAACGAAGGACAC3 '

5 ' CAGGCGTCTTGCATCGTTTCTTTTG3 '

5 ' CAAAAGAAACGATGCAAGACGCCTG3 '

5 ' GCATTCGGCAGTTGTTTCAATAGAGCC3 '

5 ' GGCTCTATTGAAACAACTGCCGAATGC3 ' .

The resulting full-length *unc-13* fragment was inserted between the XmaI and KpnI site of the pPD95.79 Vector. Then, each promoter region for ASEL and ASER was inserted between the SphI and XmaI site of the pPD95.79/UNC-13 plasmid DNA. To generate *Pgcy-5::TeTx::mCherry*, *TeTx::mCherry* fragment from *Pttx-3::TeTx::mCherry*

(kind gift from Sreekanth Chalasani) was inserted between the SmaI and ApaI site of the pDK155[*Pgcy-5::GCaMP6*] plasmid DNA. For the glutamate-gated chloride channels expressions, *glc-3* cDNA fragment was amplified by PCR fusion using the following primers:

5'ATGCGGATCCATGAGTCTCCGTTCACTTCTCAAT3' and

5'TTCTACCGGTACCTTGGCTTCCGGTGCGTGATATTGT3'.

 The resulting full-length *glc-3* fragment was inserted between the BamHI and KpnI site of the pPD95.79/Venus Vector. Then, *npr-9* promoter region was inserted between the SphI and BamHI site of the pPD95.79/GLC-3 plasmid DNA. For the AMPA-type ionotropic glutamate receptor expressions, *glr-1::GFP* fragment, which is digested by KpnI and EcoRV from *Pttx-3::glr-1::GFP* (kind gift from Takaaki Hirotsu), was inserted into a pDK597[*Pgcy-7::R-GECO1*] plasmid DNA. Then, *UNC54 3UTR* and *npr-9* promoter region were inserted between the EcoRV/ApaI and the KpnI/ApaI. To observe the localization of the presynaptic vesicle associated protein (RAB-3), *mCherry::rab-3* fragment, which was digested by the SmaI and ApaI from pDK601[*Pacr-5::mCherry::rab-3*], was inserted between the SmaI and ApaI site of the pDK104[*Pgcy-5::snb-1::GFP*] plasmid DNA.

For generation of transgenic animals, the resulting plasmid DNAs were injected into N2 (Bristol) or mutant animals using a standard microinjection method [23]. Details for the transgenic worms are shown in Table 5.

3.3.3 Calcium imaging

One or two day old adult transgenic worms were used for imaging. Worms were immobilized in a microfluidic device fabricated from polydimethylsiloxane (PDMS) [24]. The microfluidic device was set on an inverted fluorescent microscope (Olympus IX71), and time-lapse images were performed using an ORCA-Flash 4.0 CCD camera (Hamamatsu Photonics) controlled by HCImage software (Hamamatsu Photonics). Recordings were started within 3 minutes after removal from food, and images were captured at the rate of 10 frames/sec. The following compositions of buffers for calcium imaging were used: (in mM) 5 KPO_4 (pH 6.0), 1 $CaCl_2$, 1 $MgSO_4$, and 0, 50 mM NaCl for the stimulation. All the buffers were adjusted to be 350 mOsmol/L H_2O with glycerol [16]. The patterns of salt stimulation were automated by using the Perfusion Valve Controller System VC-6M (Warner Instruments) and Arduino microcontroller to control solenoid valves (Arduino SRL) with a pre-generated sequence. I used $\Delta F/F_0$ for values of fluorescence intensity change. F_0 was defined as the average fluorescence in a 5 s window before stimulation. After background subtraction, the total fluorescence intensity was measured from individual regions of interest (ROIs) in the each neuron.

Each animal was imaged twice, with a 30 s interval between the first and second observation. AIB has a bistable activity state: active and resting state [25]. Mostly, the second imaging data were used for data analysis, because AIB activity from the second observation was more stable than that from the first observation.

3.3.4 Confocal microscopy observation

L4 larvae were mounted on a 2% agarose pad with 50 mM sodium azide in M9 solution for anesthesia. Images were acquired on an inverted confocal microscope (Nikon A1, Nikon) with 60x objective lens, and were handled by NIS-Elements C/NIS-Elements C-ER and ImageJ software.

3.3.5 Statistical methods

The each data did not shown gaussian distribution based on the Shaprio-Wilk test. So, a non-parametric Wilcoxon rank sum test was performed for the evaluation of median differences of calcium responses between wild-type and *che-1(p679)* mutants (Fig 30). A non-parametric multiple comparison Steel-Dwass test was used for the evaluation of averaged calcium responses in *unc-13(e312)*, the ASEL- or ASER-specific UNC-13 rescuing animals in *unc-13(e312)* background (Fig 32).

3.4 Results

3.4.1 Calcium responses in ASEL, ASER, and AIB to the NaCl concentration changes

The nematode *C. elegans* can detect the gradient of NaCl concentration, and moves to a preferential condition by using several behavioral strategies [12, 15]. The pair of amphid sensory-neurons ASELeft and ASERight at head position mainly detects NaCl concentration changes [10]. Both ASEL/R have synaptic connections to the

downstream first-layer interneurons AIB (Fig 27). I wondered how the ASE neurons control AIB activities when NaCl concentration was changed. To monitor the calcium responses of these neurons in the wild-type animals, I recorded fluorescent changes of the genetically-encoded calcium indicator G-GECO1.2 [22], which is specifically expressed in these neurons. For the observation of ASEL response, I applied the upstep NaCl concentration change (from 0 mM to 50 mM NaCl) and found that the ASEL calcium response began to rise just after the upstep of NaCl concentration, and the $\Delta F/F_0$ value reached its peak level in a few seconds (Data not shown). After reaching to the peak response, its calcium response gradually decayed toward the steady state level. On the other hand, the ASER calcium response rose slowly after the downstep of NaCl concentration was applied (from 50 mM to 0 mM NaCl), and $\Delta F/F_0$ value reached its peak level in a few seconds (Fig 28). After reaching to the peak response, the ASER calcium response gradually decayed during the 0 mM downstep in NaCl concentration. This decay process during the downstep to 0 mM NaCl lasted until the NaCl concentration was restored to 50 mM (Fig 28). Next, I examined the response of postsynaptic interneurons AIB and found that AIB showed similar response pattern with ASER: their responses rose slowly after the downstep of NaCl concentration (Fig 28), and were sustained at around the peak level during the 0 mM NaCl concentration. After the upstep of NaCl concentration, AIB calcium level immediately decayed to the steady state level. Consistent with previous studies, ASEL has a transient NaCl-upstep response, and ASER and AIB show a sustained NaCl-downstep response [13, 17].

107

3.4.2 ASE neurons regulate AIB activity based on NaCl concentration change

The AIB interneurons receive synaptic inputs from many sensory neurons. Several sensory neurons including AFD, ASE, ASH, ASJ, AWB, and AWC, are suspected to function as salt-sensing neurons [14, 26], and all these sensory neurons are reported to have synaptic connections with AIB neurons [1]. To examine which sensory neurons do mainly affect the AIB activity based on NaCl concentration changes, I recorded the AIB response in *che-1(p679)* mutant animals. The *che-1(p679)* mutant has no ASE neurons [27, 28], and did not show any significant AIB calcium response compared to clear AIB response observed in the wild type animals (Fig 29, 30). This result indicates that AIB neurons cannot respond to the changes of NaCl concentration without ASE neurons. Therefore, I conclude that other sensory neurons except for ASE neurons probably have small or no effect on AIB activity, but ASE neurons strongly affect to AIB activity to the changes of NaCl concentration.

3.4.3 ASEL inhibits AIB activity whereas ASER stimulates AIB activity

Next, I examined how two distinct ASEL and ASER signaling are cooperatively involved in the regulation of AIB activity, because those neurons show opposite response patterns to the NaCl concentration change. I firstly monitored AIB responses to the change of NaCl concentration in the synaptic vesicle release-defective mutant *unc-13(e312)* [29]. *unc-13* encodes a protein required for the vesicle priming step at the

presynaptic site and mutations in its gene causes severe defects in neurotransmitter release. The AIB in *unc-13(e312)* mutants did not show any responses to both the downstep and upstep change of NaCl concentration (Fig 31). Therefore, together with the *che-1* mutant results, these results suggest that the synaptic transmission from ASE neurons is required for the regulation of AIB activity when NaCl concentration was changed.

I further examined the role of each ASEL and ASER neuron for the AIB activity. For this purpose, UNC-13 protein was specifically expressed in either ASEL or ASER neuron in *unc-13(e312)* mutant background, and AIB calcium responses in these cell-specific rescuing animals were monitored. In the ASEL-rescuing animals, interestingly, weak increase of AIB activity was immediately decreased to the basal level at the upstep NaCl concentration change (Fig 31B , 32C). On the other hand, this fast recovery to basal level at upstep was not rescued by the ASER-specific UNC-13 expression (Fig 31C, 32C). Furthermore, the AIB calcium response in ASEL-specific rescuing animals was quite slight compared to that in ASER-rescuing animals during the downstep of NaCl concentration (Fig 31B,C, 32A). These results suggest that the ASEL signaling probably acts to inhibit the AIB activity.

Focused on the ASER function, I found that the ASER signaling seems to act as an excitatory signal for the AIB activity. AIB neurons were stimulated during the downstep of NaCl concentration, and this activation was also observed when UNC-13 was specifically expressed in the ASER neuron of *unc-13* mutants (Fig 31C, 32A). AIB neurons in these ASER-rescuing animals showed relatively a slow rise response after the downstep of NaCl concentration (compare to the wild-type response in Fig 29A

109

and and Fig 31C). The averaged calcium responses showed a significant activation during the 60 s 0 mM NaCl presentation (Fig 32A). However, the initial (10-sec) response after the downstep of NaCl is not significant (Fig 32B), suggesting that the property of fast activation was not rescued by the ASER-specific UNC-13 expression. On the other hand, strong inactivation at the upstep of NaCl concentration was not observed (Fig 32C), suggesting that there may be no inhibitory role for the AIB activation. To further confirm these results, I also monitored AIB activities using transgenic animals in which the tetanus toxin light chain from Clostridium tetani (TeTx) was cell-specifically expressed to block synaptic transmission. Expression of TeTx reduces presynaptic vesicle release by cleaving synaptobrevin/VAMP protein which is a core component for the synaptic vesicle fusion step [30]. The transgenic animals expressing TeTx specifically in the ASER showed a reduced AIB activity during the downstep of NaCl concentration (Fig 33). Therefore, I conclude that the ASER signaling probably excites AIBs when the downstep of NaCl concentration is applied.

3.4.4 The distinct glutaminergic signals from ASEL/R regulate AIB neuronal activity

Results of the above show that ASEL can inhibit AIB whereas ASER can stimulate AIB. Both ASE neurons are known to release glutamate as a transmitter [21]. To test whether the same glutamate signal has potentials both for an excitation and an inhibition for the AIB activity, I first monitored the AIB calcium responses in the *eat-*

4(ky5) mutant animal. *eat-4* encodes a vesicular glutamate transporter in *C. elegans*, and mutations in this gene cause lack or decrease of glutamate amount in synaptic vesicles. *eat-4(ky5)* mutants did not show clear AIB responses to both the downstep and upstep of NaCl concentration (Fig 34A). Therefore, these results suggest that the glutamate signal from ASEs may generate both excitation and inhibition in AIBs.

The AMPA-type ionotropic glutamate receptor GLR-1 is expressed in AIB interneurons, which can act as an excitatory postsynaptic receptor [6]. Using *glr-1(n2461)* mutant animals, I examined whether the AMPA-type glutamate receptor can really affect the AIB activity. I found that AIBs rose to their peak response within 10 s after the downstep of NaCl concentration. However, the response soon decayed after reaching the peak response (Fig 34B). On the other hand, wild-type animals showed a sustained activity during the 0 mM NaCl presentation (Fig 28B, Fig 29A). These results suggest that the AMPA-type glutamate receptor is required to last AIB neuronal activity during NaCl stimulation.

3.4.5 Coordinated synapse constructions between ASE-AIB generate the well-organized excitation/inhibition signal

These results suggest that the glutamate signal from ASER generates AIB excitation thorough an AMPA-type glutamate receptor. On the other hand, the glutamate signal from ASEL may generate AIB inhibition through an unidentified receptor. A reasonable mechanism to explain this unfamiliar phenomenon may be that the

site of synapses between ASEL-AIB and ASER-AIB is accurately organized on each neurite, according to the type of receptors. To test this hypothesis, I first observed the localization patterns of both the AMPA-type glutamate receptor GLR-1 and the glutamate-gated chloride channels GLC-3 on the postsynaptic AIB neurite. In the transgenic animals expressing GLR-1::GFP specifically in AIB, GLR-1::GFP fusion protein seemed to be localized uniformly on its neurite (Fig 35A). On the other hand, in the transgenic worms expressing GLC-3::Venus in AIB, GLC-3::Venus was localized as several size of puncta (Fig 35B).

The localization patterns of GLR-1::GFP and those of GLC-3::Venus seemed to be slightly different on the AIB neurite. However, due to many GFP puncta on the neurite, I could not make clear whether each receptor localizes at segregated regions on the neurite, and whether those localization really correspond to their specific functions for the excitatory (with ASER) or inhibitory (with ASEL) synapses. To confirm this, I next observed the relationship between the localization patterns of presynaptic vesicle-associated protein (RAB-3) on the ASER and the distribution of GLR-1::GFP or GLC-3::Venus on the AIB. I found that the positions of both mCherry::RAB-3 on the ASER and GLR-1::GFP on the AIB were quite closely distributed (Fig 36). On the other hand, those of mCherry::RAB-3 on the ASER and GLC-3::Venus on the AIB showed a distinct distribution (Fig 37). In addition, a spatial distance of mCherry::RAB-3 on the ASER and GLC-3::Venus on the AIB is more distant than that of mCherry::RAB-3 on the ASER and GLR-1::GFP on the AIB (Fig 36, 37). These results suggest that the AMPA-type glutamate receptor GLR-1 on the AIB, not GLC-3, receives the excitatory glutamate from the ASER.

3.5 Discussion

In this part of study, I identified that ASE-AIB circuit in the salt-chemotaxis behavior are regulated by two opposite synaptic encoding: The ASEL-AIB encode is an inhibitory input, whereas the ASER-AIB encode is an excitatory input. These two signaling employ the same neurotransmitter glutamate but utilize distinct postsynaptic glutamate receptors. The formation of each synapse between ASEL-AIB and ASER-AIB is accurately organized based on the type of glutamate receptors (Fig 38). These results suggest that well-organized localization patterns of receptors may be developed to build a dynamical encoding (system) in this neural circuit.

As for the postsynaptic AIB activity, signaling from several presynaptic neurons should contribute to generate its overall response. Cell-specific rescue experiments using UNC-13 protein showed that AIB neurons is slightly activated by the signal from ASEL at the moment of downstep of NaCl concentration (Fig 31B). However, ASEL signal may not contribute to continuous AIB activity during the downstep of NaCl [13]. Because *unc-13(e512)* mutant showed that AIBs are no responses, synaptic inputs from other sensory neurons do not affect to AIB responses, As one possibility, the hyperpolarized AIB activity might rebound to the steady state by the disappeared synaptic input from ASEL, when ASEL is inactivated by decrease of NaCl concentration.

glr-1(n2461) mutants also showed a strong reduction of AIB activity by the downstep of NaCl concentration but showed a weak response at the moment of the downstep stimulus (Fig 34B). Other glutamate receptors except for AMPA-type recep-

tors might have some role for this AIB initial activity, because *eat-4(ky5)* mutants which lack presynaptic glutamate transmitter, did not show any AIB responses during the changes of NaCl concentration. *C. elegans* has four classes of glutamate receptors, which are AMPA-type glutamate-gated cation channels, NMDA-type glutamate-gated cation channels, metabotropic G-protein-coupled glutamate receptors, and glutamate-gated chloride channels [31, 32, 33, 34]. In these receptors, the metabotropic glutamate receptor MGL-2 may be expressed in the AIB interneurons [34]. This metabotropic glutamate receptor may have some function for the AIB initial activation at the down-step of NaCl concentration.

I also have to focus on a recovery mechanism when the downstep stimulus is over (upstep of NaCl concentration). In the ASER-specific *unc-13* rescuing animals, the AIB activity decayed slowly after reaching to the peak response. Temporal pattern of this decay in AIBs was likely to be constant when the upstep of NaCl concentration was applied. On the other hand, ASEL-specific *unc-13* rescuing animals showed a quick decay of the AIB calcium dynamics at the upstep on NaCl concentration. The ASEL signal thus probably inhibits or inactivates the AIB activity at the upstep. In wild-type animals, this AIB inactivation may include two processes: elimination of an excitatory signal from ASER and addition of an inhibitory signal from ASEL.

This study for circuit dynamics in the salt-chemotaxis behavior of *C. elegans* is similar to the information processing in odor-chemotaxis- or thermotaxis-circuit in *C. elegans*. In odor-chemotaxis, the glutaminergic signal from AWC sensory neurons inhibits the activity of AIY interneurons through the activation of GLC-3 inhibitory glutamate receptors, whereas activates the activity of AIB interneurons through the

114

activation of GLR-1 excitatory glutamate receptors [6]. Furthermore, the EAT-4-dependent glutaminergic signal from AFD thermosensory neurons inhibits the activity of AIY interneurons through the activation of GLC-3 inhibitory glutamate receptors. By contrast, the EAT-4-dependent glutamate signal from AWC thermosensory neurons activate AIY interneurons (Fig 39) [35]. These results showed that sensory neurons for odor-/salt-chemotaxis and thermotaxis employ the same neurotransmitter glutamate but utilize distinct postsynaptic glutamate receptors. The mechanism how the same synaptic transmitter from the same class of presynaptic neurons does generate opposite postsynaptic neuronal-state is not well understood. Here, I found that the localization of synapses between ASEL-AIB and ASER-AIB is accurately coordinated according to the type of glutamate receptor. These distinct localization patterns on the AIB neurite contribute to the opposite regulation of activity.

My findings can provide the significant issue for circuit modeling in computational simulation. The computational neuroscientists often adapt to the assumption to decrease the degree of freedom in the combination of synaptic polarities (an excitatory or an inhibitory). The assumption is that all synapses made by a given presynaptic cell are of the same polarity (an excitatory or an inhibitory) [36]. But from this study, this assumption is not suitable for the circuit simulation in *C. elegans*.

The relationship between temporal dynamics in postsynaptic neuron and the number/localization of synapse connections should be considered to understand neuronal encoding for the circuit. How are postsynaptic neurons controlled by individual synaptic connections? It is a topic of future work to represent a general model for synaptic encoding dependent on the number/localization of synapses based on *in vivo* imaging.

I will analyze a dynamical synaptic encoding between ASE-AIB circuits by the integration system, which may be consisted of an optogenetical and a calcium imaging system.

Table 5: **Strain list.**

| Strain	Neuron	Genotype	Plasmid (conc.)	Marker (conc.)	Figure
DK5349	ASER	*taEx138*	[pDK594] *Pgcy-5::G-GECO1.2* (50 ng/uL)	*Plin-44::mCherry* (50 ng/uL)	Fig 28
DK5393	AIB	*taEx175*	[pDK157] *Pnpr-9::GGECO1.2* (80 ng/uL)	*Plin-44::mCherry* (50 ng/uL)	Fig 28, 29
DK5426	AIB	*taEx194; che-1(p679) I;*	[pDK644] *Pgcy-5::mCherry* (30 ng/uL) [pDK157] *Pnpr-9::GGECO1.2* (70 ng/uL)	*Punc25::mCherry* (50 ng/uL)	Fig 29
DK5400	AIB	*taEX175;* *unc-13(e312);*	-	-	Fig 31
DK5428	AIB	*taEX196; lin-15(n765ts) I;*	[pDK157] *Pnpr-9::GGECO1.2* (60 ng/uL) [pDK162] *Pgcy-5::TeTx::mCherry* (70 ng/uL)	pbLH98 (34.5 ng/uL)	Fig 33
DK5445	AIB	*taEx209; eat-4(ky5);*	[pDK157] *Pnpr-9::GGECO1.2* (70 ng/uL)	*Plin-44::mCherry* (50 ng/uL)	Fig 34
DK5433	AIB	*taEx201; glr-1(n2461)III;*	[pDK157] *Pnpr-9::GGECO1.2* (70 ng/uL)	*Plin-44::mCherry* (40 ng/uL)	Fig 34
DK5427	AIB	*taEx195; lin-15(n765ts) I;*	[pDK165] *Pnpr-9::glr-1::gfp* (50 ng/uL)	pbLH98 (30 ng/uL)	Fig 35
DK5431	AIB	*taEx199; lin-15(n765ts) I;*	[pDK708] *Pnpr-9::glc-3::Venus* (50 ng/uL)	pbLH98 (30 ng/uL)	Fig 35
DK5432	ASER	*taEx200; lin-15(n765ts) I;*	[pDK705] *Pgcy-5::mCherry::rab-3* (50 ng/uL)	pbLH98 (50ng/uL)	-
DK5443	ASER AIB	*taEx195; taEx200;* *lin-15(n765ts) I;*	-	-	Fig 36
DK5442	ASER AIB	*taEx199; taEx200;* *lin-15(n765ts) I;*	-	-	Fig 37
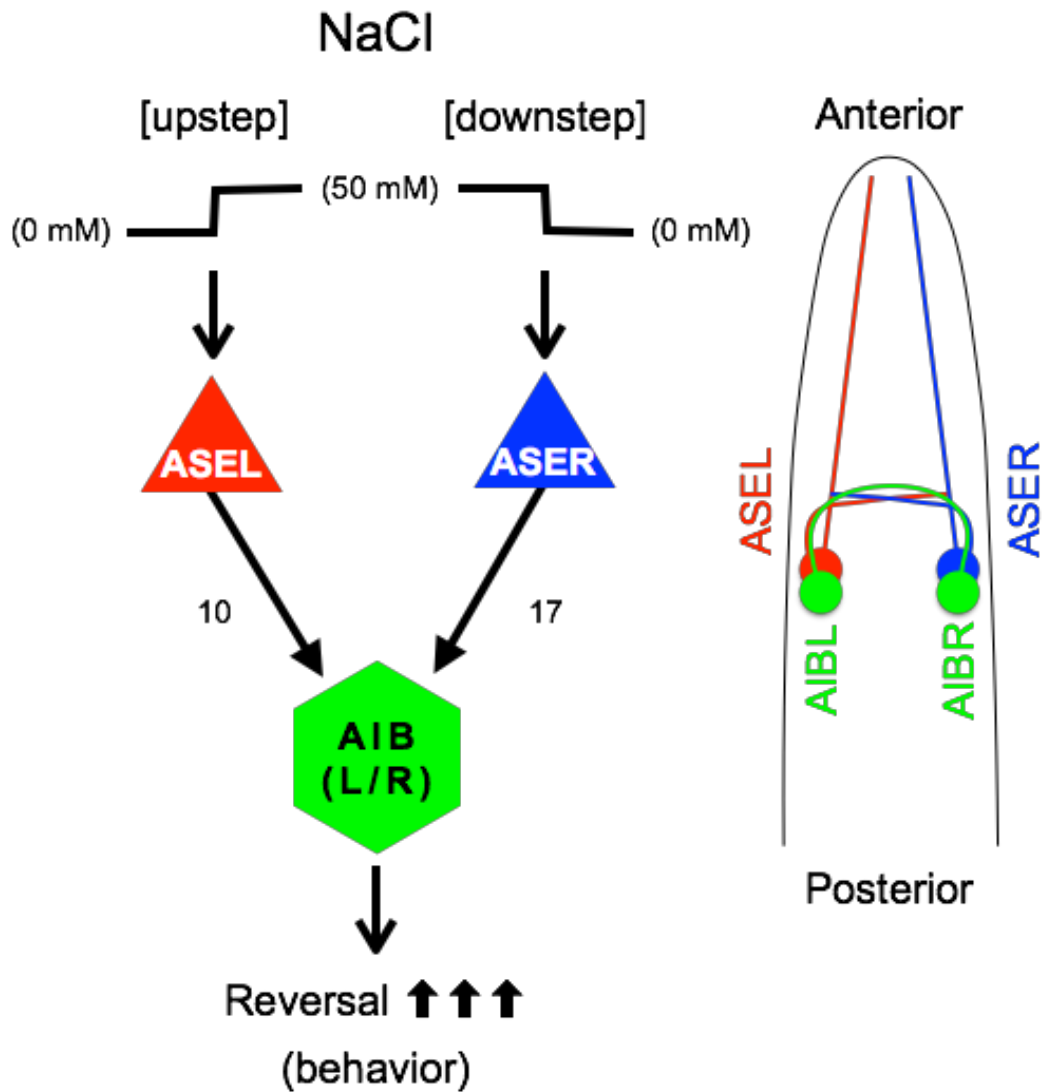
Figure 27: **Schematic drawing of simplified synaptic connections between ASEs to AIB.** The salt-sensing ASE neurons connect to their postsynaptic interneurons AIBL and AIBR. AIB neurons trigger reversal and turning behaviors. The numbers represent the number of synapse between two neurons.
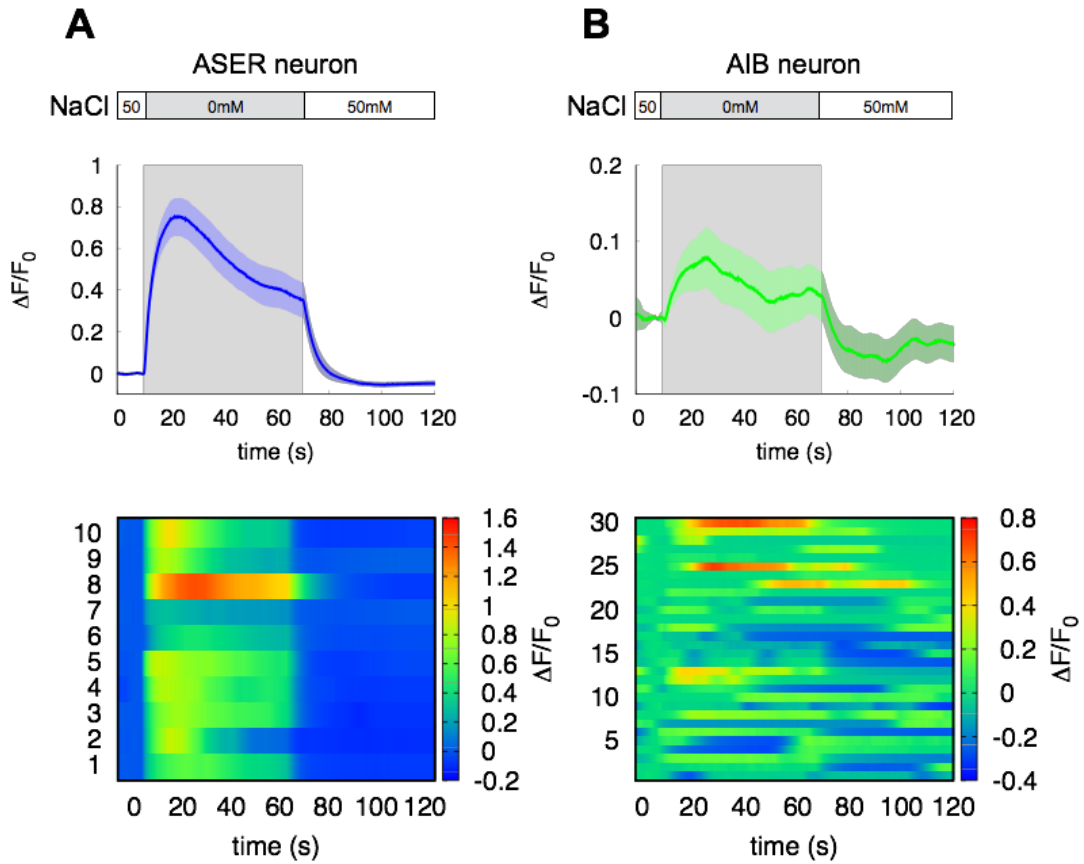
Figure 28: **Calcium dynamics of ASER and AIB neurons in response to NaCl concentration change.** Averaged calcium responses to NaCl concentration change (top) and heatmap traces of individual animals (bottom). (A) ASER responses in the wild-type animals (n=10). (B) AIB responses in the wild-type animals (n=30). ASER and AIB neurons were recorded individually. Shaded area is SEM.
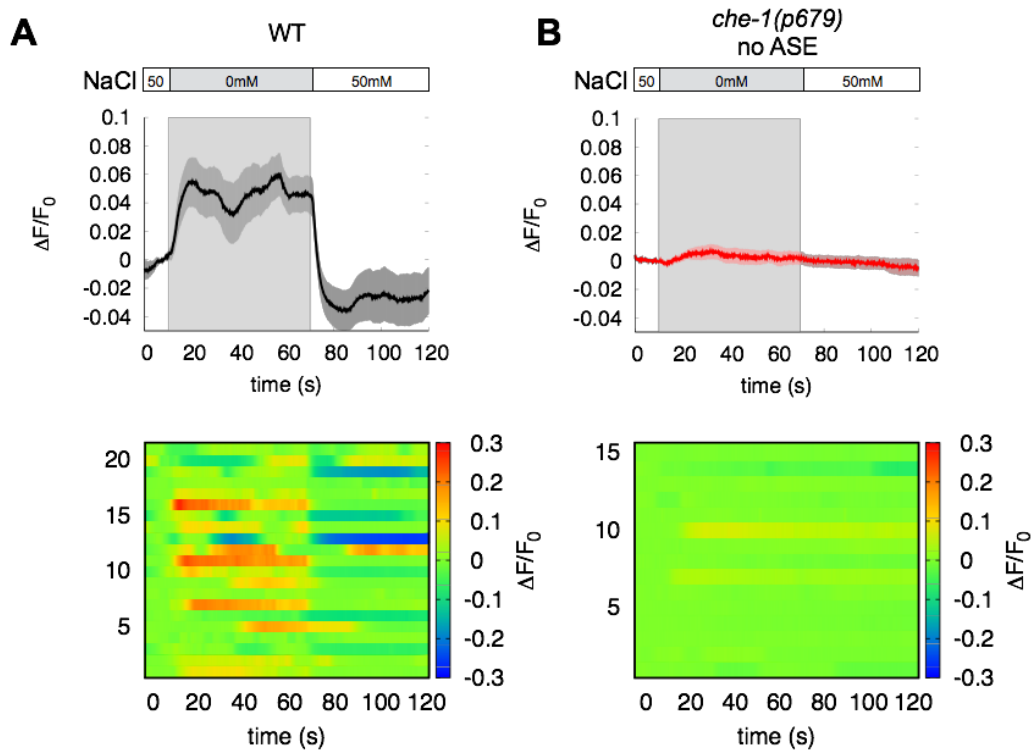
Figure 29: **Calcium dynamics of AIB in the wild type and *che-1(p679)* mutant animals.** Averaged calcium responses to NaCl concentration change (top) and heatmap traces of individual animals (bottom). (A) AIB responses in the wild-type animals (n=21). (B) AIB responses in the *che-1(p679)* mutant animals (n=15). Shaded area is SEM.
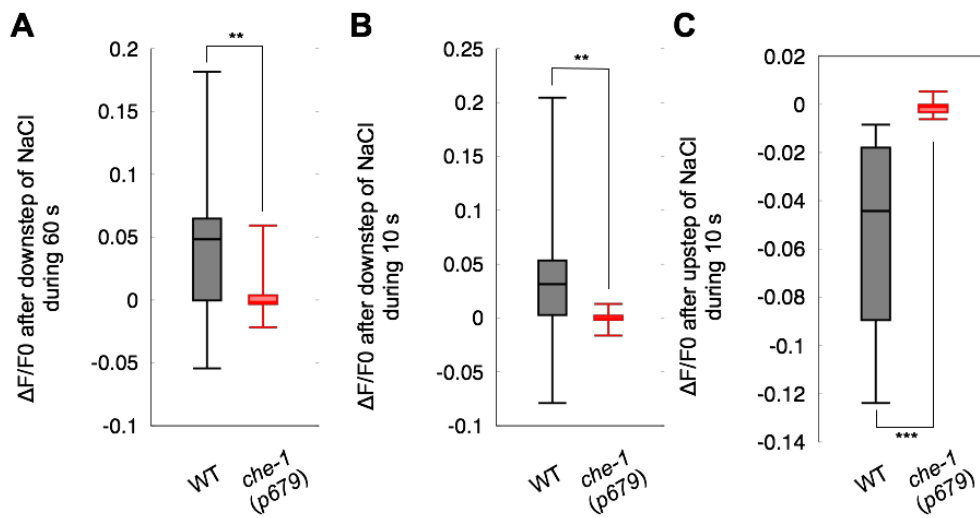
Figure 30: **Temporal responses of the AIB calcium dynamics in the wild-type and *che-1(p679)* mutant animals.** (A) Distribution of averaged calcium responses during 60 s of the downstep of NaCl concentration in the wild type (gray) and *che-1(p679)* mutant animals (red). (B, C) The difference between $(\Delta F/F_0)_{\text{after}}$ to $(\Delta F/F_0)_{\text{before}}$ were plotted from individual recordings in wild type (gray) and *che-1(p679)* mutants (red). $(\Delta F/F_0)_{\text{before}}$ means the averaged response during the 10 s before decrease (or increase) of NaCl concentration. Wilcoxon rank sum test were performed **; $p < 0.01$, ***; $p < 0.001$.
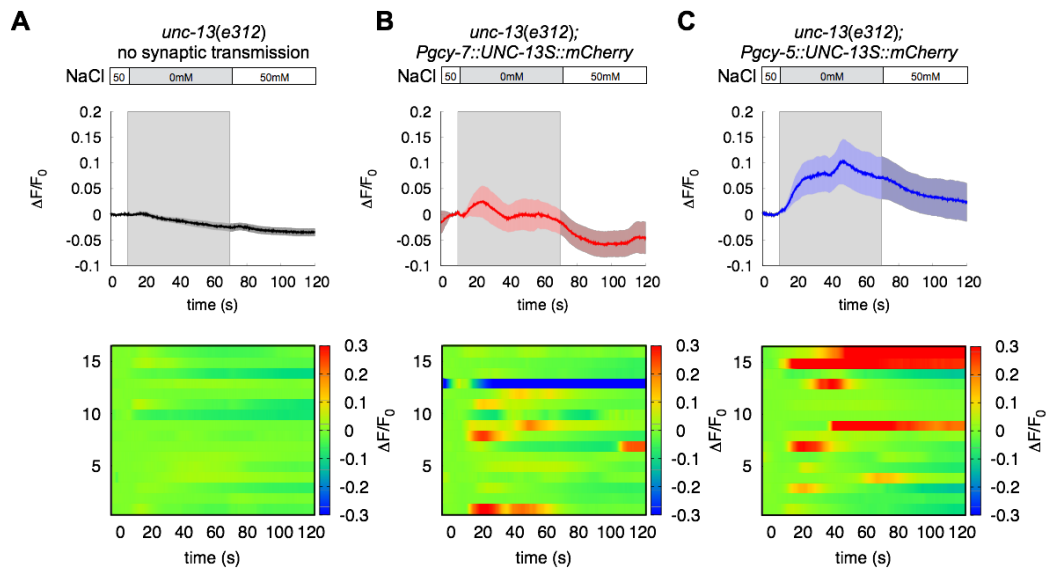
Figure 31: **AIB responses to the NaCl concentration change in the *unc-13(e312)* mutant animals and in cell-specific *unc-13* rescuing animals.** Averaged calcium responses to NaCl concentration change (top) and individual traces (bottom). (A) AIB responses in the *unc-13(e312)* mutants (n=16). (B) AIB responses in the ASEL-specific *unc-13* rescuing animals in the *unc-13(e312)* background (n=16). (C) AIB responses in the ASER-specific *unc-13* rescuing animals in the *unc-13(e312)* background (n=16). Shaded area is SEM.
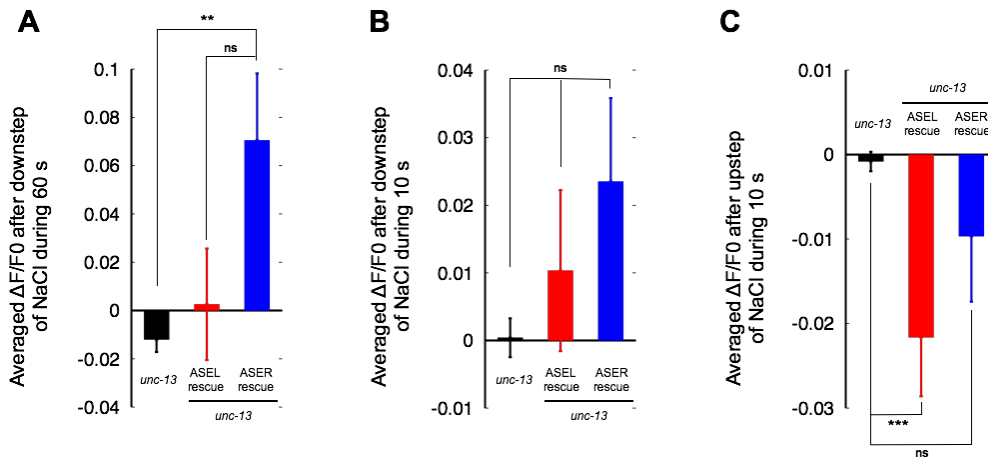
Figure 32: **Temporal responses of AIB to NaCl concentration change in the unc-13(e312), and in cell-specific unc-13 rescuing animals.** (A) Averaged $\Delta F/F_0$ after the downstep of NaCl concentration during 60 s in the *unc-13(e312)* (black), *unc-13(e312)* with a *ASELp::unc-13* rescuing transgene (red), and with a *ASERp::unc-13* rescuing transgene (blue). (B,C) The difference between $(\Delta F/F_0)_{\text{after}}$ to $(\Delta F/F_0)_{\text{before}}$ in the *unc-13(e312)* (black), and each rescuing animals (red, ASEL rescue), (blue, ASER rescue). $(\Delta F/F_0)_{\text{before}}$ is the averaged change during 10 s before decrease (or increase) of NaCl concentration. Steel-Dwass test was performed. **;$p < 0.01$, ***;$p < 0.001$; ns; not significant.
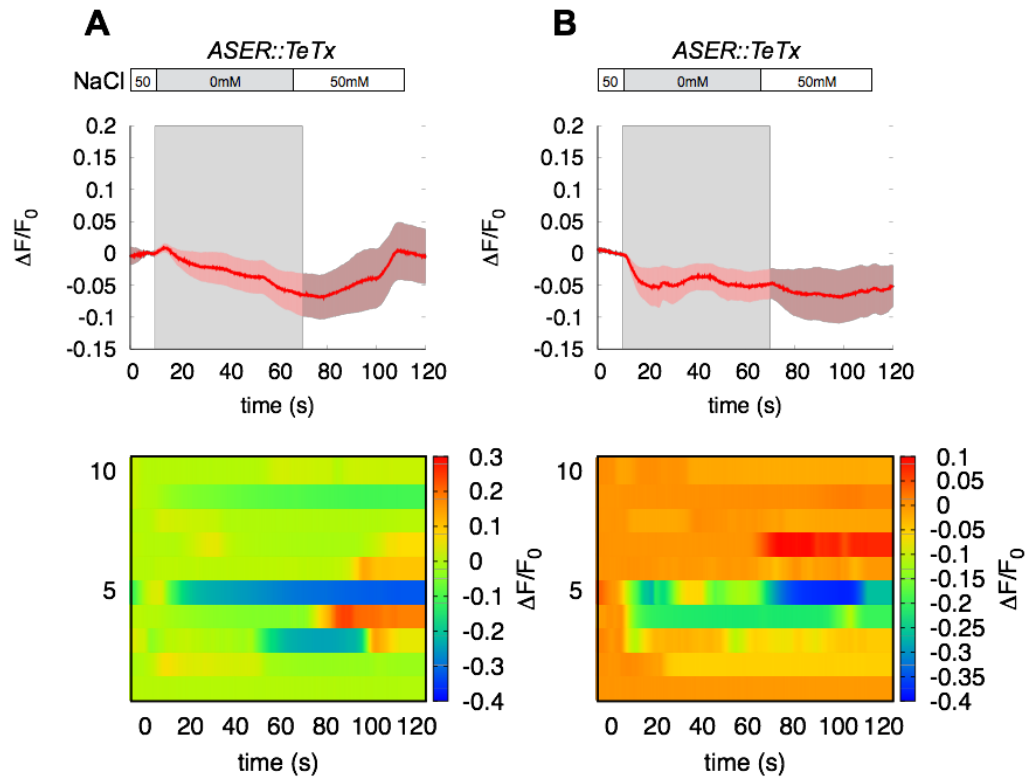
Figure 33: **AIB responses to the NaCl concentration change in the transgenic animals expressing TeTx in ASER.** Averaged calcium responses to changes of NaCl concentration (top) and individual traces (bottom) (n=10) in the first recording (A) and the second recording (B).
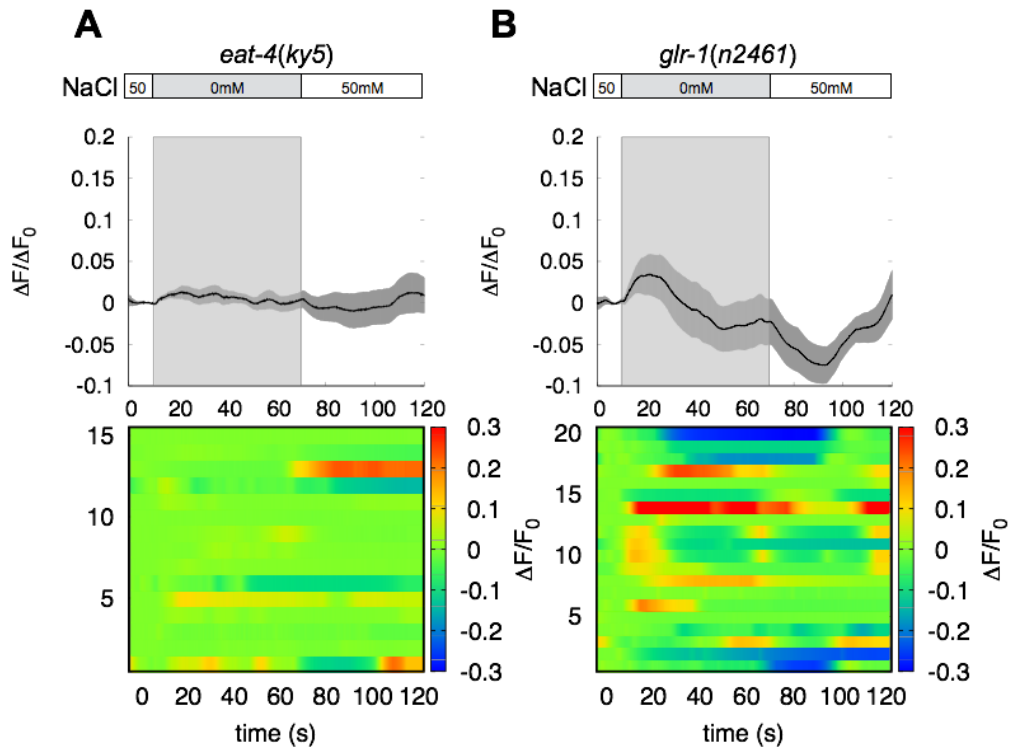
Figure 34: **AIB responses to NaCl concentration change in the *eat-4(ky5)* and the *glr-1(n2461)* mutants.** Averaged calcium responses to changes of NaCl concentration (top) and individual traces (bottom). (A) AIB responses in *eat-4(ky5)* mutants (n=15). (B) AIB responses in *glr-1(n2461)* mutants (n=20). Shaded area is SEM.
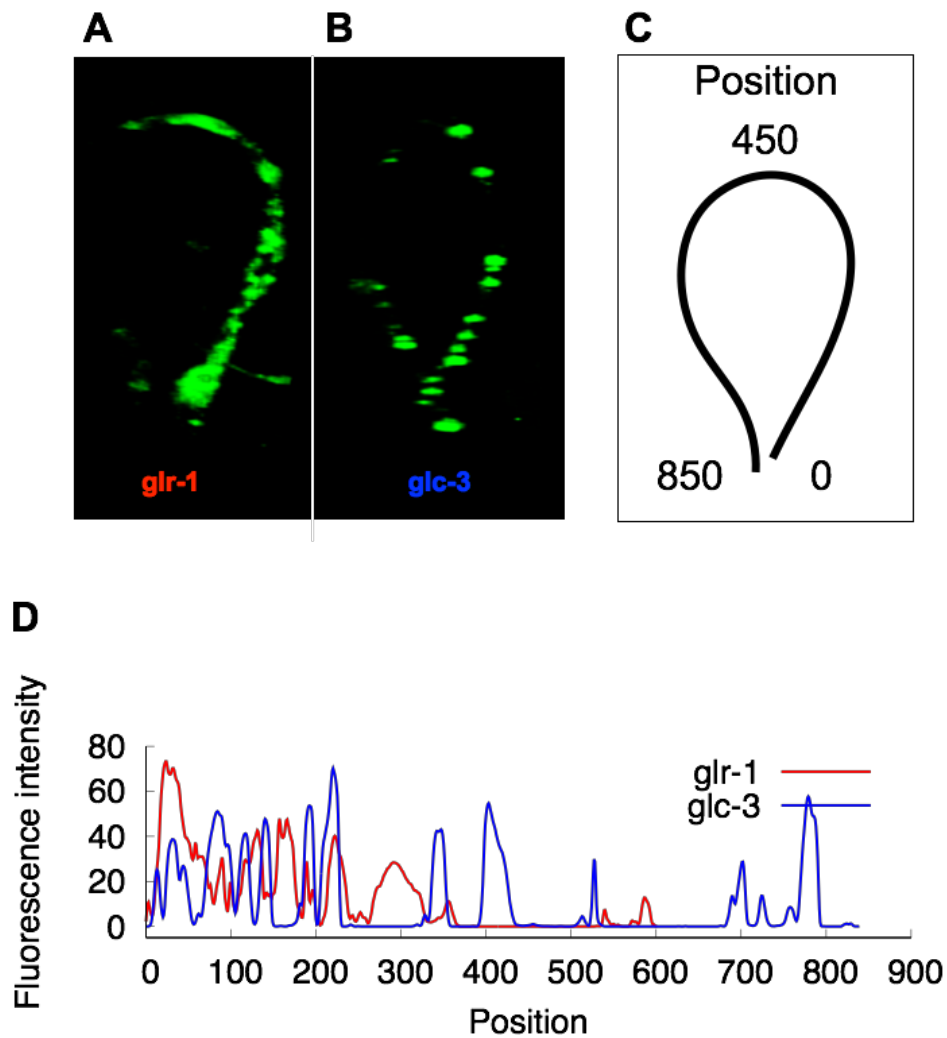
Figure 35: **The AMPA-type glutamate receptor and the glutamate-gated chloride channel are localized at distinct regions on the AIB neurite.** (A) Localization of the AMPA-type glutamate receptor. (B) Localization of the glutamate-gated chloride channel. (C) Schematic illustration for ' Position ' in the fluorescence profile (D). (D) The fluorescence profiles of the AMPA-type glutamate receptor (red) and the glutamate-gated chloride channel (blue) on AIB.

126

Figure 36: **The localization patterns of ASER presynaptic site and the AMPA-type glutamate receptors on AIB postsynaptic neurons.** (A) Schematic illustration of ASER (red) and AIB (green) neuronal morphology. The inset figure shows schematic illustration for 'Position' in the fluorescence profile in (E). (B) The confocal image of synaptic vesicle-associated protein (RAB-3) fused with mCherry in ASER (red). (C) The confocal image of the AMPA-type glutamate receptor fused with GFP in AIB (green). (D) Image obtained by merging (B) and (C). (E) The fluorescence profiles of the ASER synapses (*Pgcy-5::mCherry::rab-3*, red) and the AMPA-type glutamate receptor of the AIB (*Pnpr-9::glr-1::GFP*, green) on ASER synapses. (F) The scatter plot showing the correlation of the fluorescence intensity of *Pnpr-9::glr-1::GFP* with the fluorescence intensity of *Pgcy-5::mCherry::rab-3*. Values in the top right corner of scatter plots is correlation coefficient.
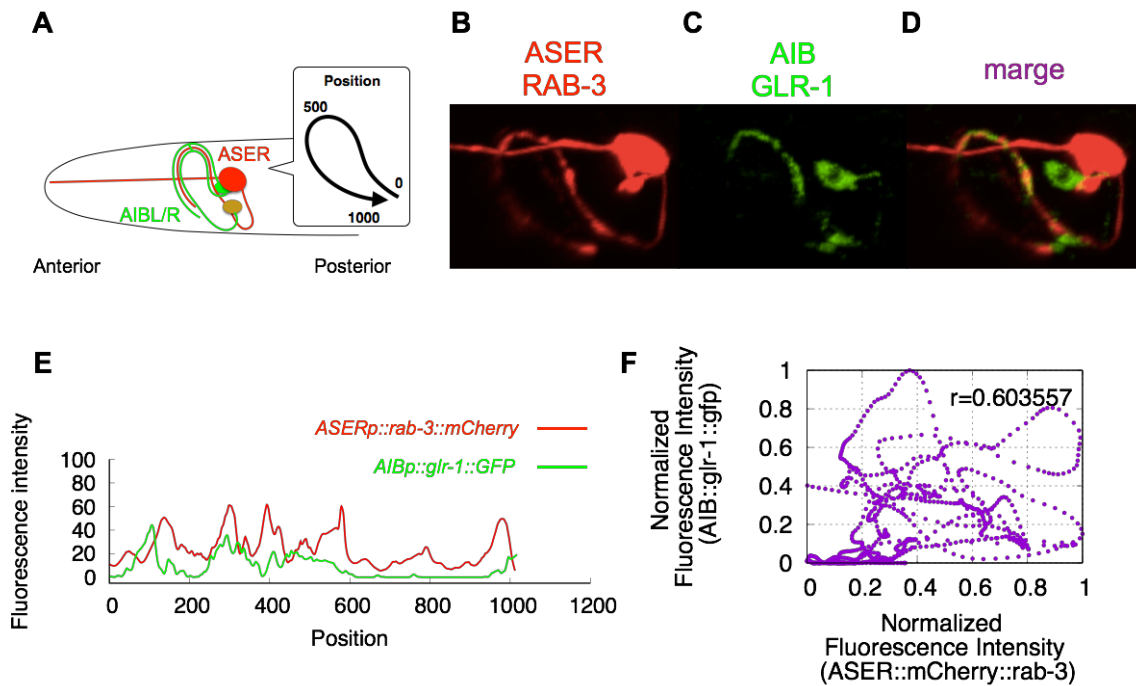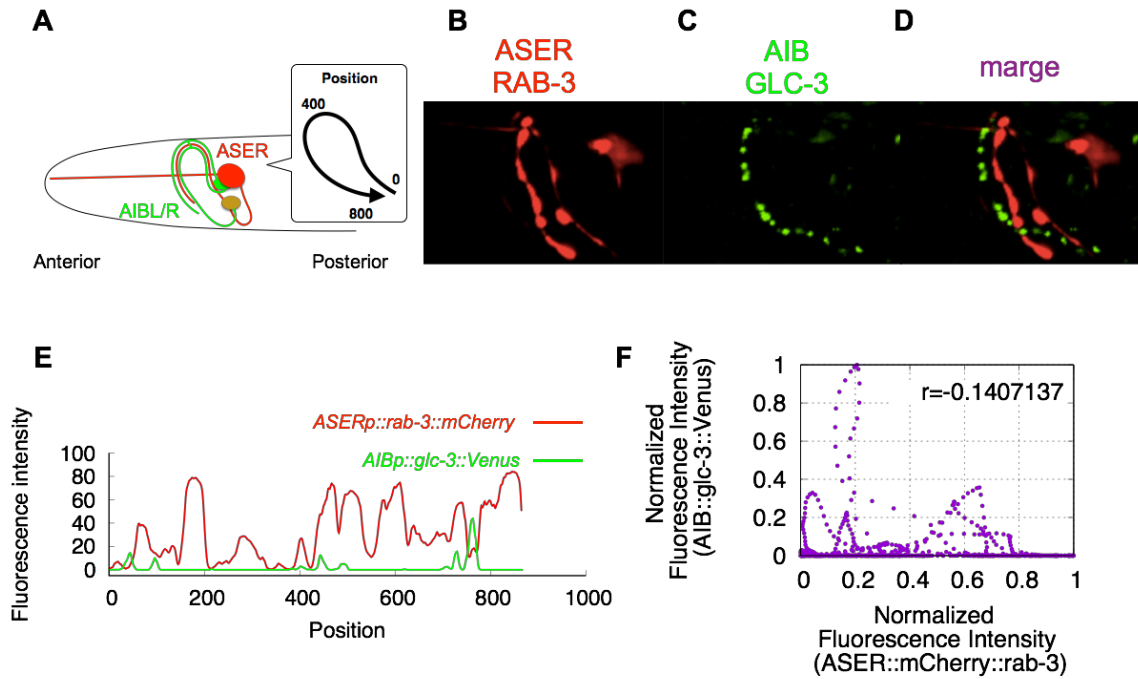
Figure 37: **The localization patterns of ASER presynaptic site and the glutamate-gated chloride channels on AIB postsynaptic neurons.** (A) Schematic illustration of ASER (red) and AIB (green) neuronal morphology. The inset figure shows schematic illustration for 'Position' in the fluorescence profile in (E). (B) The confocal image of synaptic vesicle-associated protein (RAB-3) fused with mCherry in ASER (red). (C) The confocal image of the glutamate-gated chloride channel fused with Venus in AIB (green). (D) Image obtained by merging (B) and (C). (E) The fluorescence profiles of the ASER synapses (*Pgcy-5::mCherry::rab-3*, red) and the glutamate-gated chloride channel of the AIB (*Pnpr-9::glc-3::Venus*, green) on ASER synapses. (F) The scatter plot showing the correlation of the fluorescence intensity of *Pnpr-9::glc-3::Venus* with the fluorescence intensity of *Pgcy-5::mCherry::rab-3*. Values in the top right corner of scatter plots is correlation coefficient.
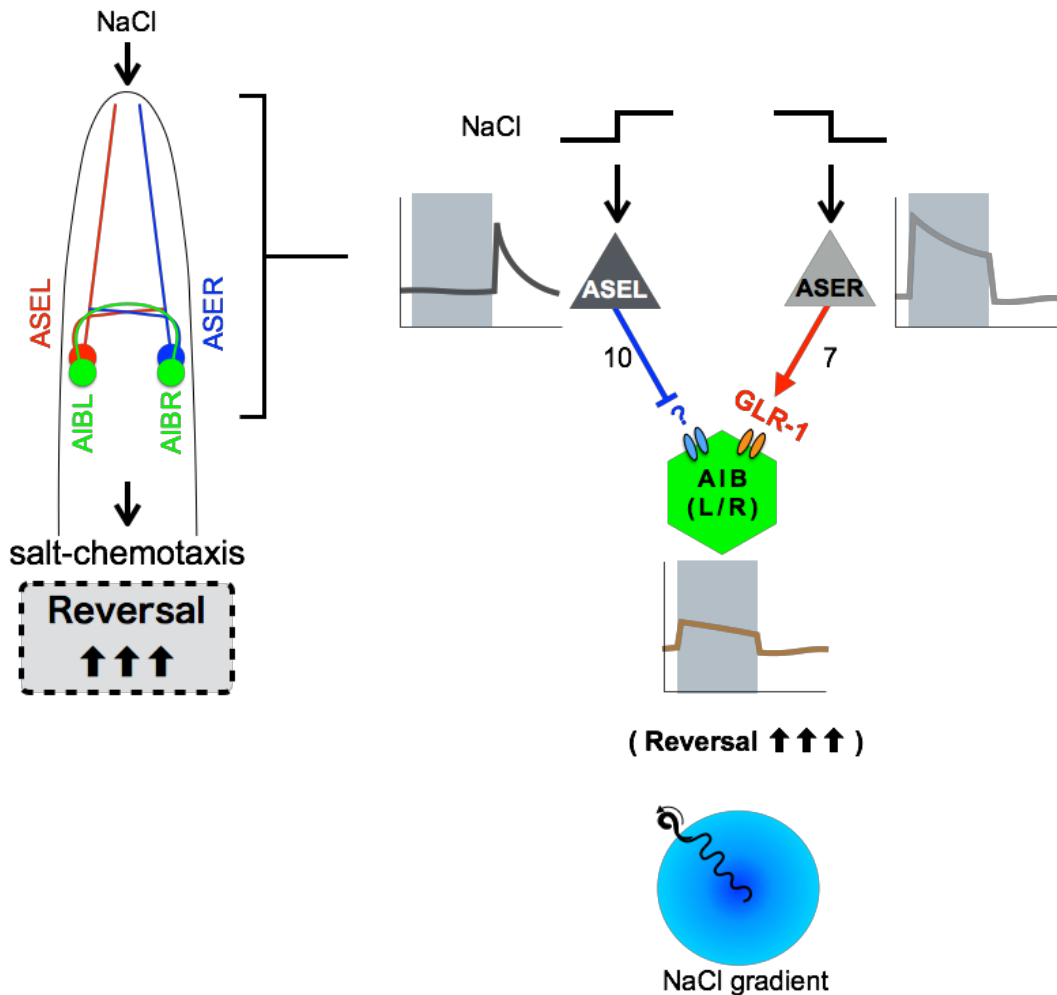
Figure 38: **Schematic model for the ASE-AIB circuit.** Glutaminergic signal from ASEL inhibits AIB activity through the unidentified inhibitory glutamate receptor, when NaCl concentration is increased. On the other hand, glutaminergic signal from ASER activates AIB activity through the AMPA-type ionotropic excitatory glutamate receptor, when NaCl concentration is decreased. AIB activation promotes increase of turn probability, whereas AIB inactivation promotes increase of forward run probability.
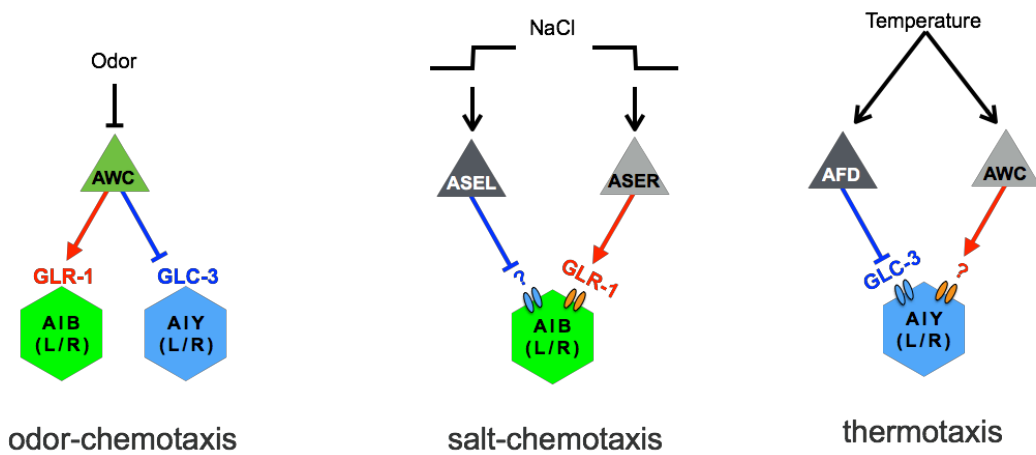
Figure 39: **Neural circuit for the odor-/salt-chemotaxis and thermotaxis in C. elegans.** The neural circuit for the odor-chemotaxis is consisted of AWC, AIB, and AIY neurons (left). The neural circuit for the salt-chemotaxis is consisted of ASE, AIB neurons (center). The neural circuit for the thermotaxis is consisted of AFD, AWC, and AIB neurons (right).

Bibliography

[1] White, J. G., Southgate, E., Thomson, J. N., and Brenner, S. (1986) The structure of the nervous system of the nematode *Caenorhabditis elegans. Philosophical Transactions of the Royal Society of London B: Biological Sciences,* **314**(1165), 1–340.

[2] Keene, A. C. and Waddell, S. (2007) *Drosophila* olfactory memory: Single genes to complex neural circuits. *Nature Reviews Neuroscience,* **8**(5), 341–354.

[3] Becker, C. G. and Becker, T. (2008) Adult zebrafish as a model for successful central nervous system regeneration. *Restorative neurology and neuroscience,* **26**(2-3), 71–80.

[4] Kato, S., Kaplan, H. S., Schrödel, T., Skora, S., Lindsay, T. H., Yemini, E., Lockery, S., and Zimmer, M. (2015) Global brain dynamics embed the motor command sequence of *Caenorhabditis elegans. Cell,* **163**(3), 656–669.

[5] Kamikouchi, A., Inagaki, H. K., Effertz, T., Hendrich, O., Fiala, A., Gopfert, M. C., and Ito, K. (2009) The neural basis of *Drosophila* gravity-sensing and hearing. *Nature,* **458**(7235), 165–171.

[6] Chalasani, S. H., Chronis, N., Tsunozaki, M., Gray, J. M., Ramot, D., Goodman, M. B., and Bargmann, C. I. (2007) Dissecting a circuit for olfactory behaviour in *Caenorhabditis elegans. Nature,* **450**(7166), 63–70.

[7] Sokolowski, M. B. (2001) *Drosophila*: Genetics meets behaviour. *Nature Reviews Genetics,* **2**(11), 879–890.

[8] Berkowitz, A., Roberts, A., and Soffe, S. (2010) Roles for multifunctional and specialized spinal interneurons during motor pattern generation in tadpoles, zebrafish larvae, and turtles. *Frontiers in Behavioral Neuroscience,* **4**, 36.

[9] Nguyen, J. P., Shipley, F. B., Linder, A. N., Plummer, G. S., Liu, M., Setru, S. U., Shaevitz, J. W., and Leifer, A. M. (2016) Whole-brain calcium imaging with cellular resolution in freely behaving *Caenorhabditis elegans. Proceedings of the National Academy of Sciences of the United States of America,* **113**(8), E1074–E1081.

[10] Bargmann, C. I. and Horvitz, H. R. (1991) Chemosensory neurons with overlapping functions direct chemotaxis to multiple chemicals in *C. elegans. Neuron,* **7**(5), 729–742.

[11] Goodman, M. B., Hall, D. H., Avery, L., and Lockery, S. R. (1998) Active currents regulate sensitivity and dynamic range in *C. elegans* neurons. *Neuron,* **20**(4), 763–772.

[12] Pierce-Shimomura, J. T., Morse, T. M., and Lockery, S. R. (1999) The fundamental role of pirouettes in *Caenorhabditis elegans* chemotaxis. *Journal of Neuroscience,* **19**(21), 9557–9569.

[13] Suzuki, H., Thiele, T. R., Faumont, S., Ezcurra, M., Lockery, S. R., and Schafer, W. R. (2008) Functional asymmetry in *Caenorhabditis elegans* taste neurons and its computational role in chemotaxis. *Nature,* **454**(7200), 114–117.

[14] Thiele, T. R., Faumont, S., and Lockery, S. R. (2009) The neural network for chemotaxis to tastants in *C. elegans* is specialized for temporal differentiation. *The Journal of Neuroscience,* **29**(38), 11904–11911.

[15] Iino, Y. and Yoshida, K. (2009) Parallel use of two behavioral mechanisms for chemotaxis in *Caenorhabditis elegans. Journal of Neuroscience,* **29**(17), 5370–5380.

[16] Oda, S., Tomioka, M., and Iino, Y. (2011) Neuronal plasticity regulated by the insulin-like signaling pathway underlies salt chemotaxis learning in *Caenorhabditis elegans. Journal of Neurophysiology,* **106**(1), 301–308.

[17] Kunitomo, H., Sato, H., Iwata, R., Satoh, Y., Ohno, H., Yamada, K., and Iino, Y. (2013) Concentration memory-dependent synaptic plasticity of a taste circuit regulates salt concentration chemotaxis in *Caenorhabditis elegans. Nature Communications,* **4**, 2210 EP –.

133

[18] Izquierdo, E. J. and Beer, R. D. (2013) Connecting a connectome to behavior: An ensemble of neuroanatomical models of *C. elegans* klinotaxis. *PLoS Computational Biology,* **9**(2), 1–20.

[19] Luo, L., Wen, Q., Ren, J., Hendricks, M., Gershow, M., Qin, Y., Greenwood, J., Soucy, E. R., Klein, M., Smith-Parker, H. K., Calvo, A. C., Colón-Ramos, D. A., Samuel, A. D. T., and Zhang, Y. (2014) Dynamic encoding of perception, memory, and movement in a *C. elegans* chemotaxis circuit. *Neuron,* **82**(5), 1115–1128.

[20] Satoh, Y., Sato, H., Kunitomo, H., Fei, X., Hashimoto, K., and Iino, Y. (2014) Regulation of experience-dependent bidirectional chemotaxis by a neural circuit switch in *Caenorhabditis elegans. Journal of Neuroscience,* **34**(47), 15631–15637.

[21] Serrano-Saiz, E., Poole, R. J., Felton, T., Zhang, F., De La Cruz, E. D., and Hobert, O. (2013) Modular control of glutamatergic neuronal identity in *C. elegans* by distinct homeodomain proteins. *Cell,* **155**(3), 659–673.

[22] Zhao, Y., Araki, S., Wu, J., Teramoto, T., Chang, Y. F., Nakano, M., Abdelfattah, A. S., Fujiwara, M., Ishihara, T., Nagai, T., and Campbell, R. E. (2011) An expanded palette of genetically encoded Ca^{2+} indicators. *Science,* **333**(6051), 1888–1891.

[23] Mello, C. C., Kramer, J. M., Stinchcomb, D., and Ambros, V. (1991) Efficient gene transfer in *C. elegans*: extrachromosomal maintenance and integration of transforming sequences.. *The EMBO Journal,* **10**(12), 3959–3970.

[24] Chronis, N., Zimmer, M., and Bargmann, C. I. (2007) Microfluidics for *in vivo* imaging of neuronal and behavioral activity in *Caenorhabditis elegans. Nature Methods,* **4**(9), 727–731.

[25] Gordus, A., Pokala, N., Levy, S., Flavell, S. W., and Bargmann, C. I. (2015) Feedback from network states generates variability in a probabilistic olfactory circuit. *Cell,* **161**(2), 215–227.

[26] Zaslaver, A., Liani, I., Shtangel, O., Ginzburg, S., Yee, L., and Sternberg, P. W. (2015) Hierarchical sparse coding in the sensory system of *Caenorhabditis elegans. Proceedings of the National Academy of Sciences of the United States of America,* **112**(4), 1185–1189.

[27] Uchida, O., Nakano, H., Koga, M., and Ohshima, Y. (2003) The *C. elegans che-1* gene encodes a zinc finger transcription factor required for specification of the ASE chemosensory neurons. *Development,* **130**(7), 1215–1224.

[28] Chang, S., Johnston, R. J., and Hobert, O. (2003) A transcriptional regulatory cascade that controls left/right asymmetry in chemosensory neurons of *C. elegans. Genes & Development,* **17**(17), 2123–2137.

[29] Richmond, J. E., Davis, W. S., and Jorgensen, E. M. (1999) UNC-13 is required for synaptic vesicle fusion in *C. elegans. Nature neuroscience,* **2**(11), 959–964.

[30] Schiavo, G. G., Benfenati, F., Poulain, B., Rossetto, O., de Laureto, P. P., DasGupta, B. R., and Montecucco, C. (1992) Tetanus and botulinum-B neurotoxins

block neurotransmitter release by proteolytic cleavage of synaptobrevin. *Nature,* **359**(6398), 832–835.

[31] Hart, A. C., Sims, S., and Kaplan, J. M. (1995) Synaptic code for sensory modalities revealed by *C. elegans* GLR-1 glutamate receptor. *Nature,* **378**(6552), 82–85.

[32] Maricq, A. V., Peckol, E., Driscoll, M., and Bargmann, C. I. (1995) Mechanosensory signalling in *C. elegans* mediated by the GLR-1 glutamate receptor. *Nature,* **378**(6552), 78–81.

[33] Cully, D. F., Vassilatis, D. K., Liu, K. K., Paress, P. S., Van der Ploeg, L. H. T., Schaeffer, J. M., and Arena, J. P. (1994) Cloning of an avermectin-sensitive glutamate-gated chloride channel from *Caenorhabditis elegans. Nature,* **371**(6499), 707–711.

[34] Dillon, J., Hopper, N., Holden-Dye, L., and O'Connor, V. (2006) Molecular characterization of the metabotropic glutamate receptor family in *Caenorhabditis elegans. Biochemical Society Transactions,* **34**(5), 942–948.

[35] Ohnishi, N., Kuhara, A., Nakamura, F., Okochi, Y., and Mori, I. (2011) Bidirectional regulation of thermotaxis by glutamate transmissions in *Caenorhabditis elegans. The EMBO Journal,* **30**(7), 1376–1388.

[36] Wicks, S. R., Roehrig, C. J., and Rankin, C. H. (1996) A dynamic network simulation of the nematode tap withdrawal circuit: predictions concerning synaptic function using behavioral criteria. *Journal of Neuroscience,* **16**(12), 4017–4031.

Chapter 4

General discussion and conclusion

The neural circuit is a complex system in which individual neurons interact with stochastic and chaotic dynamics through synaptic inputs. Using calcium imaging methods, circuit dynamics with cellular resolution has been analyzed for understanding the complex neural system navigating animal behaviors [1, 2, 3]. In addition to the calcium imaging, computational modeling using observation data is quite useful toward capturing the neural circuit as a dynamical system. In this thesis I attempted to generate a computational model for simulation of whole-brain dynamics in *C. elegans* based on calcium imaging.

As shown in chapter II, I succeeded to develop a novel computational model describing the spatio-temporal activity in single neuronal cell based on calcium imaging data. This neuron model has insufficient for analyses of circuit dynamics, because do not has a function for synaptic transmission. To expand this neuronal model for simulation of circuit dynamics, synaptic transmission through chemical synapses should be included to the model. In chapter III, I thus examined activities of the first-

layer interneurons AIB which are connected by the ASE presynaptic neurons, and tried to evaluate the role and meaning of each synaptic connection for their neuronal activities.

In chapter II, I developed the computational model for single neuronal dynamics based on the calcium imaging analyses. The proposed three-unit ODE neuronal model provides us much benefit for biological interpretation and as a simulation tool for circuit analysis (see chapter II) [4]. The most exciting result in the three-unit ODE model is that the model can reliably reproduces neuronal responses to several types of stimulation pattern, though the ODE model is constructed based on the calcium responses to a simple sensory stimulation. This finding implies that the computational model can be constructed relative easily based on neuronal responses to a simple pulse-like stimulation by using imaging methods including calcium imaging, if a focusing neuron has a near-linear feature in the temporal response. The previous studies reported that several neurons in *C. elegans* respond temporally as a near-linear to a pulse-like stimulus [5, 6, 7, 8]. So this three-unit ODE model might well be able to represent these neuronal responses. A performance of this ODE model will become more highly by using imaging data from wide-brain imaging [9, 10, 11], and thereby I will be able to provide a suitable model for whole-brain simulation with cellular resolution. Is this ODE model useful for modeling of the nervous system in other animals? Potentially, yes. Other model organisms, furthermore, several neurons also likely to have temporal feature of a near-linear response [12, 13, 14]. Thus, I believe that this ODE model is capable to model the cellular-level activity of the whole brains in several animals. However, several modifications will be required in this ODE model

138

for the circuit-level modeling.

Toward reconstruction of whole-brain in *C. elegans*, it should be modeled not only neuronal response but also synapse transmission. The proposed model represents the neuronal response to external stimuli, but cannot handle the interaction between neurons through synaptic inputs. To expand the single-cell computation into a circuit level, it is important to understand the synaptic regulation among neurons. In chapter III, I observed the dynamical responses of postsynaptic neurons in the salt-sensing circuit through synaptic encoding. The salt-sensing neurons ASEL and ASER have an opposite sensory function: ASEL is activated by the upstep of NaCl concentration, whereas ASER is activated by the downstep of NaCl concentration. In addition, ASEL promotes forward run probability, whereas ASER promotes turn probability [15, 16]. Both ASEL and ASER, however, release glutamate to the same postsynaptic neurons AIB [17, 18]. The molecular and cellular mechanisms about how the neural encoding does achieve such opposite behavioral output is poorly understood. From the *in vivo* neuronal recording in AIB neurons using several mutants, I found that ASEL and ASER regulate AIB activity by two opposite signals. The glutaminergic signal from ASEL inhibits AIB activity through the glutamate-gated chloride channel. The glutaminergic signal from ASER stimulates AIB activity through the AMPA-type ionotropic glutamate receptor. Surprisingly, the localization of each types of synapse between ASEL-to-AIB and ASER-to-AIB is accurately coordinated according to the type of glutamate receptors. Chalasani and his colleagues reported that a *C. elegans* sensory neuron oppositely regulates two different interneurons: The olfactory neuron AWC stimulates AIB interneurons, whereas inhibits AIY interneurons through

139

glutaminergic signal (Fig 39) [19]. On the other hand, this study showed that the single interneuron class can receive both excitatory and inhibitory signals depending on their synaptic sites, and that these signals can regulate fast response in the AIB neurons. These neuronal regulating mechanisms for postsynaptic neurons by sensory neurons can provide an insight into the more complex information processing in several processing through glutaminergic signals. Moreover, these results in this study take on a major significance for computational simulation of circuit dynamics. Computational neuroscientists often hypothesize that synapses from several presynaptic neurons have 'excitatory' or 'inhibitory' but not both, if presynaptic neurons employ a same neurotransmitter. The hypothesis is often applied for decrease in degree of freedom for simulation. However, these results imply that the hypothesis generate a restriction analysis from circuit simulation.

In this thesis, modeling of synapse transmission has not been achieved yet. These results have an insufficient for understanding of synaptic encoding dependent on between synapse numbers and localization in ASE-to-AIB neurons. Here I am planning to perform the *in vivo* imaging to get synaptic properties in the circuit for whole-brain modeling.

1. Modeling for chemical synapses

    I found out that ASEL inhibits AIB activity, whereas ASER activates AIB activity. Focus on this small circuit, the role and meaning of both an excitatory- and an inhibitory-signal through synapses can be obtained to construct a computational model of synaptic transmission. To analyze synaptic encoding pre-

cisely in this circuit, I will develop an integrated imaging system which consists of an optogenetic system for manipulation of presynaptic neuronal activity and a calcium imaging system for monitoring of postsynaptic neuronal activity. Based on imaging analyses using this integrated system, the proposed sigmoidally synaptic model [20] will be modified.

2. Modeling for electrical synapse

An electrical synapse conducts neuronal activity dependent on both number and surface area in two neighboring neurons. The *C. elegans* neural circuit has approximately 1,000 electrical synapses. An electrical synapse has a critical role for information processing in neural circuit. However a circuit model neglects the surface area in electrical synapses [21, 22, 23, 24]. A role of electrical synapse as information-relay junction for computational model is poorly understood. Is the neuronal activity via electrical synapses directly proportional to connection area? How does the power balance between chemical and electrical synapse have a relation to connecting neuronal activity? Rabinowitch and his colleagues developed the method for artificially modifying electrical connectivity in *C. elegans* [25]. I believe that a role of electrical synapse on synaptic encoding can be understood by the integration analysis using both Rabinowtch's synaptic-rewiring method and the imaging system. I am hopeful to develop a novel model for electrical synapse based on calcium imaging data.

Complex phenomena in brain, that are perception, memory formation, learning, and decision making, are encoded as activity patterns of individual neurons in neural

circuit. A whole-brain simulator (emulator) with cellular resolution can represent an activity patterns of individual neurons, thereby can generate these phenomena in neural circuit level. Of course, the simulator can also analyze the information processing in neural circuit. Using the simulator, nervous system of worms can be dissected a role as a component for information processing. This analysis will be a quite useful tool for understanding neural encoding. Moreover, the simulator can control their brain activity in virtual world. For example, simulated circuit-dynamics in worms can be easily represent for new memory, new learning and enhancement of ability for decision making. By merging a living worm's brain with an enforced brain in virtual world using optogenetic manipulations, I will get a wiser worm in real world. I believe that the whole-brain simulator enables us to use not only analysis for the neural information processing but also as a tool for memory, learning, and decision making by external brain. Near future I will have two brains: One is your self, and other is as an simulator on computer. This thesis represents the beginning of an endeavor as a first step to the my epic goal.

Bibliography

[1] Muto, A., Ohkura, M., Abe, G., Nakai, J., and Kawakami, K. (2013) Real-time visualization of neuronal activity during perception. *Current Biology,* **23**(4), 307–311.

[2] Keene, A. C. and Waddell, S. (2007) *Drosophila* olfactory memory: Single genes to complex neural circuits. *Nature Reviews Neuroscience,* **8**(5), 341–354.

[3] Barker, A. J. and Baier, H. (2015) Sensorimotor decision making in the zebrafish tectum. *Current Biology,* **25**(21), 2804–2814.

[4] Kuramochi, M. and Doi, M. (2017) A computational model based on multi-regional calcium imaging represents the spatio-temporal dynamics in a *Caenorhabditis elegans* sensory neuron. *PLOS ONE,* **12**(1), e0168415.

[5] Kato, S., Xu, Y., Cho, C. E., Abbott, L. F., and Bargmann, C. I. (2014) Temporal responses of *C. elegans* chemosensory neurons are preserved in behavioral dynamics. *Neuron,* **81**(3), 616–628.

[6] Kuhara, A., Ohnishi, N., Shimowada, T., and Mori, I. (2011) Neural coding in a single sensory neuron controlling opposite seeking behaviours in *Caenorhabditis elegans*. *Nature Communications,* **2**, 355 EP –.

[7] Oda, S., Tomioka, M., and Iino, Y. (2011) Neuronal plasticity regulated by the insulin-like signaling pathway underlies salt chemotaxis learning in *Caenorhabditis elegans*. *Journal of Neurophysiology,* **106**(1), 301–308.

[8] Luo, L., Wen, Q., Ren, J., Hendricks, M., Gershow, M., Qin, Y., Greenwood, J., Soucy, E. R., Klein, M., Smith-Parker, H. K., Calvo, A. C., Colón-Ramos, D. A., Samuel, A. D. T., and Zhang, Y. (2014) Dynamic encoding of perception, memory, and movement in a *C. elegans* chemotaxis circuit. *Neuron,* **82**(5), 1115–1128.

[9] Prevedel, R., Yoon, Y.-G., Hoffmann, M., Pak, N., Wetzstein, G., Kato, S., Schrodel, T., Raskar, R., Zimmer, M., Boyden, E. S., and Vaziri, A. (2014) Simultaneous whole-animal 3D imaging of neuronal activity using light-field microscopy. *Nature Methods,* **11**(7), 727–730.

[10] Nguyen, J. P., Shipley, F. B., Linder, A. N., Plummer, G. S., Liu, M., Setru, S. U., Shaevitz, J. W., and Leifer, A. M. (2016) Whole-brain calcium imaging with cellular resolution in freely behaving *Caenorhabditis elegans*. *Proceedings of the National Academy of Sciences of the United States of America,* **113**(8), E1074–E1081.

[11] Venkatachalam, V., Ji, N., Wang, X., Clark, C., Mitchell, J. K., Klein, M., Tabone, C. J., Florman, J., Ji, H., Greenwood, J., Chisholm, A. D., Srinivasan, J., Alkema, M., Zhen, M., and Samuel, A. D. T. (2016) Pan-neuronal imaging in roaming *Caenorhabditis elegans*. *Proceedings of the National Academy of Sciences of the United States of America,* **113**(8), E1082–E1088.

[12] Matsuo, E., Yamada, D., Ishikawa, Y., Asai, T., Ishimoto, H., and Kamikouchi, A. (2014) Identification of novel vibration- and deflection-sensitive neuronal subgroups in Johnston's organ of the fruit fly. *Frontiers in Physiology,* **5**, 179.

[13] Panier, T., Romano, S., Olive, R., Pietri, T., Sumbre, G., Candelier, R., and Debrégeas, G. (2013) Fast functional imaging of multiple brain regions in intact zebrafish larvae using selective plane illumination microscopy. *Frontiers in Neural Circuits,* **7**, 65.

[14] Dreosti, E., Esposti, F., Baden, T., and Lagnado, L. (2011) *In vivo* evidence that retinal bipolar cells generate spikes modulated by light. *Nature Neuroscience,* **14**(8), 951–952.

[15] Suzuki, H., Thiele, T. R., Faumont, S., Ezcurra, M., Lockery, S. R., and Schafer, W. R. (2008) Functional asymmetry in *Caenorhabditis elegans* taste neurons and its computational role in chemotaxis. *Nature,* **454**(7200), 114–117.

[16] Thiele, T. R., Faumont, S., and Lockery, S. R. (2009) The neural network for chemotaxis to tastants in *C. elegans* is specialized for temporal differentiation. *The Journal of Neuroscience,* **29**(38), 11904–11911.

[17] White, J. G., Southgate, E., Thomson, J. N., and Brenner, S. (1986) The structure of the nervous system of the nematode *Caenorhabditis elegans. Philosophical Transactions of the Royal Society of London B: Biological Sciences,* **314**(1165), 1–340.

[18] Serrano-Saiz, E., Poole, R. J., Felton, T., Zhang, F., De La Cruz, E. D., and Hobert, O. (2013) Modular control of glutamatergic neuronal identity in *C. elegans* by distinct homeodomain proteins. *Cell,* **155**(3), 659–673.

[19] Chalasani, S. H., Chronis, N., Tsunozaki, M., Gray, J. M., Ramot, D., Goodman, M. B., and Bargmann, C. I. (2007) Dissecting a circuit for olfactory behaviour in *Caenorhabditis elegans. Nature,* **450**(7166), 63–70.

[20] Izquierdo, E. J. and Lockery, S. R. (2010) Evolution and analysis of minimal neural circuits for klinotaxis in *Caenorhabditis elegans. Journal of Neuroscience,* **30**(39), 12908–12917.

[21] Wicks, S. R., Roehrig, C. J., and Rankin, C. H. (1996) A dynamic network simulation of the nematode tap withdrawal circuit: predictions concerning synaptic function using behavioral criteria. *Journal of Neuroscience,* **16**(12), 4017–4031.

[22] Rakowski, F., Srinivasan, J., Sternberg, P., and Karbowski, J. (2013) Synaptic polarity of the interneuron circuit controlling *C. elegans* locomotion. *Frontiers in Computational Neuroscience,* **7**, 128.

[23] Sakata, K. and Shingai, R. (2004) Neural network model to generate head swing in locomotion of *Caenorhabditis elegans*. *Network: Computation in Neural Systems,* **15**(3), 199–216.

[24] Kuramochi, M. and Iwasaki, Y. (2010) Quantitative modeling of neuronal dynamics in *C. elegans. Neural Information Processing. Theory and Algorithms: 17th International Conference, ICONIP 2010, Sydney, Australia, November 22-25, 2010, Proceedings, Part I,* pp. 17–24.

[25] Rabinowitch, I., Chatzigeorgiou, M., Zhao, B., Treinin, M., and Schafer, W. R. (2014) Rewiring neural circuits by the insertion of ectopic electrical synapses in transgenic *C. elegans. Nature Communications,* **5**, 4442 EP –.